NORTHWESTERN UNIVERSITY

Phase Coherent Electron Transport in Carbon Nanotube Devices

A DISSERTATION

SUBMITTED TO THE GRADUATE SCHOOL

IN PARTIAL FULFILLMENT OF THE REQUIREMENTS

for the degree

DOCTOR OF PHILOSOPHY

Field of Physics and Astronomy

By

Zhengfan Zhang

EVANSTON, ILLINOIS

June 2006

ABSTRACT

Phase Coherent Electron Transport in Carbon Nanotube Devices

Zhengfan Zhang

The electrical properties of multiwalled carbon nanotubes have been studied by transport measurements. The devices were fabricated by e-beam lithography after carefully locating the nanotubes on silicon/silicon oxide substrates. Low contact resistances have been achieved by plasma etch prior to metal deposition. Measurements were carried out at low temperature using a ^{3}He refrigerator or a dilution refrigerator to study the phase coherent electron transport in the nanotube devices.

The four-terminal differential resistance dV/dI has been measured as a function of various parameters such as dc bias current I_{dc}, gate voltage V_g, temperature T and magnetic field B. The devices we measured show large sample to sample variations. Even in the same sample, the characteristics change with thermal cycling and/or time. Asymmetric features with respect to dc bias current (voltage) have been found in these nanotube devices that can be well explained by Fano resonances, a natural consequence of interference effects between direct and resonant transmission. The sample specific behavior and metastability suggests defects or impurities play an important role in nanotube electron transport. Simultaneous

measurements of the contact resistances show correlation between the nanotube conductance and the metal-nanotube contact conductance. These results give us some insights into the influence of the defects or impurities on the conductance of the whole nanotube device. However, the exact locations of the defects or impurities cannot be determined due to non-local effects. The sample phase coherence length has been deduced from magnetic field dependent measurements.

To explain the behavior we observed in the multiwalled carbon nanotube devices, we proposed a model which explains the origin of the direct transmission and the transmission through a resonant state. This model also offers an explanation of the controversies arising from previous measurements of the multiwalled carbon nanotubes.

Acknowledgements

There are many people I would like to acknowledge their support and encouragement, without which, this thesis can never be completed.

My advisor, Prof. Venkat Chandrasekhar opened the door of mesoscopic physics for me and helped me overcome the challenges in the way of completion of this thesis. His broad knowledge of physics and experimental techniques is very helpful. He always challenges me for a better, deeper understanding of physics. I have learned to think independently and work under pressure. Zhigang Jiang, who has been my classmate ever since we were undergraduate freshmen, helped me through the entire period of the Ph.D. studies. I remember the countless days and nights we spent together fabricating samples, making measurements and diagnosing equipment problems. Even after he graduated, I still enjoyed discussing physics with him on the telephone. Dr. Dmitriy A. Dikin gave me so many valuable advice in experimental techniques and is always ready to help. I also enjoyed very inspiring discussion of physics with him. Dr. Sukkoo Jung helped me in the early stage of the e-beam lithography. Dr. Sergey Rozhok helped me with AFM operation. My senior student José Aumentado kindly answered my questions by email after he graduated. Jonghwa Eom taught me useful tricks for sample measurement. Our young student Paul Cadden-Zimansky took a heavy load of equipment maintenance work from me.

I also want to thank our other group members Dr. Dmitry Ruzmetov and Dr. Yongho Seo for their help in the laboratory.

I would thank Prof. Rodney S. Ruoff for his introduction to carbon nanotube physics and Prof. John B. Ketterson for the inspiring discussions.

Dr. Linhui Ye in Prof. Arthur J. Freeman's group helped me with the understanding of carbon nanotube electronic structures.

Finally, I would like to thank my parents for their support of everything, especially at the difficult hours of my life.

Contents

List of Tables

List of Figures

CHAPTER I

Introduction

As technology advances, there is a constant trend of scaling down for the microelectronics industry. This continuous scaling down depends on the improvement of lithography techniques. At present, the lithography technique is primarily by photolithography which is limited by the light wavelength. Extreme ultra violet (EUV) lithography is under development and is expected to be deployed for commercial usage by Intel in 2009 [**1**]. Other techniques such as X-ray lithography, electron beam lithography, ion-beam lithography, scanning probe lithography, imprint lithography are also available [**2**], but they have their own limitations and have not been adapted by the mainstream of the semiconductor industry. For example, electron beam lithography is widely used in research laboratories, however, it is not suitable for industry usage because the exposure speed is slow and the cost is high. Projection electron beam lithography is being developed to overcome this problem but it faces other technical challenges such as low throughput. Nanoimprint lithography is currently being developed and is promising for cheap, large scale and high throughput production with high resolution [**3**]. However, there are technical difficulties with regard to overlay and defects, i.e., due to the fact that direct contact is involved, the overlay error and the defect number and size is larger than optical-based lithography which projects the pattern from a distance. Besides current technical difficulties, this approach is very different from the current optical-based lithography techniques so that it creates an additional barrier for its acceptance by

the industry. Its future in microelectronics is still uncertain. All these approaches are known as "top-down" approaches as they start from bulk materials and fabricate nanostructures by a lithography process together with pattern transfer techniques such as wet etch, dry etch and/or thin film deposition, etc.. The advantage of the "top-down" approach is that this approach is easy for device integration, highly reliable and compatible with the current semiconductor fabrication process. The main disadvantage is the resolution is limited by the lithography process and the equipment is very expensive with each production line costing millions or billions of dollars. There is also the so called "bottom-up" approach. In the "bottom-up" approach, the nanostructure is fabricated using self assembly mostly by chemical methods. The advantage is the pattern can be very small and the process is highly parallel. There are different schemes for this "bottom up" approach. Molecular electronics, which uses single molecules as electronic devices, has been proposed as the ultimate technology. This has been foreseen by R. Feynman in 1959 [**4**], although the experimental realization was not achieved until recently [**5**]. In this approach, individual molecules in the circuit function as switches, storage devices, etc.. However, as individual molecules are very small, it is an extremely challenging task to connect them to macroscopic devices although significant progress has been made in this area [**6**, **7**]. This highlights the difficulties faced by the "bottom up" approach: device integration is very difficult. It is speculated that a combination of both approaches is very likely to be the solution: the "bottom up" approach synthesizes small structures while the "top down" approach integrates those structures and connects them to the macroscopic outside world (e.g. see Ref. [**8**]).

Carbon nanotubes (CNTs) are long molecules with a diameter of only one or a few nanometers, so they have at least one dimension that is too small to achieve by the traditional lithographic process, but they are easier to manipulate than individual molecules as they are long. CNT devices serve as a bridge from the traditional solid state devices to revolutionary molecular devices. The fact that CNTs can be either metallic or semiconducting depending on their chirality makes them very interesting and suitable as the basis for a variety of nanoelectronic devices. The most challenging problem of the CNT electronics is that the synthesis of CNTs is still not fully controllable and this lack of control brings severe problems for device integration [**9**].

Even though limited by the lack of control in the synthesis process, CNTs remain attractive to many researchers as they have been shown to have excellent electronic, mechanical, thermal and electrochemical properties [**9**]. As they can sustain a very high density of current [**10**], be ballistic conductors [**11**], have high mobility for semiconducting CNTs [**12**], have high mechanical strength [**13**], be chemically functional and conduct heat very efficiently [**14**], they have been regarded as one of the promising candidates for the building blocks of nanoelectronics despite the challenges discussed in the previous paragraph. CNT field effect transistors (FETs) [**15**–**18**], CNT p-n junction diodes [**19**], logic NOR gates [**20**], complementary metal-oxide semiconductor (CMOS) inverters (logic NOT gates) [**21**], and memory devices [**22**] have been fabricated. Very recently, a CNT ring oscillator consisting of five CMOS CNT inverters has been fabricated by scientists from IBM [**23**]. There are many other possible applications for CNTs as discussed in Ref. [**9**] in addition to nanoelectronics.

For example, CNTs can be used as material strengtheners, field emitters, thermal sinks and ion storage for batteries, etc..

Besides their great potentials for industrial applications, CNTs are also interesting from a scientific point of view. They are interesting to both solid state physicists and quantum chemists. From the point of view of solid state physics, the free electron wave extends to the whole crystal in perfect periodic potentials, which is known as Bloch's theorem [**24**]. Defects or impurities, phonons and surface boundaries, etc., cause scattering of the electrons, which is the origin of resistance. On the other hand, quantum chemistry starts from an electron wave localized around an atom, then constructs valence bonds or molecular orbitals when atoms get close to each other to form molecules. The electrons can then move around and conduct current. CNTs provide a common "play ground" for scientists from both disciplines. As will be discussed in Chapter 2, experiments on CNTs showed amazing agreement with theories with symmetry analysis. Therefore CNTs also provide a testing stage for various theories. For example, a single-walled carbon nanotube (SWCNT) is considered to be the ideal model for 1D electron transport where Luttinger liquid behavior has been speculated to exist [**25**].

This keen interest is reflected in the numbers of papers published each year as shown in Fig. 1.1. The numbers almost keep exponentially increasing for both general research on CNTs and research related to CNT electronic devices. Similarly, general research on nanoscience and nanotechnology is also rapidly increasing compared with other traditional physics areas such as mesoscopic physics and superconductivity. This boom of publications

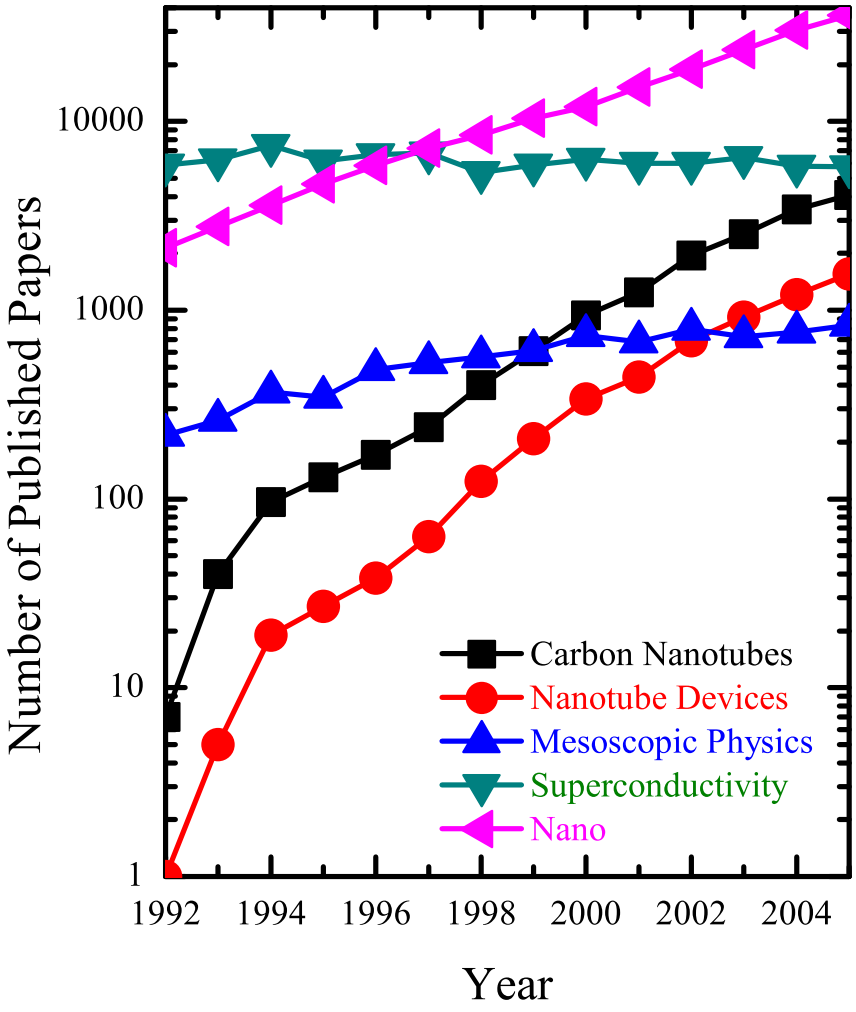

Figure 1.1. (Color) The numbers of published papers on the subject of carbon nanotubes and carbon nanotube devices from 1992-2005. For comparison, the numbers of papers on the subject of mesoscopic physics, superconductivity and nanoscience/nanotechnology are also shown. (Data obtained by keyword search from *Web of Science*.)

shows the exciting and breathtaking advances in this field. In this thesis, we will demonstrate our exploration of this field of transport measurements of CNT devices.

This thesis is organized as follows. In the next chapter we will give a short review of the electronic band structure of CNTs and an introduction to mesoscopic physics with quantum transport theory. A short literature survey of the experiments regarding electronic transport done by other researchers will be given in the same chapter. This is then followed by our sample fabrication procedures and transport measurement techniques in Chapter 3. In Chapter 4, the transport properties of multiwalled nanotubes (MWNTs) with normal metal contacts, sample specific behavior with regard to the contact resistances, and phase-coherent interference effects will be discussed. Finally, a summary and outlook for future work will be given at the end.

CHAPTER II

Overview of Carbon Nanotube Physics

Research on CNTs is multidisciplinary in nature. It is a collaborative study involving physicists, electrical engineers, chemists, materials scientists and mechanical engineers. Generally, CNTs can be in the form of an individual SWCNT, a SWCNT rope, a MWNT or a MWNT rope. A SWCNT can be described as a graphene sheet rolled into a cylindrical shape so that the structure is one dimensional. A MWNT is multiple layers of graphite rolled into concentric cylinders. A SWCNT rope is multiple SWCNTs packed parallel to each other forming a bundle and a MWNT rope consists of an array of parallel packed MWNTs. Figure 2.1 shows the difference between individual SWCNT, individual MWNT, SWCNT rope and MWNT rope.

A brief overview of physics involved in the present research will be give in this chapter. The CNT electronic band structure will be discussed first. It is remarkable that so many important results can be obtained elegantly by symmetry analysis. An overview of mesoscopic physics centering on quantum transport will then be given. Finally, a brief review of experiments on CNT electronic transport is provided. A number of numerical simulation results will also be presented for a more illustrative way to understand the underlying physics[1].

[1]All simulations in this thesis were performed by the author.

2.1. Electronic Structure of Carbon Nanotubes

2.1.1. Tight binding calculation of graphene band structure

As a SWCNT can be thought of as a graphene sheet rolled into a cylinder, the simplest theoretical approach is to start from the tight binding calculation of two-dimensional graphene. Then one incorporates the periodic boundary condition introduced in forming a cylinder. This technique is often referred to as the Brillouin Zone folding of energy dispersion relations [**26**]. For a unit cell of graphene as shown in Fig. 2.2(a), the hexagonal basis vectors are

$$\mathbf{a}_1 = (\frac{\sqrt{3}}{2}a, \frac{a}{2}), \tag{2.1a}$$

$$\mathbf{a}_2 = (\frac{\sqrt{3}}{2}a, -\frac{a}{2}), \tag{2.1b}$$

where a=2.46 Å is the lattice constant. The reciprocal lattice is then

$$\mathbf{b}_1 = (\frac{2\pi}{\sqrt{3}a}, \frac{2\pi}{a}), \tag{2.2a}$$

$$\mathbf{b}_2 = (\frac{2\pi}{\sqrt{3}a}, -\frac{2\pi}{a}). \tag{2.2b}$$

The reciprocal lattice is shown in Fig. 2.2(b). The high symmetry points are marked as Γ, M, and K.

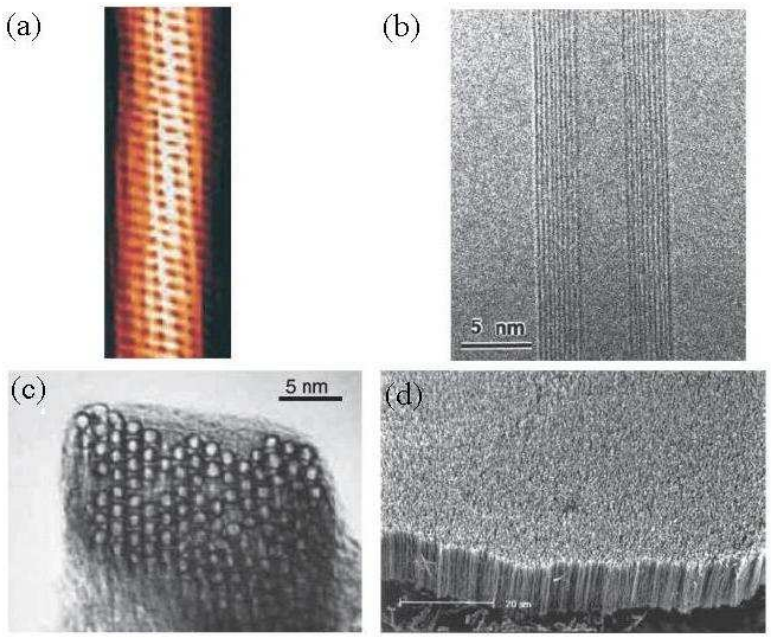

Figure 2.1. (Color) (a) STM image showing a SWCNT, (b) SEM image showing a MWNT, (c) TEM image showing a SWNT rope, (d) SEM image of an array of MWNTs. Adapted from Ref. [**9**].

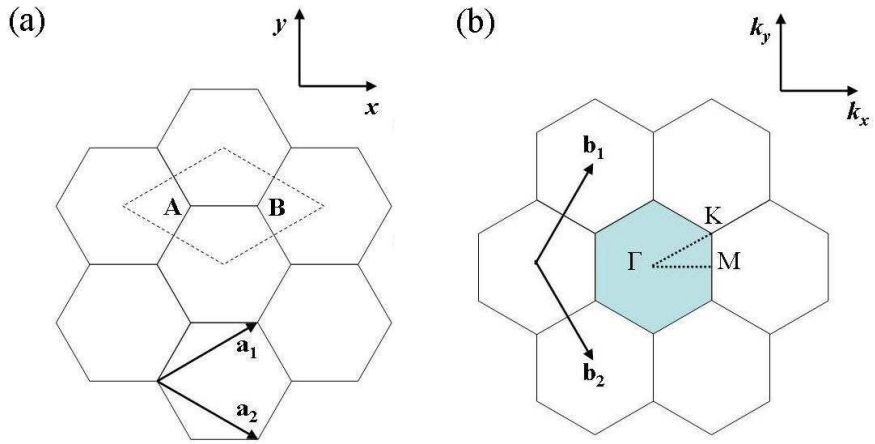

Figure 2.2. (Color) (a) The lattice structure of graphene. (b) **k** in reciprocal space. The unit cell of two dimensional graphene is shown as the dotted rhombus in (a). Brillouin zone of graphene is shown as the blue hexagon in (b). $\mathbf{a}_{1(2)}$, $\mathbf{b}_{1(2)}$ are unit cell lattice vectors and reciprocal lattice vectors, respectively. A and B are the two atoms in the unit cell. Γ, K are M are the high symmetry points in the hexagonal lattice.

The energy dispersion relation for a graphene sheet by a tight binding calculation is given by [**26**, **27**],

$$E_{g2D}(k_x, k_y) = \pm\gamma_0\sqrt{1 + 4\cos(\frac{ak_y}{2})\cos(\frac{\sqrt{3}ak_x}{2}) + 4\cos^2(\frac{ak_y}{2})}, \quad (2.3a)$$

$$= \pm\gamma_0\sqrt{3 + 2(\cos(\mathbf{k}\cdot\mathbf{a}_1) + \cos(\mathbf{k}\cdot\mathbf{a}_2) + \cos(\mathbf{k}\cdot(\mathbf{a}_1 - \mathbf{a}_2)))}. \quad (2.3b)$$

where $\gamma_0 = 3.033$ eV is the amplitude of the nearest-neighbor overlap integral.

Figure 2.3 shows the 3D representation of the graphene band structure. As the two bonding and anti-bonding bands only touch at six points denoted by K (or K') and the density of state (DOS) at the Fermi Level is zero [**26**], graphene is also called a zero-bandgap semiconductor.

2.1.2. Structure of single-walled carbon nanotubes

For the graphene sheet, we can define a vector $\mathbf{C}_h$ for a pair of integers (n, m) as

$$\mathbf{C}_h = n\mathbf{a}_1 + m\mathbf{a}_2 \quad (2.4)$$

as shown in Fig. 2.4, ($\mathbf{a}_1$, $\mathbf{a}_2$ are the two hexagonal basis vectors.) The translational vector $\mathbf{T}$ is the unit vector of a SWCNT along the tube axis (Fig. 2.4). In the unrolled sheet, it is perpendicular to the vector $\mathbf{C}_h$ (often called the Chiral vector). The unit cell of the SWCNT is the rectangle as shown in Fig. 2.4. The number of hexagons in each unit cell is denoted as N and the number of carbon atoms in a unit cell is $2N$. The parameters that define the SWCNTs are shown in Table 2.1.

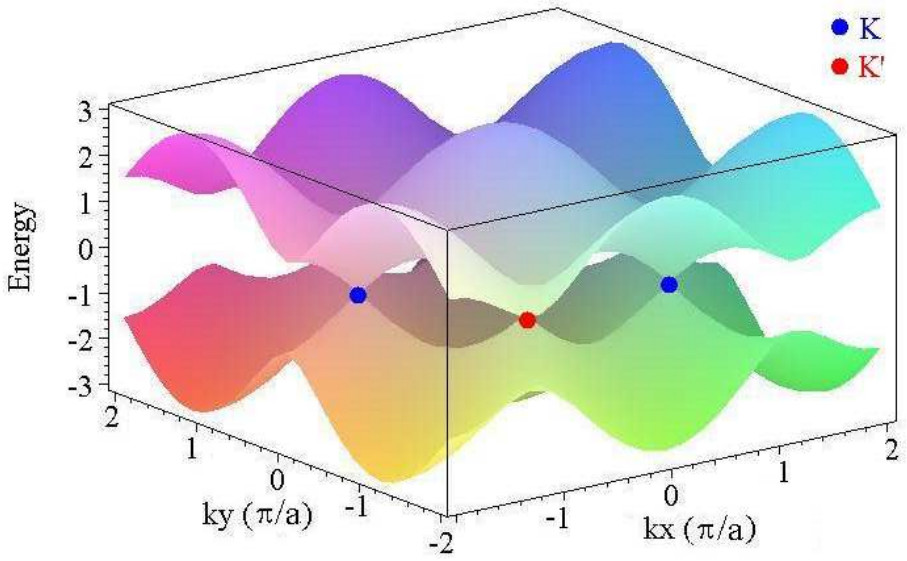

Figure 2.3. (Color) Three dimensional representation of the energy dispersion relation of the π and π^* bands of graphene band structure. Blue (red) dots correspond to the K (K') points in the first Brillouin zone.

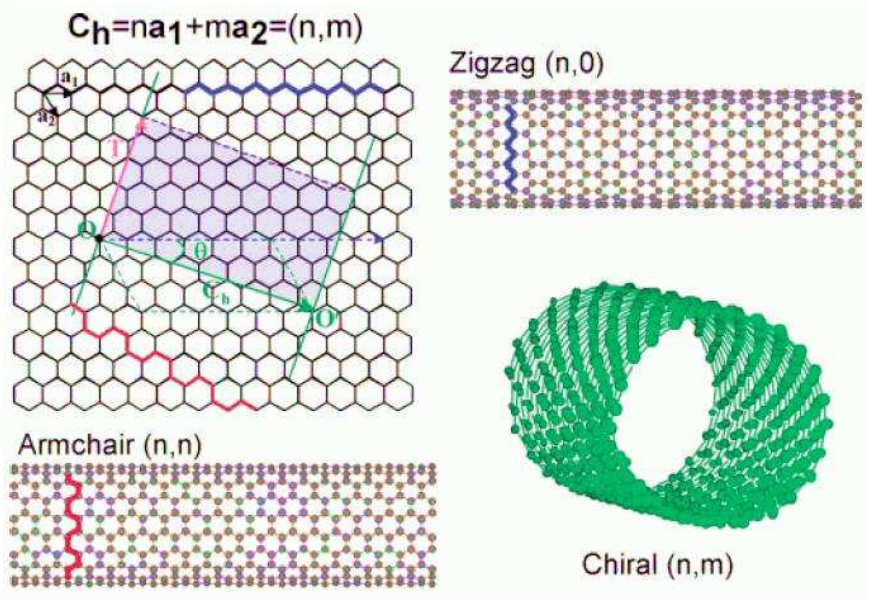

Figure 2.4. (Color) Schematics of three types of SWCNTs formed from rolling up of a graphene sheet. OO' is the rolling direction defines the chiral vector $\mathbf{C}_h = n\mathbf{a}_1 + m\mathbf{a}_2 \equiv (n, m)$. The translational vector $\mathbf{T}$ is along the tube axis, thus perpendicular to the chiral vector $\mathbf{C}_h$. The shaded area is the unit cell of SWCNT before it is rolled. θ is the chiral angle. Adapted from Ref. [**28**].

For some selected SWCNTs, we list the values of their parameters in Table 2.2. The set of integers (n,m), where $\mathbf{C}_h = n\mathbf{a}_1 + m\mathbf{a}_2$, is used to classify the CNTs. For $n = m$, i.e., (n,n), we have an armchair SWCNT. For $m = 0$, i.e. $(n,0)$, we have a zigzag SWCNT. The diameter d_t of the SWCNT is determined by the length of $\mathbf{C}_h$, $d_t = L/2\pi$, where $L = a\sqrt{n^2 + m^2 + nm}$ is the length of $\mathbf{C}_h$. All the other SWCNTs are called chiral SWCNTs. Figure 2.4 demonstrate the three types of SWCNTs (armchair, zigzag, chiral) that can be formed from a graphene sheet. Figure 2.5 shows the atomic configuration of (5,5), (9,0) and (10,0) SWCNTs with the atoms in the unit cell highlighted. Two other SWCNTs, (7,4) and (8,3), are shown in Fig. 2.6.

2.1.3. Metallic and semiconducting nanotubes

For a SWCNT with vector $\mathbf{C}_h$, the boundary condition $\psi(\mathbf{r}+\mathbf{C}_h) = \psi(\mathbf{r})$ must be satisfied. This leads to the quantization of the electron wave vector $\mathbf{k}$ along the circumference of the SWCNT.

$$\mathbf{k} \cdot \mathbf{C}_h = 2\pi q, \tag{2.5}$$

where q is an integer.

Equation 2.3a can be rewritten as

$$E_{g2D}(k_x, k_y) = \pm\gamma_0\sqrt{(1 + 2\cos(\frac{ak_y}{2})\cos(\frac{\sqrt{3}ak_x}{2}))^2 + 4\cos^2(\frac{ak_y}{2})\sin^2(\frac{\sqrt{3}ak_x}{2})}. \tag{2.6}$$

[2]Generated by *Virtual Nanolab* from Atomistix A/S, Denmark.

Table 2.1. Parameters of carbon nanotubes [**26**].

symbol	name	formula	value
a	length of unit vector	$a = \sqrt{3}a_{C-C} = 2.49$ Å, $a_{C-C} = 1.44$ Å	
$\mathbf{a}_1$, $\mathbf{a}_2$	unit vectors	$(\frac{\sqrt{3}}{2}, \frac{1}{2})a$, $(\frac{\sqrt{3}}{2}, -\frac{1}{2})a$	x,y coordinate
$\mathbf{b}_1$, $\mathbf{b}_2$	reciprocal lattice vectors	$(\frac{1}{\sqrt{3}}, 1)\frac{2\pi}{a}$, $(\frac{1}{\sqrt{3}}, -1)\frac{2\pi}{a}$	x,y coordinate
$\mathbf{C}_h$	chiral vector	$\mathbf{C}_h = n\mathbf{a}_1 + m\mathbf{a}_2 \equiv (n, m)$,	$(0 \le \lvert m\rvert \le n)$
L	length of $\mathbf{C}_h$	$L = \lvert\mathbf{C}_h\rvert = a\sqrt{n^2 + m^2 + nm}$	
d_t	diameter	$d_t = L/\pi$	
θ	chiral angle	$\sin\theta = \frac{\sqrt{3}m}{2\sqrt{n^2+m^2+nm}}$, $\cos\theta = \frac{2n+m}{2\sqrt{n^2+m^2+nm}}$,	$0 \le \lvert\theta\rvert \le \frac{\pi}{6}$
d	$\gcd(n, m)$[a]		
d_R	$\gcd(2n + m, 2m + n)$[a]		
$\mathbf{T}$	translational vector	$\mathbf{T} = t_1\mathbf{a}_1 + t_2\mathbf{a}_2 \equiv (t_1, t_2)$ $t_1 = \frac{2m+n}{d_R}$, $t_2 = -\frac{2n+m}{d_R}$	$\gcd(t_1, t_2) = 1$[a]
T	length of $\mathbf{T}$	$T = \lvert\mathbf{T}\rvert = \frac{\sqrt{3}L}{d_R}$	
N	Number of hexagons in the unit cell.	$N = \frac{2(n^2+m^2+nm)}{d_R}$	
$\mathbf{R}$	symmetry vector	$\mathbf{R} = p\mathbf{a}_1 + q\mathbf{a}_2 \equiv (p, q)$ $t_1 q - t_2 p = 1$, $(0 < mp - nq \le N)$	$\gcd(p, q) = 1$[a]
τ	pitch of $\mathbf{R}$	$\tau = \frac{(mp-nq)T}{N} = \frac{MT}{N}$	
ψ	rotation angle of $\mathbf{R}$	$\psi = \frac{2\pi}{N}$	
M	number of $\mathbf{T}$ in $N\mathbf{R}$.	$N\mathbf{R} = \mathbf{C}_h + M\mathbf{T}$	

[a] $\gcd(n, m)$ denotes the greatest common divisor of the two integers n and m.

Table 2.2. Values of parameters of selected SWCNTs.

$\mathbf{C}_h$	$(5,5)$	$(9,0)$	$(7,4)$	$(8,3)$	$(10,0)$	$(10,10)$	(n,n)	$(n,0)$
d	5	9	1	1	10	10	n	n
d_R	15	9	3	1	10	30	$3n$	n
d_t(Å)	6.78	7.05	7.55	7.72	7.83	13.56	$\frac{\sqrt{3}na}{\pi}$	$\frac{na}{\pi}$
θ	30°	0°	21.1°	15.3°	0°	30°	30°	0°
L/a	$\sqrt{75}$	9	$\sqrt{93}$	$\sqrt{97}$	10	$\sqrt{300}$	$\sqrt{3}n$	n
$\mathbf{T}$	$(1,-1)$	$(1,-2)$	$(5,-6)$	$(14,-19)$	$(1,-2)$	$(1,-1)$	$(1,-1)$	$(1,-2)$
T(Å)	2.46	4.26	13.7	42.0	4.26	2.46	2.46	4.26
T/a	1	$\sqrt{3}$	$\sqrt{31}$	$\sqrt{291}$	$\sqrt{3}$	1	1	$\sqrt{3}$
N	10	18	62	194	20	20	$2n$	$2n$
$\mathbf{R}$	$(1,0)$	$(1,-1)$	$(1,-1)$	$(3,-4)$	$(1,-1)$	$(1,0)$	$(1,0)$	$1,-1$
M	5	9	11	41	10	10	n	n
$E_g(eV)$	0	0.082	0.032	1.292	0.827	0	0	—

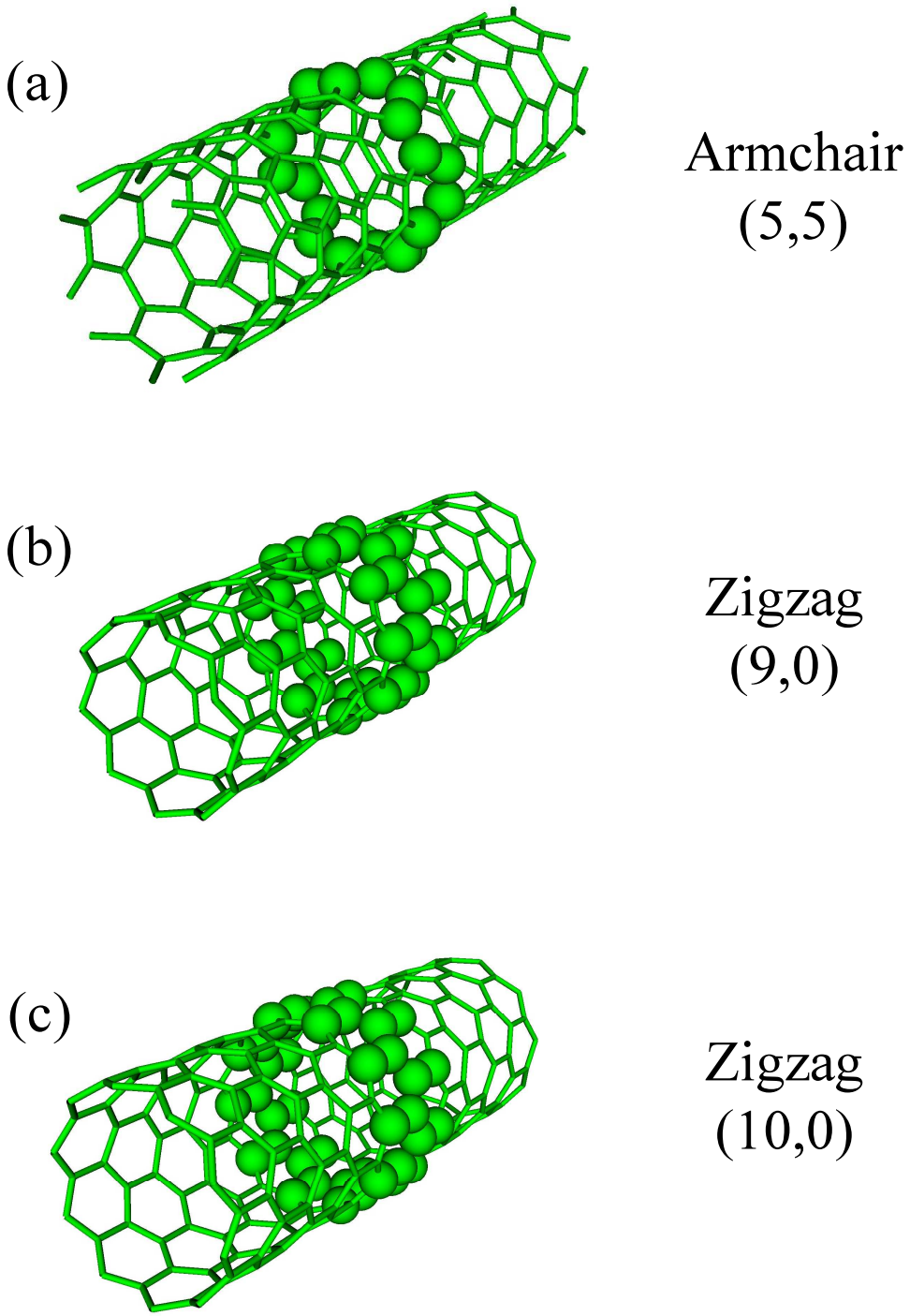

Figure 2.5. (Color) Atomic configuration[2] of (a) (5,5) armchair, (b) (9,0) zigzag and (c) (10,0) zigzag SWCNTs. The number of carbon atoms as in the unit cell shown is 20, 36, 40 in (5,5), (9,0), (10,0) SWCNTs respectively. (Note: the number of atoms is twice the number of hexagons in a unit cell.)

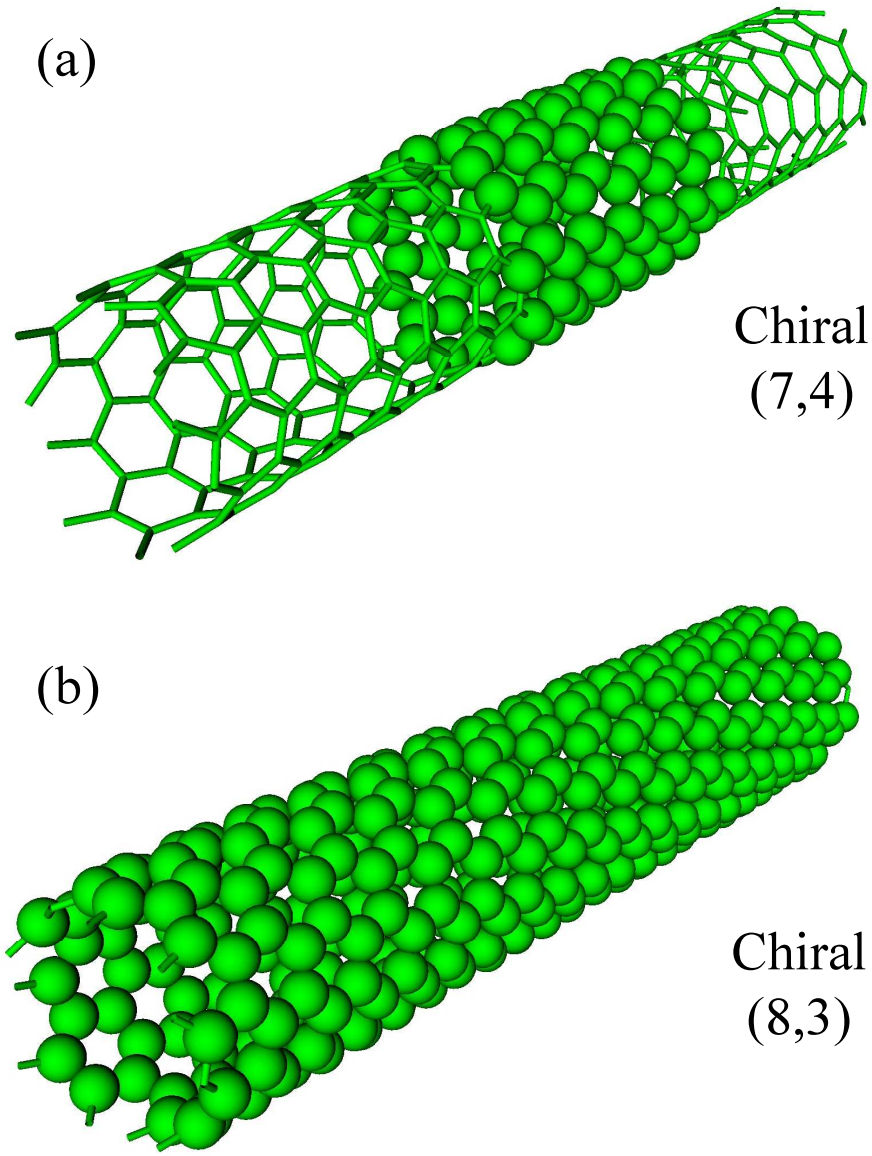

Figure 2.6. (Color) Atomic configuration[2] of (a) (7,4) chiral and (b) (8,3) chiral SWCNTs. The number of carbon atoms in the unit cell as shown is 124, 388 in (7,4), (8,3) SWCNTs respectively. (Note: the number of atoms is twice the number of hexagons in a unit cell.)

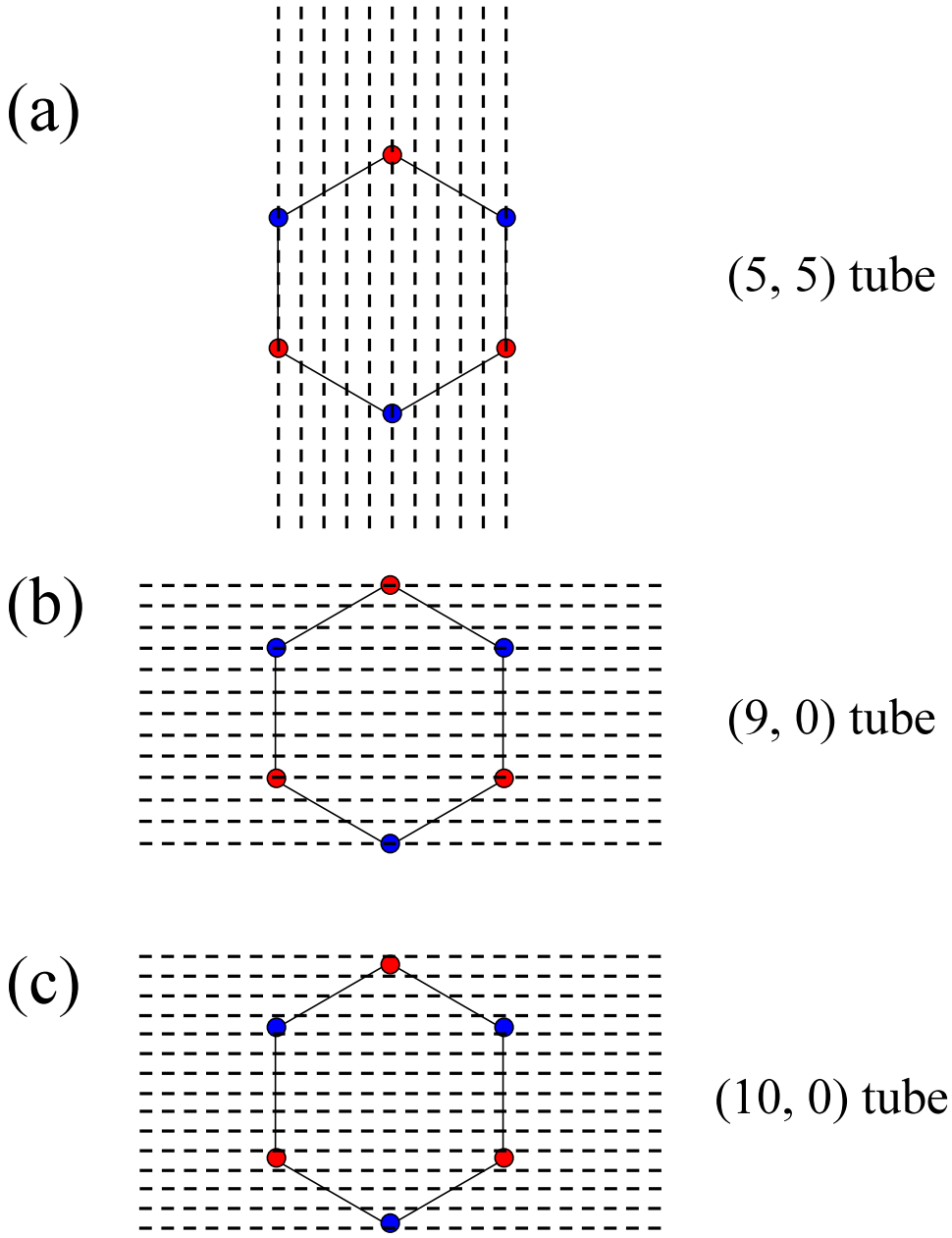

Figure 2.7. (Color) Diagrams for the first Brillouin zone of graphene with periodic boundary conditions. The dashed lines represent the allowed k-vector for (a) amchair (5,5), (b) zigzag (9,0), (c) zigzag (10,0) SWCNTs. The blue (red) dots represent the K (K') points.

For a gapless dispersion relation, one must have

$$\frac{\sqrt{3}ak_x}{2} = 2s\pi,\ s = 0, \pm1, \pm2, \ldots \tag{2.7a}$$

$$\frac{ak_y}{2} = (2t+1)\pi \pm \frac{1}{3}\pi,\ t = 0, \pm1, \pm2, \ldots \tag{2.7b}$$

or

$$\frac{\sqrt{3}ak_x}{2} = (2s+1)\pi,\ s = 0, \pm1, \pm2, \ldots \tag{2.7c}$$

$$\frac{ak_y}{2} = 2t\pi \pm \frac{1}{3}\pi,\ t = 0, \pm1, \pm2, \ldots \tag{2.7d}$$

must be satisfied. From Eqns. 2.1 and 2.4, we have

$$\mathbf{C}_h = \frac{\sqrt{3}}{2}a(n+m)\hat{\mathbf{e}}_x + \frac{a}{2}(n-m)\hat{\mathbf{e}}_y. \tag{2.8}$$

We put Eqn. 2.8 in the boundary condition Eqn. 2.5 and get

$$k_x\frac{\sqrt{3}}{2}a(n+m) + k_y\frac{a}{2}(n-m) = 2\pi q. \tag{2.9}$$

Equations 2.7a, 2.7b and 2.9 can be satisfied when $n - m = 3l$, where l is a nonzero integer. Equations 2.7c, 2.7d and 2.9 can be satisfied when $n = m$. These are the conditions for metallic SWCNTs. The same result was obtained in a geometric illustrative way in Ref. [**26**],

$$n - m = 3l, \tag{2.10}$$

where l is an integer.

We can see that any armchair CNT (n, n) will always be metallic while a zigzag or chiral CNT could be either metallic or semiconducting.

The dispersion relations for the armchair (n, n) and zigzag $(n, 0)$ CNTs are [**26**]

$$E_{armchair}(k) = \pm\gamma_0\sqrt{1 \pm 4\cos(\frac{q\pi}{n})\cos(\frac{ka}{2}) + 4\cos^2(\frac{ka}{2})}, \tag{2.11}$$

$$(-\pi < ka < \pi), (q = 1, \ldots, 2n)$$

and

$$E_{zigzag}(k) = \pm\gamma_0\sqrt{1 \pm 4\cos(\frac{\sqrt{3}ka}{2})\cos(\frac{q\pi}{n}) + 4\cos^2(\frac{q\pi}{n})}, \tag{2.12}$$

$$(-\frac{\pi}{\sqrt{3}} < ka < \frac{\pi}{\sqrt{3}}), (q = 1, \ldots, 2n).$$

A more illustrative way to show this relation is through Fig. 2.7, the reciprocal for (a) (5,5) armchair CNT, (b) (9,0) zigzag CNT, (c) (10,0) zigzag CNT. The $\mathbf{k}$ component $\mathbf{k}_{\parallel}$ that is parallel to the tube axis can be any value while the perpendicular component $\mathbf{k}_{\perp}$ is quantized. Thus the allowed $\mathbf{k}$ is parallel to the CNT tube axis as shown by the dashed lines in Fig. 2.7. We can see for an armchair CNT, $\mathbf{k}$ will always go through the K (K') points as shown in Fig. 2.7(a). For other CNTs such as (9,0) zigzag CNT in Fig. 2.7(b), $\mathbf{k}$ goes through the K (K') points while in Fig. 2.7(c), $\mathbf{k}$ does not go through the K (K') points for the (10,0) zigzag CNT.

Near the K points, the energy can be approximated as

$$E(\mathbf{k}) \approx \pm\frac{\sqrt{3}\gamma_0 a}{2}|\mathbf{k}-\mathbf{k}_K| = \hbar v_F|\mathbf{k}-\mathbf{k}_K|, \tag{2.13}$$

with the Fermi velocity $v_F = \frac{\sqrt{3}a\gamma_0}{2\hbar} = 8\times10^5\ m/s$. The DOS then can be calculated as [**29**]

$$\begin{aligned}\nu(E) &= \sum_{\text{all subbands}} \frac{1}{\pi}\left(\frac{dE}{dk}\right)^{-1}, \\ &= \frac{4a}{\pi^2 d_t\gamma_0}\sum_{q=-\infty}^{\infty} g(E,E_q), \end{aligned}\tag{2.14a}$$

with

$$g(E,E_q) = \begin{cases} \frac{|E|}{\sqrt{E^2-E_q^2}} & |E| > |E_q| \\ 0 & |E| < |E_q|, \end{cases} \tag{2.14b}$$

$$E_q = |3q-n+m|\frac{a\gamma_0}{\sqrt{3}d_t}. \tag{2.14c}$$

Equation 2.14c can be rewritten as

$$E_q = |q+\beta|\frac{2\hbar v_F}{d_t}, \tag{2.14d}$$

where $\beta = 0$ for a metallic CNT and ±1 for a semiconducting CNT.

For metallic SWCNTs, the DOS per unit length along the tube axis is a constant regardless of the diameter and chirality [**30**],

$$\nu(E_F) = \frac{8}{\sqrt{3}\pi a\gamma_0} = \frac{4}{\pi\hbar v_F}. \tag{2.15}$$

For semiconducting SWCNTs, the band gap is inversely proportional to the tube diameter as [**26**, **27**][3]

$$E_g = \frac{2\gamma_0 a_{C-C}}{d_t}. \tag{2.16}$$

Figure 2.8 shows the dispersion relation and the DOS for several selected SWCNTs. For armchair SWCNTs (5,5) and (10,10), the DOS at the Fermi level is finite, so they are always metallic. For zigzag SWCNTs (9,0) and (10,0), as Eqn. 2.10 indicates, the (9,0) CNT is matallic and the (10,0) CNT is semiconducting.

2.1.4. Curvature effect

The calculation by Brillouin Zone folding of the graphene dispersion relation only considered the periodic boundary condition $\psi(\mathbf{r}+\mathbf{C}) = \psi(\mathbf{r})$, but ignored the effect of curvature of the CNT tube axis. If the tube diameter is large enough, the curvature effect can be ignored. However, for small diameter SWCNTs, such curvature effects cannot be ignored. We illustrate this by a symmetry argument. As shown in Fig. 2.9, from the symmetry argument, the distortion of the reciprocal lattice due to the curvature effects can only be along certain axes of symmetry. Therefore $\mathbf{k}$ will still go through the K points for an armchair SWCNT, while

[3]The equation in Ref. [**26**] missed a factor of 2.

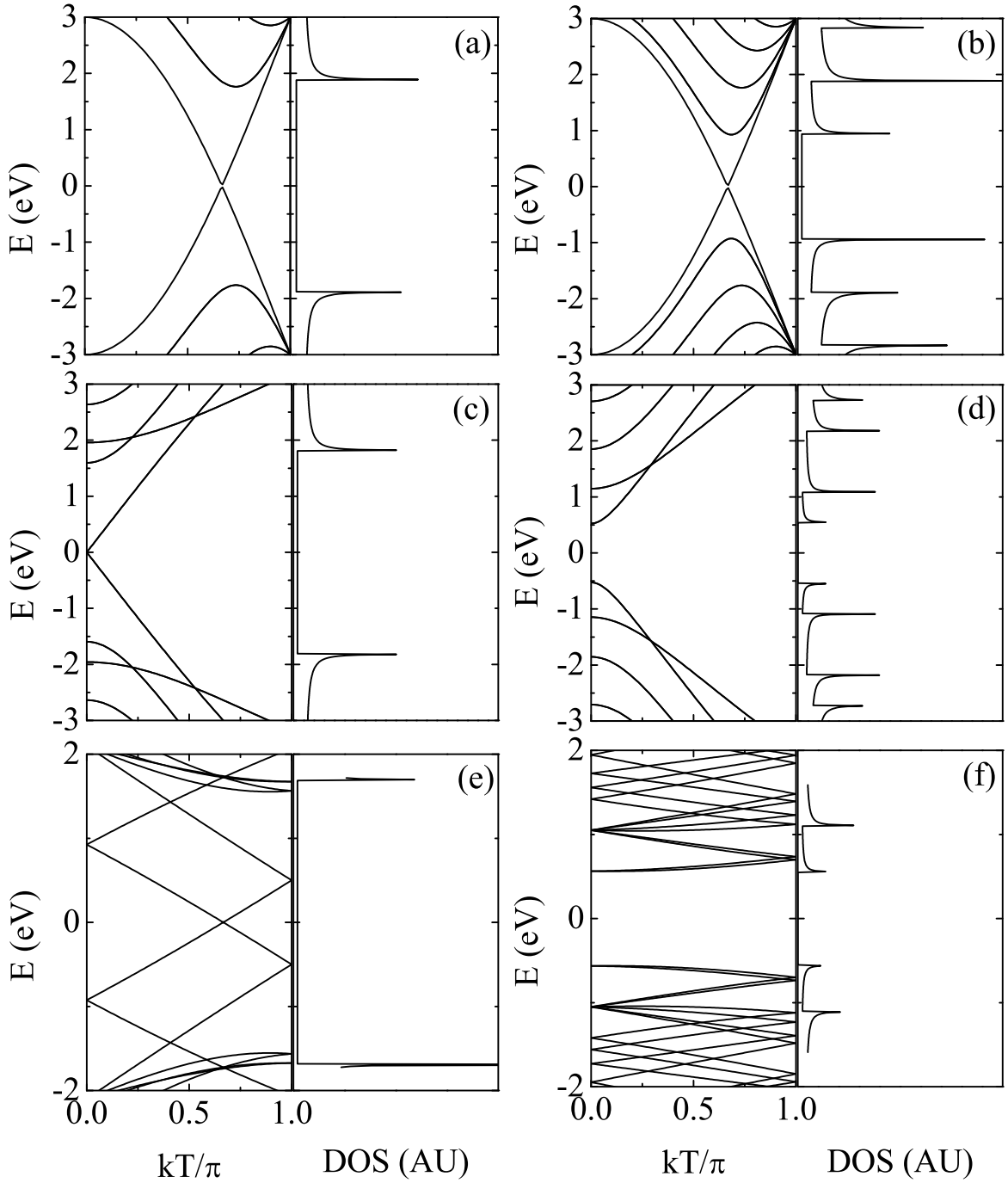

Figure 2.8. Dispersion relation and DOS of (a) (5,5), (b) (10,10), (c) (9,0), (d) (10,0), (e) (7,4), (f) (8,3) SWCNTs.

for other $n - m = 3l$, $l \neq 0$ SWCNTs, $\mathbf{k}$ will miss the K points. More rigorous calculations have shown the same result [**31**, **32**]. The small band gap caused by the curvature effect is [**32**, **33**],

$$E_g^c = \frac{\gamma_0 a^2}{4d_r^2} \cos 3\theta, \tag{2.17}$$

where θ is the chiral angle (see Table 2.1.). This curvature induced gap is inversely proportional to d_r^2. For an armchair SWCNT θ is 30° and the gap is zero. For a zigzag SWCNT, $\theta = 0$ and the gap is the largest among tubes of the same diameter.

After considering the curvature effect, the SWCNTs can be classified into three types. The armchair (n,n) SWCNTs are true metallic CNTs. The SWCNTs (n,m) where $n-m = 3l$, $l \neq 0$ are small band gap semiconductors while the rests are semiconductors. Therefore (5,5) and (10,10) SWCNTs are metallic, (9,0) and (7,4) SWCNTs have small band gaps, and (10,0) and (8,3) SWCNTs are semiconducting as shown in the last row of Table 2.2. For small band gap semiconducting SWCNTs with same chiral angle θ, the band gap is inversely proportional to the square of the tube radius R_t as given by Eqn. 2.17.

2.1.5. Single-walled carbon nanotube bundles

Due to the curvature effect, the only true metallic SWCNTs are armchair SWCNTs. This is explained by the high symmetry of (n,n) SWCNTs. When the armchair SWCNT forms a bundle, the symmetry is greatly reduced. Delaney *et al.* [**34**, **35**] calculated that for a (10,10) SWCNT rope, a pseudogap of 0.1 eV at the Fermi energy level is caused by the intertube interaction. Figure 2.10(a) shows a rope of (10,10) armchair SWCNTs. An isolated

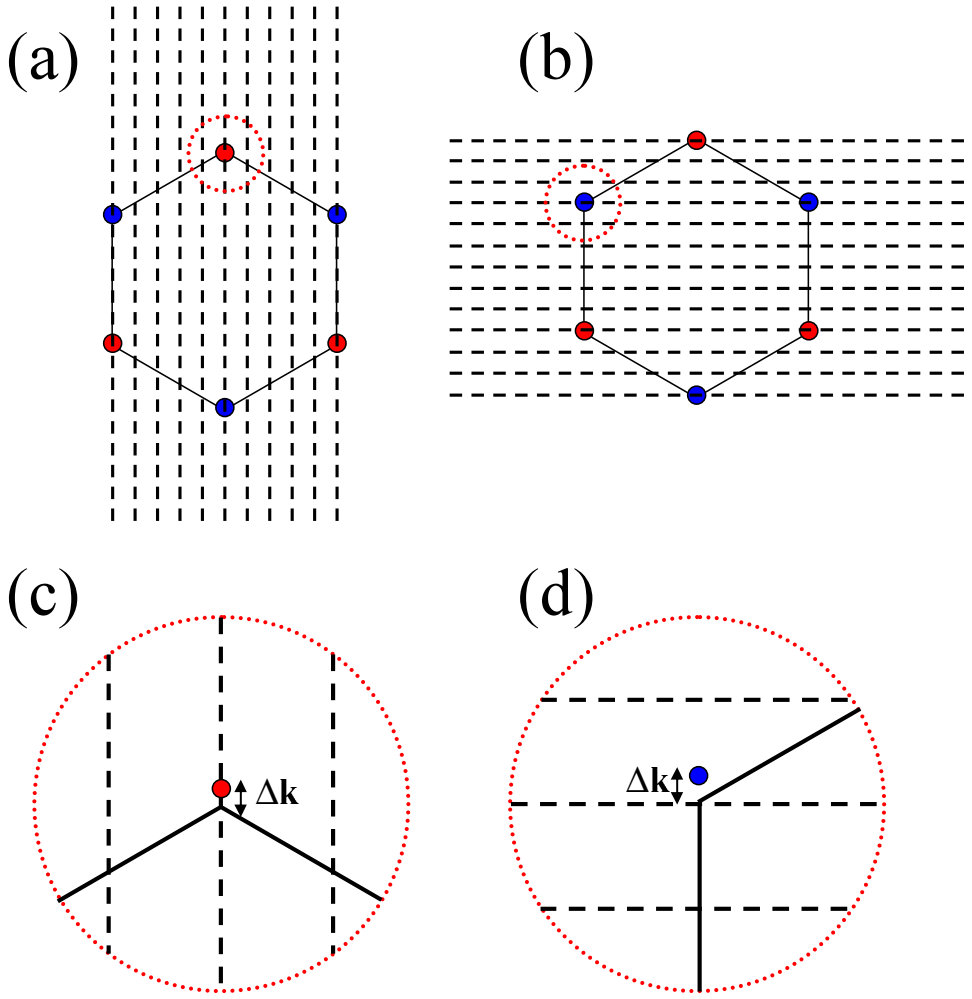

Figure 2.9. (Color) (a) The Brillouin zone and allowed **k** for an armchair nanotube ((5,5) tube shown here), (b) For a $n - m = 3l$ ($l \neq 0$) tube ((9,0) tube shown here), (c) the enlarged view of (a) at the K point. Due to the curvature effect, the K point can move. But by a symmetry argument, it can only shift vertically, thus the allowed **k** still passes through. (d) the enlarged view of (a) at the K point. Due to the curvature effect, the K point can move. But it shifts vertically, thus the shift can cause a mismatch for K and **k**.

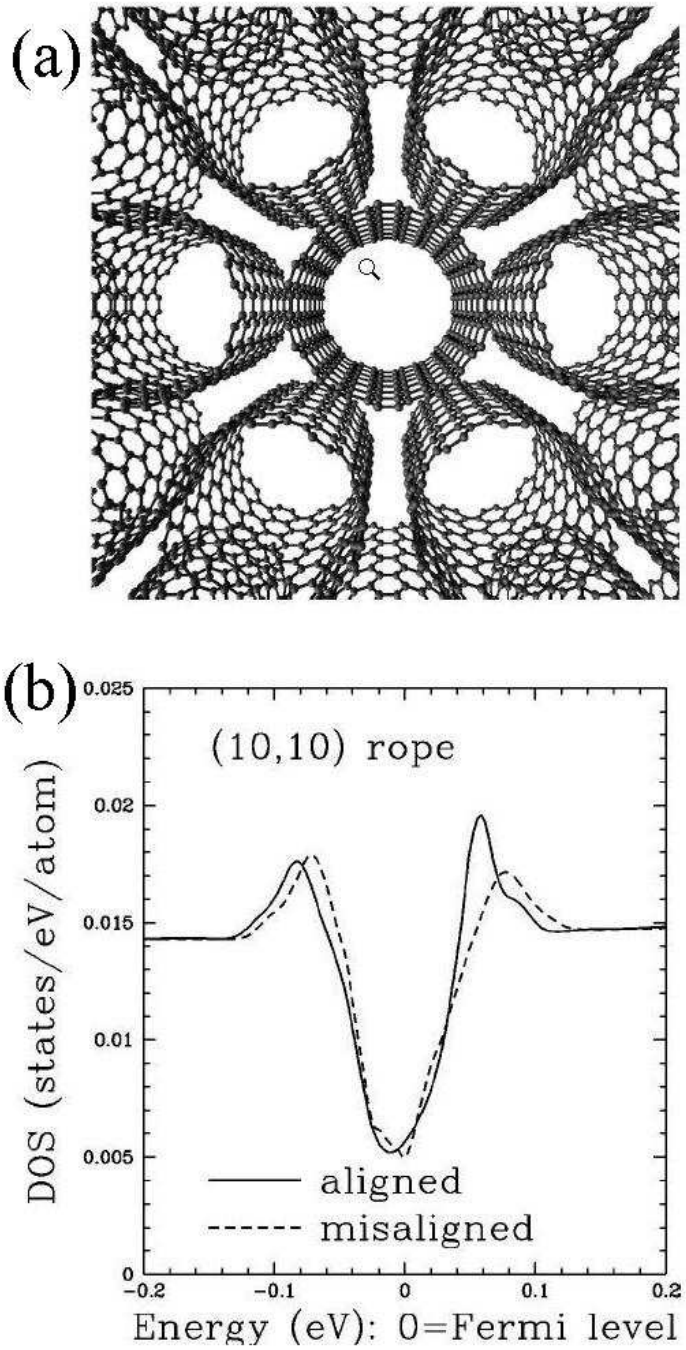

Figure 2.10. Psuedo gap in a (10,10) SWCNT rope caused by intertube interaction. (a) Perspective view of an aligned (10,10) SWCNT rope, (b) Calculated DOS for a (10,10) SWCNT rope with misaligned (dashed line) and aligned CNTs (solid line). Adapted from Ref. [**35**].

(10,10) SWCNT has the symmetry D_{20h} while the hexagonal packed structure has the D_{6h} symmetry. The highest common symmetry is D_{2h}. Figure 2.10(b) shows the pseudogap at the Fermi level.

2.1.6. Multiwalled nanotubes

MWNTs have been less studied due to their complexity. The simplest case is a double-walled carbon nanotube consisting of two concentric CNT shells. As the two coaxial CNT shells have different diameters d_t and circumferences L, in general, they will not be commensurate except in some special cases[4]. As shown in Table 2.1 and 2.2, the length of the translational vector T depends on the CNT chirality. T is 2.46 Å and 4.26 Å for armchair and zigzag CNTs respectively. Figure 2.5 gives a graphical representation of the unit cells of (5,5), (9,0) and (10,0) SWCNTs. For a random given (n,m), the unit cell can be fairly long. (e.g. (7,4) and (8,3) SWCNTs shown in Fig. 2.6; also refer to the value of T in Table 2.2.) Armchair and zigzag CNTs will not be commensurate with each other as $T = a$ for armchair and $T = \sqrt{3}a$ for zigzag CNTs. The commensurate cases are two armchair or two zigzag CNT shells. The general case is for the two CNTs (n_1, m_1) and (n_2, m_2) satisfying

$$\frac{n_1}{n_2} = \frac{m_1}{m_2} = r, \tag{2.18}$$

where the ratio r is a rational number. Figure 2.11 shows a commensurate and an incommensurate double-walled carbon nanotube. The calculation predicts that the CNT shells

[4]Commensurate means the ratio of the lengths of the unit cells for each shell along the tube axis is a rational number.

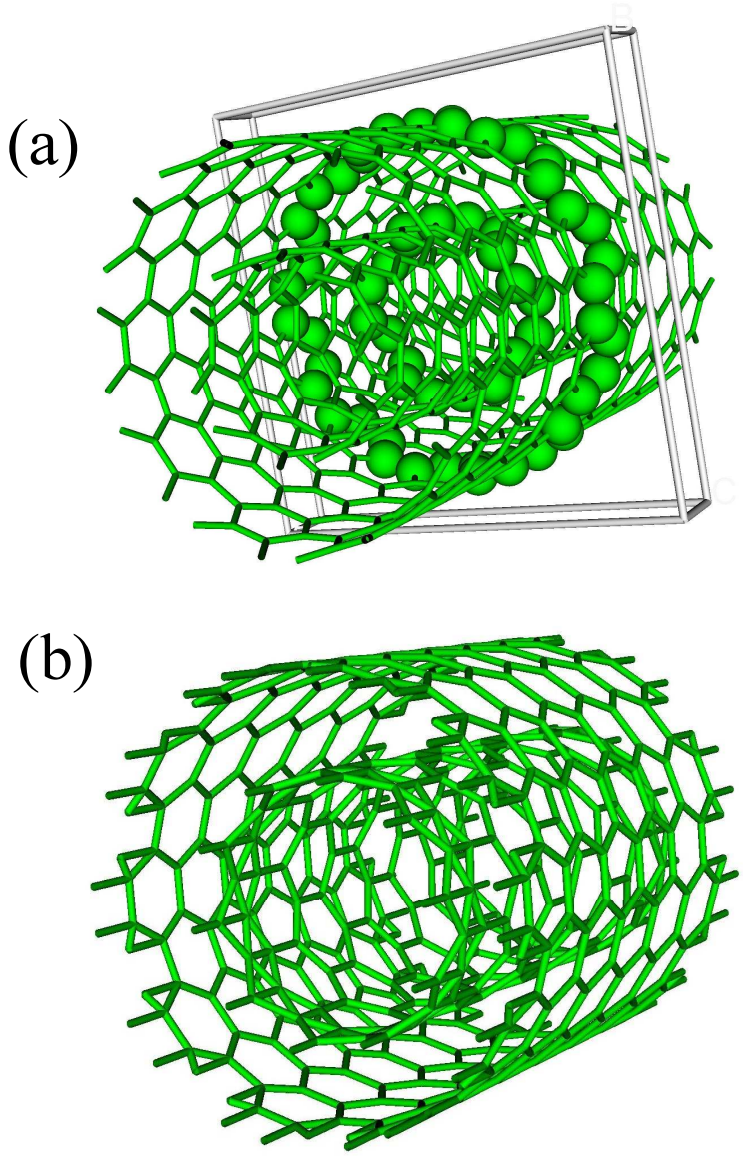

Figure 2.11. (Color) Geometric schematics[2] of (a) (5,5)-(10,10) commensurate CNT and (b) (10,0)-(10,10) incommensurate CNT. The unit cell in (5,5)-(10,10) CNT is shown in (a). There is no unit cell for the incommensurate CNT in (b).

of a coaxial MWNT retain the basic electronic properties (i.e. remain either metallic or semiconducting depending on their chirality) of the constituent shells even though the details of dispersion relation may be changed by the intertube interaction [**36**]. More recently, electron transport in commensurate and incommensurate MWNTs has been studied theoretically [**37**, **38**]. Diffusive transport behavior was explained by S. Roche *et al.* as a result of shells that are incommensurate [**38**]. However, K.H. Ahn *et al.* asserted that the diffusive, ballistic, or intermediate between them transport can all happen in incommensurate MWNTs. As can be seen, there is still lack of consensus about how the intra-shell interactions affect electron transport in MWNTs.

2.2. Overview of Mesoscopic Physics

2.2.1. Introduction

CNTs have diameters of a few up to a few tens of nanometers. For systems of this size, quantum effects and fluctuation cannot be ignored. In fact, even before the discovery of CNTs in 1991, scientists had studied the novel properties of conductors with at least one dimension in the nanometer scale. Conductors with dimensions on this length scale cannot be treated as classical conductors because the dimensions of the devices L, W are small enough to be comparable to or less than the mean free path length l_m, the phase coherence length l_φ, the thermal length l_T and/or the Fermi wavelength λ_F. They are also too large for the full quantum mechanical treatment as they consist of at least thousands of atoms. This size scale is called the mesoscopic scale as it lies between the macroscopic world where classical laws can be applied safely and the atomic world where the full quantum mechanics

must be used. The length scales mentioned above (such as l_m, l_φ, l_T and λ_F) are the most important parameters in mesoscopic physics.

Mesoscopic systems demonstrate interesting basic physics. Universal conductance fluctuation (UCF) [**39**, **40**] and weak localization (WL) [**41**] have been discovered in the diffusive transport regime. Conductance quantization [**42**] and the Luttinger liquid [**43**, **44**] have been studied in the ballistic transport regime. Quantum dots can act as artificial atoms [**45**] in which the Coulomb interaction plays an important role.

A brief overview of mesoscopic physics will be given in this section. We first introduce the various characteristic length scales in mesoscopic systems. The Landauer formula and ballistic transport is then discussed. Basic concepts of electron-electron interaction in ballistic systems are given in a short survey. Diffusive transport including UCF and WL will be discussed. We end this section by discussing Coulomb blockade in quantum dots.

2.2.2. Characteristic length scales

The Fermi wavelength $\lambda_F = 2\pi/k_F$ is the de Broglie wavelength of electrons at the Fermi energy level. The Fermi wave vector k_F is related to the Fermi velocity v_F and Fermi energy E_F by

$$v_F = \frac{\hbar k_F}{m} \tag{2.19}$$

$$E_F = \frac{\hbar^2 k_F^2}{2m}, \tag{2.20}$$

where m is the effective electron mass.

The mean free path l_m is the average length that an electron travels before being scattered by a scattering center. In transport, only electrons near the Fermi energy contribute, therefore we have

$$l_m = v_F \tau, \tag{2.21}$$

where τ is the relaxation time.

The phase coherence length l_φ is the length scale over which an electron maintains its phase coherence. In the ballistic regime

$$l_\varphi = v_F \tau_\varphi, \tag{2.22}$$

where τ_φ is the phase relaxation time. In the diffusive regime the phase coherence length is

$$l_\varphi = \sqrt{D\tau_\varphi}. \tag{2.23}$$

D is the diffusion constant given by

$$D = \frac{v_F^2 \tau}{d} = \frac{v_F l_m}{d}, \tag{2.24}$$

where d is the dimensionality of the sample.

l_φ defines the length scale of interference of the wave functions of a single electron state. However, interference can also be important for electron states that have close energies. At nonzero temperature, thermal averaging occurs over an energy scale of $k_B T$. Electrons with

an energy difference of k_BT lose their phase coherence after a time interval of the order of $\hbar/k_BT$. This corresponds to a length scale

$$l_T = \sqrt{\frac{D\hbar}{k_BT}}, \tag{2.25}$$

which is called the thermal length or the Thouless length. For a system of finite size L, we can define an energy scale named the Thouless energy

$$E_C = \frac{D\hbar}{L^2}. \tag{2.26}$$

Two states having energies close to each other are correlated. States with energy difference larger than E_C can be regarded as independent of each other. If $l_T > l_\varphi$, the dominant dephasing properties are defined by l_φ. On the other hand, if $l_T < l_\varphi$, the primary dephasing is due to thermal excitations and l_T is an important length scale for mesoscopic phenomena. The temperature dependence of mesoscopic phenomena is defined by both l_φ and l_T.

In mesoscopic systems, for 1D transport, if $L \gg l_m$, the transport is in the diffusive regime. In the ballistic regime, $L \ll l_m$ and the electrons experience no or few scattering events inside the conductor. The sample boundary plays an important role for scattering instead of impurities.

2.2.3. Ballistic transport and Landauer formula

For an ideal conductor, there is no scattering inside the conductor and the resistance should be zero. But the resistance from the interface between the conductor and the conducting pads is not zero because of the mode mismatch of the conductor and the contact pads.

In a ballistic conductor, the electrons entering the conductor from one side will be transported to the other side without any scattering. For each subband, the net current from one side to the other side when one applies a voltage difference V across the conductor is [**46**]

$$I = \frac{2e}{h} \int d\,\mathcal{E}(f(\mathcal{E} - \frac{eV}{2}) - f(\mathcal{E} + \frac{eV}{2})), \tag{2.27}$$

where $f(\mathcal{E}-\mu) = \frac{1}{e^{(\mathcal{E}-\mu)/k_B T}+1}$ is the Fermi distribution function. At zero temperature $T = 0$,

$$I = \frac{2e^2}{h} V \tag{2.28}$$

Therefore, the conductance of a ballistic conductor that has M subbands at zero temperature is

$$G = \frac{I}{V} = \frac{2e^2}{h} M. \tag{2.29a}$$

The resistance is

$$R = \frac{1}{G} = \frac{h}{2e^2} \frac{1}{M}. \tag{2.29b}$$

This means the conductance will be a multiple of $2e^2/h$ and independent of length. As discussed in the previous section, in real experiments, ballistic transport can only be achieved

if the sample length L is much smaller than the mean free path l_m and phase coherence length l_φ.

As an ideal quantum wire has a finite resistance, there must be dissipation if current flows through the wire. As the resistance is only at the contacts not inside the wire, this means the dissipation occurs at the contacts. When the current is large enough, due to heat dissipation, the contacts will be burned before the wire. This has been used as an additional proof that transport is ballistic in MWNTs [**47**].

In non-ideal systems with multiple subbands, there is a certain probability R that an electron entering the conductor will get reflected and a probability T that it will be transmitted. These two probabilities obey a simple relation $R + T = 1$. Here we assume the transmission probability T is the same for all subbands. The conductance of this system is then [**46**]

$$G_C = \frac{I}{V} = \frac{2e^2}{h} MT, \tag{2.30a}$$

and the resistance is

$$R_C = \frac{h}{2e^2} \frac{1}{MT} \tag{2.30b}$$

Equation 2.30a is called the two-terminal Landauer formula because it includes the contacts. If the contacts are not included, Eqns. 2.30 become [**46**]

$$G_S = \frac{2e^2}{h} \frac{MT}{R} \tag{2.31a}$$

$$R_S = \frac{h}{2e^2} \frac{R}{MT}, \tag{2.31b}$$

where G_S (R_S) is the conductance (resistance) from the scatterers inside the wire.

If the transmission probability is not the same for all subbands, we can define $T_{ij} = |t_{ij}|^2$ as the probability for an electron from the jth subband to be transmitted to the ith subband in the other lead and $R_{ij} = |r_{ij}|^2$ as the probability of an electron being reflected from the jth subband to the ith subband. Here the transmission and reflection amplitudes t_{ij} and r_{ij} are elements in the scattering matrix

$$\begin{pmatrix} o_{L1} \\ o_{L2} \\ \dots \\ o_{LM} \\ o_{R1} \\ \dots \\ o_{RM} \end{pmatrix} = \begin{pmatrix} r_{11} & r_{12} & \dots & r_{1M} & t_{11} & t_{21} & \dots & t_{M1} \\ r_{21} & r_{22} & \dots & r_{2M} & t_{12} & t_{22} & \dots & t_{M2} \\ \dots & & & & & & & \\ r_{M1} & r_{M2} & \dots & r_{MM} & t_{1M} & t_{2M} & \dots & t_{MM} \\ t_{11} & t_{12} & \dots & t_{1M} & r_{11} & r_{21} & \dots & r_{M1} \\ \dots & & & & & & & \\ t_{M1} & t_{M2} & \dots & t_{MM} & r_{1M} & r_{2M} & \dots & r_{MM} \end{pmatrix} \begin{pmatrix} i_{L1} \\ i_{L2} \\ \dots \\ i_{LM} \\ i_{R1} \\ \dots \\ i_{LM} \end{pmatrix}. \tag{2.32}$$

where $o(i)_{Ln}$ means the outgoing (incoming) electron wave amplitude of mode n in the left lead, and similarly $o(i)_{Rn}$ for the right lead. We can define a $2M$ by $2M$ matrix as

$$\mathbf{S} = \begin{pmatrix} \mathbf{r} & \mathbf{t}^T \\ \mathbf{t} & \mathbf{r}^T \end{pmatrix}. \tag{2.33}$$

The scattering matrix is a unitary matrix defined as

$$\mathbf{O} = \mathbf{SI}, \tag{2.34}$$

where **O** (**I**) is the column vectors representing the outgoing (incoming) wave amplitudes in the different subbands in the leads as

$$\mathbf{O}(\mathbf{I}) = \begin{pmatrix} o(i)_{L1} \\ o(i)_{L2} \\ \cdots \\ o(i)_{LM} \\ o(i)_{R1} \\ o(i)_{R2} \\ \cdots \\ o(i)_{LM} \end{pmatrix}. \tag{2.35}$$

We note that unitary matrix **S** satisfies the relation $\mathbf{S}^{+}\mathbf{S} = \mathbf{I} = \mathbf{S}\mathbf{S}^{+}$. The corresponding equations of Eqn. 2.30a, 2.31a are [**48**]

$$G_C = \frac{2e^2}{h}\sum_i T_i = \frac{2e^2}{h} tr\, \mathbf{t}\mathbf{t}^{\dagger} \tag{2.36}$$

$$G_S = \frac{2e^2}{h}\frac{2\sum_i T_i \sum_i 1/v_i}{\sum (1 + R_i - T_i)/v_i}, \tag{2.37}$$

where $T_i = \sum_j T_{ij}$, $R_i = \sum_j R_{ij}$, v_i is the electron velocity in the ith subband.

For a four-terminal device shown schematically in Fig. 2.12, in the weak coupling limit that the voltage probes lead 3 and 4 are only weakly connected to the sample, the four-terminal resistance is given by [**49**]

$$R_{12,34} = \frac{h}{2e^2}\frac{1}{T_{12}^{(0)}}\frac{T_{31}T_{42} - T_{32}T_{41}}{(T_{31} + T_{32})(T_{41} + T_{42})}, \tag{2.38}$$

where $T_{12}^{(0)}$ is the transmission without the presence of other leads. If leads 3 and 4 are strongly coupled, Eqn. 2.38 takes a more complex form

$$R_{12,34} = \frac{h}{2e^2}(T_{31}T_{42} - T_{32}T_{41})/D, \tag{2.39}$$

where D is a sample-specific constant independent of the index $1, 2, 3, 4$ [**50**]. In a magnetic field B, the two-terminal resistance is symmetric with respect to B, $R_C(B) = R_C(-B)$. For the four-terminal resistance, the relation is generally not true

$$R_{mn,kl}(B) \neq R_{mn,kl}(-B). \tag{2.40}$$

The correct relation given by the Landauer-Büttiker equation is [**50**]

$$R_{mn,kl}(B) = R_{kl,mn}(-B). \tag{2.41}$$

This means that when we reverse the magnetic field and exchange the current and voltage leads, the resistance (conductance) will be the same. The reciprocal relation has been experimentally observed first by Benoit *et al.* [**51**].

2.2.4. Electron-electron interaction

The Landauer formular discussed in the previous section gives the quantized conductance in the ballistic transport case. This formula was derived without the consideration of electron-electron interaction. In the three dimensional case, the electron-electron interaction can be treated as a perturbation within the frame work of Fermi liquid theory [**24**]. Fermi liquid theory states that there is a one to one correspondence between the low energy excitations of a free Fermi gas and those of an interacting electron liquid. These excitations are called "quasiparticles". As a result of the Pauli exclusion principle and the conservation law of momentum and energy, the availabe phase space for electron-electron scattering at low energies (e.g. $k_B T \ll E_F$) is small compared with the large phase space available in 3D [**24**,**52**]. The electron-electron scattering rate is small compared with the dominant scattering mechanism (e.g. the electron elastic scattering rate). The correlations in the electron system are weak, although the interactions may be strong. For one-dimensional systems, because the momentum and energy conservation law are actually the same ($E - E_F \approx v(p - p_F)$), they are not as restrictive as in the 3D case. Perturbation corrections describing even weak electron-electron interaction are divergent. The electron-electron interactions will remove the sharp Fermi surface. The ground state is non-perturbative and it is described as a Luttinger liquid [**52**–**54**]. In a 1D system, even weak interactions can result in strong correlations. According to Luttinger liquid theory, the charge and spin excitations are collective modes (plasmons) described by boson modes. The charge and spin modes have different excitation energies and propagate at different velocities in the presence of interactions. This leads to

spin-charge separation, a peculiar effect predicted by Luttinger liquid theory. In transport, Luttinger liquid theory predicts the conductance to be

$$G = g\frac{e^2}{h}, \tag{2.42}$$

where the correlation exponent g is a dimensionless parameter (the dimensionless conductance). $g = 1$ for the non-interacting case, $g < 1$ for repulsive interactions, and $g > 1$ for attractive interactions. However, for a 1D wire of finite length L connected to Fermi liquid contacts, Luttinger liquid behavior will be cut off at temperatures T for which ($\hbar v_F/k_B T \geq L$) [**55**]. If the coupling is weak and transport is limited by tunneling, the tunneling DOS demonstrates a power law dependence with energy,

$$\nu(E) \propto E^{\alpha}, \tag{2.43}$$

where the exponent α depends on the contact geometry. For an armchair SWCNT with tunneling contacts made to its ends [**56**],

$$\alpha = (\frac{1}{g} - 1)/4, \tag{2.44a}$$

while for an armchair SWCNT with tunneling contacts made to its body,

$$\alpha = (\frac{1}{g} + g - 2)/8. \tag{2.44b}$$

The temperature T and voltage dependence V of the conductance is given by [**56**]

$$G(V,T) = AT^{\alpha}\cosh(\frac{eV}{(2k_BT)})|\Gamma(\frac{1+\alpha}{2}+\frac{ieV}{2\pi k_BT})|^2, \tag{2.45a}$$

$$\propto \begin{cases} T^{\alpha} & eV \ll k_BT \\ V^{\alpha} & eV \gg k_BT \end{cases} \tag{2.45b}$$

where Γ is the gamma function and A is a prefactor.

Armchair SWCNTs are believed to be Luttinger liquids [**25**]. There is some experimental evidence that supports this claim [**57**,**58**], but further experiments are needed to unambiguously prove that SWCNTs are Luttinger liquids. The experimental details will be discussed in the next section.

2.2.5. Interference in diffusive transport

In the ballistic transport regime, the length scale of the sample L satisfies $L \ll l_m, l_\varphi$, where l_m and l_φ are the mean free path and phase coherence length, respectively. In the diffusive regime, the sample length satisfies $l_m \ll L \ll l_\varphi$. This means that as an electron moves through the conductor, it will experience some elastic scattering as $L \gg l_m$ but still maintain phase coherence as $L \ll l_\varphi$. This leads to many interesting phenomena such as WL, UCF, and the Aharonov-Bohm effect. We will follow Ref. [**59**] to give a brief review of these phenomena.

As shown in Fig. 2.13(a), in electron transport, there are many paths for electrons to go between two points within a conductor. There are also paths like that are shown in Fig.

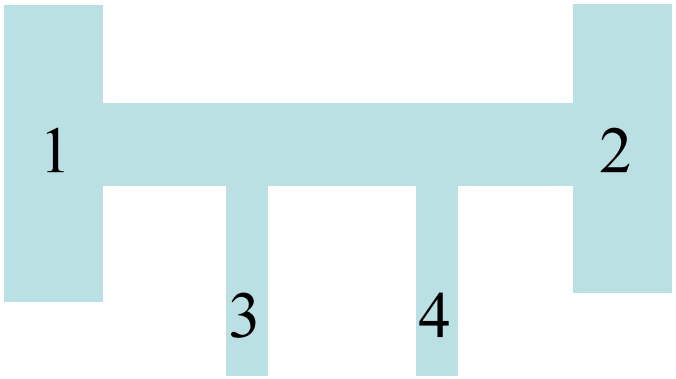

Figure 2.12. (Color) Schematic of a four terminal measurement. The current is driven from lead 1 to lead 2. The voltage probes are lead 3 and lead 4.

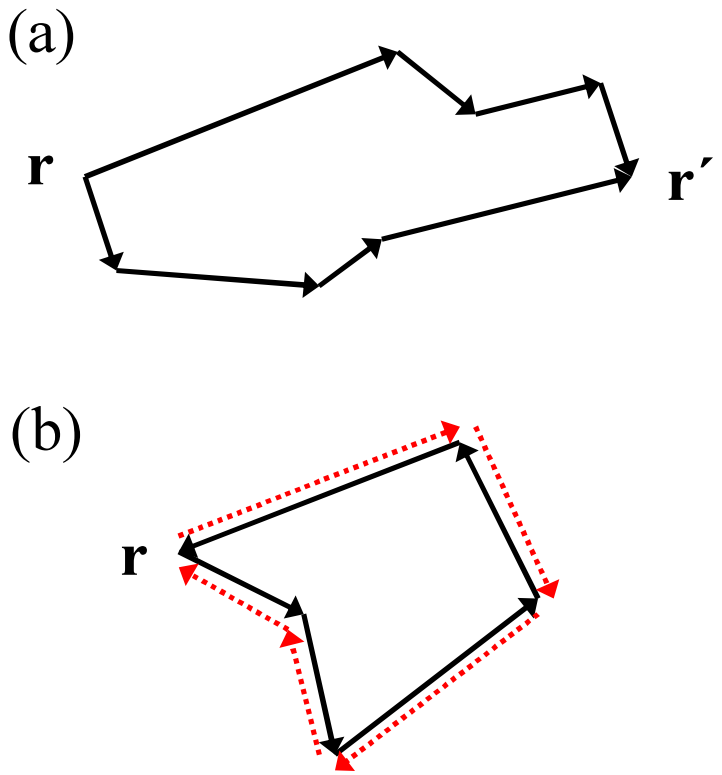

Figure 2.13. (Color) Mechanism of coherent backscattering. **(a)**: the path for electron travels from r to r'. **(b)** the path for electron travels back to r. For each such path, there is a reverse path as shown in the dashed line.

2.13(b) for the electron to return back to r. At zero magnetic field, for each such path there is another path for the electron to travel backwards like shown in dashed line in the Fig. 2.13(b). In the Feynman path integral formalism, the probability of propagating from r to r' during a time t is

$$P(r, r', t) = |\sum_i A_i|^2 = \sum_i |A_i|^2 + \sum_{i \neq j} A_i A_j^*, \tag{2.46}$$

where the A_i are probability for each single trajectory i connecting r and r'. The classical diffusion probability corresponds to the first term, while the second term describes quantum interference. If r and r' are different, the phase difference is uncorrelated over all trajectories. However, if r and r' are same, $P(r, r, t)$ will describe all closed loop trajectories. In the absence of magnetic field, time-reversal invariance implies that A^+, A^- (for clockwise and counterclockwise propagation respectively) are the same, i.e. $A^+ = A^- = A$.

$$P(r, r, t) = |A^+ + A^-|^2 = |A + A|^2 = 4|A|^2. \tag{2.47}$$

The enhanced coherent backscattering is called WL and it can be suppressed by a small magnetic field, as a magnetic field will break the reversal symmetry of such paths so that $A^+ \neq A^-$. When a magnetic field is applied, the phase difference acquired between the clockwise and counter-clockwise paths is

$$\begin{aligned} \varphi &= h^{-1} \oint_+ p^+ \cdot dl - h^{-1} \oint_- p^- \cdot dl \\ &= \frac{2e}{h} \int (\Delta \times A) \cdot dS = \frac{2eBS}{h} \equiv \frac{2S}{L_m^2} \equiv 4\pi \frac{\Phi}{\Phi_0}. \end{aligned} \tag{2.48}$$

The phase difference is twice the enclosed area S divided by the square of the magnetic length $L_m \equiv (\hbar/eB)^{1/2}$, or alternatively, it is 4π times the enclosed flux Φ in units of the elementary flux quantum $\Phi_0 \equiv h/e$.

This suppression can be used to directly measure the phase coherence length of the electrons. In a magnetic field, the paths with an area larger than L_m^2 lose phase coherence and do not contribute to the interference. In 1D, the WL correction is given by ($L_\varphi, L_m \gg W \gg L_{el}$) [**60**]

$$\Delta G_{WL}^{1D} = -\frac{e^2}{\pi\hbar}\frac{1}{L}\left[\frac{3}{2}(\frac{1}{D\tau_\varphi}+\frac{4}{3D\tau_{SO}}+\frac{1}{D\tau_B})^{-1/2}-\frac{1}{2}(\frac{1}{D\tau_\varphi}+\frac{1}{D\tau_B})^{-1/2}\right], \tag{2.49}$$

where $\tau_B = (3L_m^4)/(W^2D)$, τ_{SO} is the spin-orbit scattering time and D is the diffusion constant. The characteristic magnetic field B_c for the suppression of 1D WL is [**59**]

$$B_c = \begin{cases} \frac{\hbar}{e}\frac{\sqrt{3}}{Wl_\varphi} & l_m \ll W \\ \frac{\hbar}{e}\frac{1}{W}\sqrt{\frac{C_1}{Wv_F\tau_\varphi}} & L_m^2 \gg Wl_m, l_m \gg W \\ \frac{\hbar}{e}\frac{C_2 l_m}{W^2 v_F\tau_\varphi} & Wl_m \gg L_m^2 \gg W^2, l_m \gg W \end{cases} \tag{2.50}$$

where C_1, C_2 are constants depending on boundary scattering conditions. For specular scattering, it is found that $C_1 = 9.5$ and $C_2 = 4.8$, while for diffusive scattering, $C_1 = 4\pi$ and $C_2 = 3$.

UCF is another feature in diffusive transport [**61**]. The electrons can pass through the disordered conductor through many paths. Those paths interfere with each other and the conductance is determined by their phase difference. When the configuration of the

impurities changes, the phase difference between different paths will change and can cause fluctuations on the order of e^2/h. To understand this behavior, we start from the Landauer formula

$$G = \frac{e^2}{h} \sum_{i,j=1}^{M} |t_{ij}|^2, \tag{2.51}$$

where M is the total number of subbands. The variance of the conductance is

$$< (\delta G)^2 >=< G^2 > - < G >^2 \tag{2.52}$$

With

$$\sum |t_{ij}|^2 = M - \sum |r_{ij}|^2, \tag{2.53}$$

we obtain

$$< \delta G^2 >= (\frac{e^2}{h})^2 (\delta(\sum |r_{ij}|^2)) = (\frac{e^2}{h})^2 M^2 (\delta |r_{ij}|^2)^2, \tag{2.54}$$

where

$$(\delta |r_{ij}|^2)^2 \equiv< |r_{ij}|^4 > - < |r_{ij}|^2 >^2 . \tag{2.55}$$

As there is no correlation between different reflective paths,

$$< |r_{ij}|^4 >= 2 < |r_{ij}|^2 >^2 . \tag{2.56}$$

In the diffusive limit $< |r_{ij}|^2 >= 1/M$. We can get

$$(\delta G)^2 \approx 2(\frac{e^2}{h})^2, \tag{2.57}$$

$$\delta G \approx \sqrt{2}\frac{e^2}{h}. \tag{2.58}$$

The detailed calculation yields [**59**]

$$\delta G = \frac{g_s g_v}{2}\beta^{-1/2} C \frac{e^2}{h}. \tag{2.59}$$

Here C is a constant that depends on the shape of the sample. $C \approx 0.73$ in a narrow channel with $L \ll W$. $\beta = 1$ in a zero magnetic field and $\beta = 2$ when time-reversal symmetry is broken with magnetic field. $g_s g_v$ account for spin and valley degeneracies. Recall that the phase coherence length $l_\varphi \equiv (D\tau_\varphi)^{-1/2}$ and the thermal length $l_T \equiv (\hbar D/k_B T)^{1/2}$. At non-zero temperature, for $l_\varphi \ll l_T, L$ [**59**],

$$\delta G = \frac{g_s g_v}{2}\sqrt{\beta}\sqrt{12}(\frac{e^2}{h}\frac{l_\varphi}{L})^{3/2}, \tag{2.60a}$$

and for $l_T \ll l_\varphi \ll L$,

$$\delta G = \frac{g_s g_v}{2}\sqrt{\beta}(\frac{8\pi}{3})^{1/2}\frac{e^2}{h}\frac{l_T l_\varphi^{1/2}}{L^{3/2}}. \tag{2.60b}$$

For the intermediate temperature regime when $l_\varphi \approx l_T$,

$$\delta G = \frac{g_s g_v}{2}\beta^{-1/2}\sqrt{12}\frac{e^2}{h}(\frac{l_\varphi}{L})^{3/2}[1 + \frac{9}{2\pi}(\frac{l_\varphi}{l_T})^2]^{-1/2}. \tag{2.60c}$$

The above calculated value is in regard to change of impurity configuration in the sample. Experimentally, it is not practical to deliberately change the impurity configuration of the sample, rather it can be done by changing the magnetic field or Fermi energy by means of a gate. UCF manifests itself as a random fluctuation on the order of e^2/h on sweeping magnetic field or gate voltage. This random fluctuation depends on the impurity configuration, thus the pattern is sample-specific but reproducible in the same sample. The sample reproducibility holds as long as the configuration of impurities in the sample does not change, such as can be caused by thermal annealing.

As a magnetic field can change the relative phase of different paths, the conductance fluctuation can be characterized by a correlation field defined by

$$C(\Delta B) =< g(B)g(B+\Delta B) > - < g(B) >^2 . \tag{2.61}$$

The correlation function has a normal decay with the correlation field ΔB_c defined by the equation $C(\Delta B_c) = 0.5 \times C(0)$. In the dirty limit,

$$\Delta B_c = 2\pi C \frac{\hbar}{e} \frac{1}{W l_\varphi}, \tag{2.62}$$

where the prefactor C decreases from 0.95 for $l_\varphi \gg l_T$ to 0.42 for $l_\varphi \ll l_T$.

The phase coherence length l_φ decreases with increasing temperature. There are three mechanisms that may contribute to electron dephasing: electron-phonon scattering, electron-electron scattering and scattering from impurities which have an internal degree of freedom (e.g. magnetic impurities). It is known that in the absence of an extrinsic noise source or

magnetic impurities, the dominant source of dephasing in metallic thin films is electron-phonon interactions above about 1 K, while at low temperatures, electron-electron interactions are the leading source of dephasing. If only electron-electron interactions are taken into account, the phase coherence length in 1D is given by [**62**],

$$l_\varphi = (\frac{DG_D L\hbar^2}{2e^2 k_B T})^{\frac{1}{3}}, \tag{2.63a}$$

$$\sim T^{-\frac{1}{3}}, \tag{2.63b}$$

where G_D is the classical Drude conductance of the sample.

2.2.6. Quantum dot physics

A typical quantum dot is a metallic island with two metallic electrodes close by. This island is isolated from its surroundings except for tunneling between the electrodes and the island. A third electrode is sometimes used as a gate but it is only capacitively connected to the central island[5]. The two electrodes are also referred to as source and drain as electrons can tunnel from the source to the island and then from the island to the drain. The typical size of quantum dots is about a few tens to a few hundred nanometers. When electrons tunnel from the source to the quantum dot, the extra charge creates a change of $e^2/2C_\Sigma$ in electrostatic potential of the dot. C_Σ is the total capacitance of the quantum dot coupled to the environment. In a large system where C_Σ is large, the change is hardly noticeable. However, in a small quantum dot, the potential change would be greater than the thermal

[5]Capacitively connected means it can change the chemical potential in the island, but no electron tunneling is allowed.

energy at low temperatures. The other constraint is that the quantum fluctuation of the charge number n in the dot must be sufficiently small. For this latter constraint to hold, the tunneling resistance R_t must be sufficiently large. These two conditions can be written as,

$$\frac{e^2}{2C_\Sigma} \gg k_B T, \tag{2.64a}$$

$$R_t \gg \frac{h}{e^2}. \tag{2.64b}$$

If these conditions are satisfied, Coulomb repulsion will prevent another electron tunneling into the quantum dot before the first electron tunnels out of the quantum dot. This causes a blockade of electron transport [**63**].

When one applies a source-drain bias voltage V and a gate voltage V_g as shown in Fig. 2.14, the total electrostatic energy is

$$\begin{aligned} E_s &= \frac{Q_1^2}{2C_1} + \frac{Q_2^2}{2C_2} + \frac{Q_g^2}{2C_g} \\ &= \frac{1}{2C_\Sigma}(C_g C_1 (\frac{V}{2} - V_g)^2 + C_1 C_2 V^2 + C_g C_2 (\frac{V}{2} + V_g)^2 + Q^2), \end{aligned} \tag{2.65}$$

where $Q_{g(1,2)}$ is the charge in the gate (lead 1,2). $Q = Q_1 - Q_2 - Q_g$ is the net charge on the island. The work done by the batteries is

$$W = Q_1(\frac{C_2}{C_\Sigma}V + \frac{C_g}{C_\Sigma}(\frac{V}{2} - Vg)) + Q_2(\frac{C_1}{C_\Sigma}V - \frac{C_g}{C_\Sigma}(\frac{V}{2} - V_g)). \tag{2.66}$$

The total energy in the system is

$$E = E_s - W. \tag{2.67}$$

The change of the total energy of the system for an electron tunneling through junction 1 is [**63**]

$$\Delta E_1^{\pm} = \frac{e}{C_\Sigma}[-\frac{e}{2} \mp (en - Q_p + C_2 V + C_g(\frac{V}{2} - V_g))], \tag{2.68}$$

where n is the net number of electrons on the dot, Q_p is the random charge trapped in the system near the junction. Q_p is responsible for the asymmetries in the experimental I-V characteristics. $C_\Sigma = C_1 + C_2 + C_g$ is the total capacitance of the quantum dot. Similarly, the change of energy of the system for an electron to tunnel through junction 2 is

$$\Delta E_2^{\pm} = \frac{e}{C_\Sigma}[-\frac{e}{2} \pm (en - Q_p - C_1 V - C_g(\frac{V}{2} + V_g))]. \tag{2.69}$$

For the jth junction, the total rate from occupied states on the left (right) to unoccupied states on the right (left) is given by [**63**]

$$\Gamma_j^{\pm}(V) = \frac{1}{eR_{tj}} \frac{\Delta E_j^{\pm}/e}{1 - e^{-\Delta E_j^{\pm}/k_B T}}, \qquad (j = 1, 2) \tag{2.70}$$

where R_{tj} is the resistance of the jth tunnel junction.

Let $P(n)$ be the probability of finding n electrons on the island. The evolution of $P(n)$ for this double junction is given by the master equation [**63**]

$$\frac{\partial P(n)}{\partial t} = \Gamma_1^+(n-1)P(n-1) + \Gamma_1^-(n+1)P(n+1) - [\Gamma_1^+(n) + \Gamma_1^-(n)]P(n)$$
$$+\Gamma_2^-(n-1)P(n-1) + \Gamma_2^+(n+1)P(n+1) - [\Gamma_2^-(n) + \Gamma_2^+(n)]P(n) \qquad (2.71)$$

For a stationary state

$$\frac{\partial P(n)}{\partial t} = 0 \qquad (2.72)$$

The solution of Eqn. 2.72 is

$$[\Gamma_1^-(n+1) + \Gamma_2^+(n+1)]P(n+1) = [\Gamma_1^+(n) + \Gamma_2^-(n)]P(n). \qquad (2.73)$$

As we know that the total probability must be one.

$$\sum_n P(n) = 1 \qquad (2.74)$$

$P(n)$ can be calculated by solving Eqns. 2.72 and 2.74. The current is given by

$$I = e\sum_n P(n)[\Gamma_{1,2}^-(n) - \Gamma_{1,2}^+(n)]. \qquad (2.75)$$

The I-V characteristic can be calculated from Eqns. 2.72, 2.74 and 2.75. Figure 2.15(a) is a simulation of the single electron tunneling effect at zero temperature. The characteristic rhombic shape is know as "Coulomb blockade diamonds". As the temperature increases, the conductance at zero voltage becomes a small but nonzero value. The pattern of the

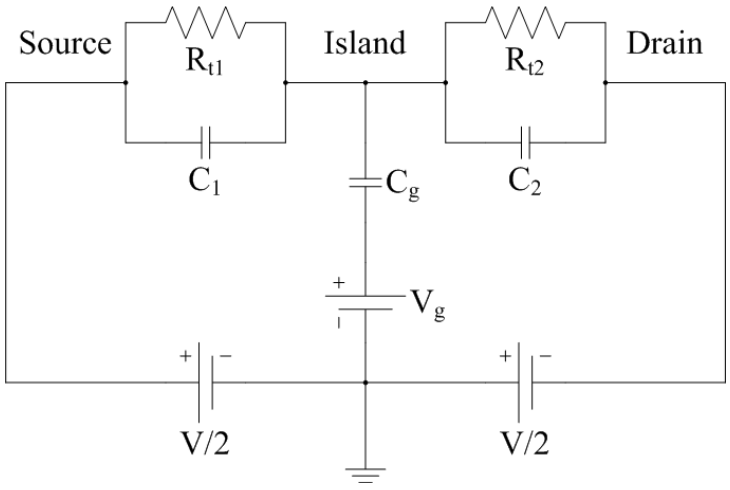

Figure 2.14. Equivalent electric circuit diagram for a quantum dot.

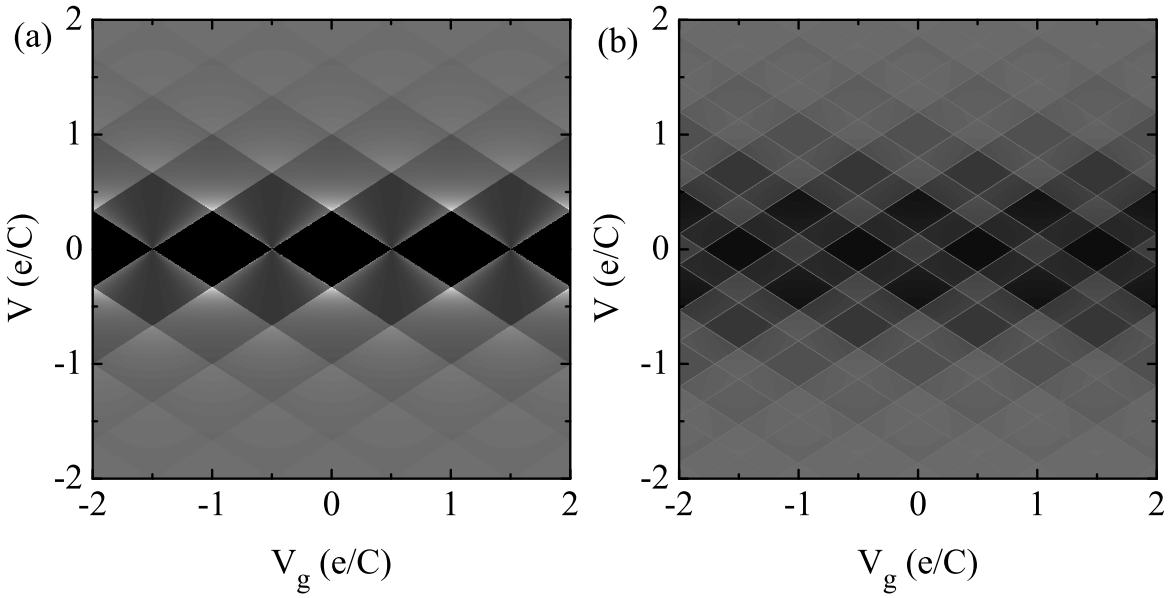

Figure 2.15. The simulated conductance of a quantum dot as a function of V_g and V at (a) $T = 0$, (b) $k_BT/eV = 0.1$ (Darker means lower conductance). For each junction, the tunneling resistance $R_{t1} = R_{t2}$ and the capacity $C_1 = C_2 = C_g = C_\Sigma/3 = C$. The voltages are in units of e/C.

"diamonds" also changes instead of being merely smeared by temperature as shown in Fig. 2.15(b).

If the conductance is high enough that the number of electrons is not well defined, or the total capacitance is so large that the charging energy is too small compared to other energy scales (e.g. k_BT), the Coulomb blockade effect will be absent and the transport reduces to double barrier tunneling neglecting electron-electron interaction. Generally speaking, for a resonant system such as a double tunneling barrier system, the transmission is

$$T(E) = \frac{\Gamma_1\Gamma_2}{(E-E_0)^2 + \frac{1}{4}(\Gamma_1+\Gamma_2)^2}. \tag{2.76}$$

The $\Gamma_{1(2)}/\hbar$ are the escape rates for the 1 (2) leads. E_0 is the resonant energy and $T(E_0)$ is the transmission when on resonance. Equation 2.76 is valid for both coherent tunneling and sequential tunneling and is often called the Breit-Wigner form [**46**]. Scattering processes between the barrier have little effect on the resonant form. If the two barriers are symmetric, $\Gamma_1 = \Gamma_2 = \Gamma/2$, Eqn. 2.76 is then,

$$T(E) = T(E_0)\frac{1}{1+(\frac{E-E_0}{\Gamma/2})^2}. \tag{2.77}$$

We can see that the transmission will drop to the half of the transmission on resonance when $E - E_0 = \Gamma/2$. Therefore Γ is the full width of the resonance.

Coulomb blockade effects can also appear in an unconventional way. Egger *et al.* [**64**] found that an interacting, disordered conductor that acts as high-impedance transmission line, connected only by tunnel junctions so that the level broadening is negligible, has the

tunneling DOS that obeys a power law behavior

$$\nu(E) \propto E^{\alpha}. \tag{2.78}$$

This is very similar to the tunneling DOS of Luttinger liquid in Eqn. 2.43. It can be understood as arising from the charge that has been transferred to one-dimensional plasmon modes in such a disordered wire. Therefore the tunneling conductance is

$$G(T) \propto T^{\alpha}, \tag{2.79a}$$

$$G(V) \propto V^{\alpha}, \tag{2.79b}$$

where T is the temperature, V is the bias voltage and α is given by Eqn 2.44. The similarity between the Luttinger liquid and unconventional Coulomb blockade has generated a lot of interest for finding unambiguous ways to determine genuine Luttinger liquid behavior.

2.2.7. Fano resonances

The theory of Fano resonances was first developed by Fano to explain the asymmetric lineshape in the spectra of rare gases. Fano's model takes into account the interference between an auto-ionized state with discrete energy levels and a continuum of states [**65**]. Since then, Fano resonances have been found to be universal phenomena that arise wherever there is the probability of interference between a resonant transmission path and a direct transmission path. Fano lineshapes have been observed in the spectroscopy of atoms and molecules,

in electron, neutron and Raman scattering, and more recently in quantum dots [**66**]. Figure 2.16 shows a schematic of the physics of the Fano resonance.

To briefly summarize, consider a system with a discrete energy state embedded in a continuum of states. The Hamiltonian of the discrete state without considering the continuum is

$$H_{discrete} = E_{\varphi}|\varphi\rangle\langle\varphi|, \tag{2.80a}$$

where φ is the discrete state. The Hamiltonian of the continuum states is

$$H_{continuum} = \sum_{E'} E'|\psi_{E'}\rangle\langle\psi_{E'}|, \tag{2.80b}$$

where $\psi_{E'}$ is the eigenstate in the continuum with energy E'. Now, for the whole system, the Hamiltonian is

$$H = E_{\varphi}|\varphi\rangle\langle\varphi| + \sum_{E'} E'|\psi_{E'}\rangle\langle\psi_{E'}| + \sum_{E'}(V_{E'}|\psi_{E'}\rangle\langle\varphi| + V^*_{E'}|\varphi\rangle\langle\psi_{E'}|), \tag{2.81}$$

where $V_{E'}$ is the coupling strength between the discrete state and the continuum. The eigenstates Ψ_E of the whole system can be expressed as a linear combination of φ and $\{\psi_{E'}\}$,

$$\Psi_E = a\varphi + \int dE' b_{E'}\psi_{E'}, \tag{2.82}$$

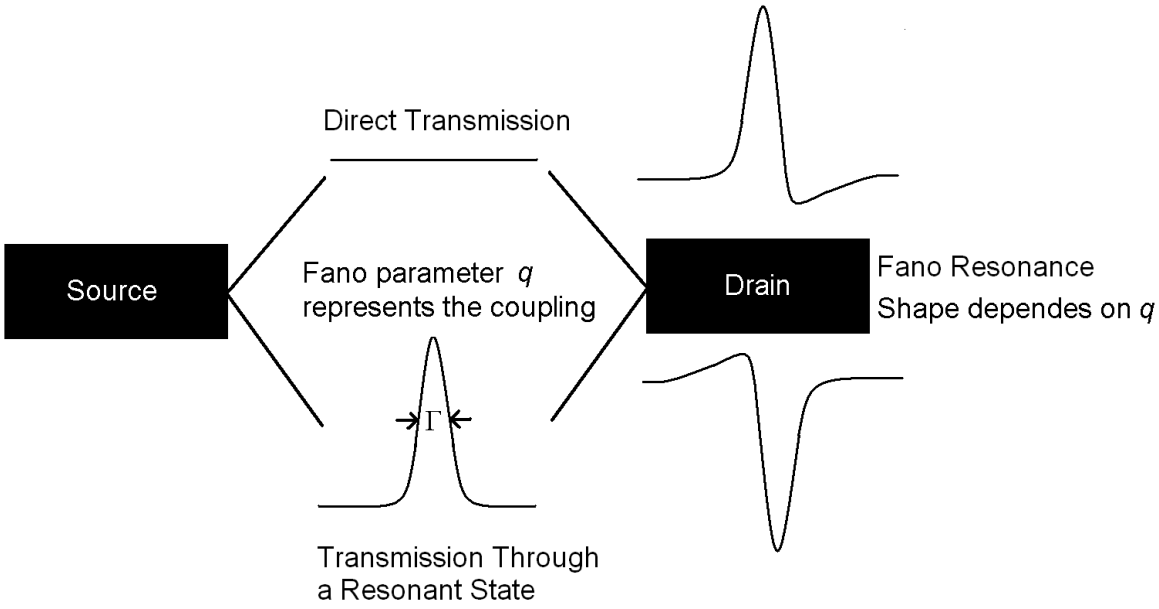

Figure 2.16. Schematic view of a Fano resonance. There are two paths for the transmission, one is resonant and one is direct. We note that these two paths do not need to be spatially separated.

where a and $b_{E'}$ are coefficients which depend on E. The explicit form of a and $b_{E'}$ will be given later.

According to perturbation theory [**67**], the state φ becomes

$$\Phi = \varphi + P \int dE' \frac{V_{E'} \psi_{E'}}{E - E'}, \tag{2.83}$$

where P denotes the principal part of the integral, and Φ is the state φ modified by an admixture of states of the continuum. The energy E of the resonant state is shifted by an amount F. $E = E_\varphi + F \equiv E_0$, where

$$F = P \int dE' \frac{|V_{E'}|^2}{E - E'}. \tag{2.84}$$

If $|V_{E'}|$ is a constant, $F = 0$. The phase shift Δ is

$$\Delta = -\arctan \frac{\pi |V_E|^2}{E - E_\varphi - F(E)}. \tag{2.85}$$

Fano calculated the result and he obtained [**65**]

$$a = \frac{\sin \Delta}{\pi V_E}, \tag{2.86a}$$

$$b = \frac{V_{E'}}{\pi V_E} \frac{\sin \Delta}{E - E'} - \cos \Delta \, \delta(E - E'). \tag{2.86b}$$

We define

$$\varepsilon = -\cot \Delta = \frac{E - E_\varphi - F(E)}{\pi |V_E|^2}. \tag{2.87}$$

For an incoming initial state i, it enters the system and eventually turns into a linear combination of the system eigenstates $\{\Psi_E\}$ through a perturbation T. The transition rate is then [**67**]

$$\omega_{\Psi\leftarrow i} = \frac{2\pi}{\hbar}|\langle\Psi_E|T|i\rangle|^2. \tag{2.88a}$$

Similarly the transition rate to the continuum without the discrete state is

$$\omega_{\psi\leftarrow i} = \frac{2\pi}{\hbar}|\langle\psi_E|T|i\rangle|^2. \tag{2.88b}$$

Fano calculated

$$\langle\Psi_E|T|i\rangle = \frac{1}{\pi V_E^*}\langle\Phi|T|i\rangle\sin\Delta - \langle\psi_E|T|i\rangle\cos\Delta. \tag{2.89}$$

As E passes through the resonance at $E = E_0$, Δ varies sharply, which causes a sharp variation in $\langle\Psi_E|T|i\rangle$. As $\sin\Delta$ is an odd function of $E - E_0$, and $\cos\Delta$ is an even function of $E - E_0$, the contribution from $\langle\Phi|T|i\rangle$ and $\langle\psi_E|T|i\rangle$ to $\langle\Psi_E|T|i\rangle$ have opposite phases on the two sides of the resonance.

The ratio of the transition rates is then [**65**]

$$\frac{T_{\Psi\leftarrow i}}{T_{\psi\leftarrow i}} = \frac{\omega_{\Psi\leftarrow i}}{\omega_{\psi\leftarrow i}} = \frac{|\langle\Psi_E|T|i\rangle|^2}{|\langle\psi_E|T|i\rangle|^2} = \frac{(\varepsilon+q)^2}{1+\varepsilon^2}, \tag{2.90}$$

where $\varepsilon = -\cot\Delta = 2(E - E_0)/\Gamma$, E_0 and $\Gamma = 2\pi|V_E|^2$ are the resonant energy and width, respectively. The Fano parameter q is

$$q = \frac{\langle\Phi|T|i\rangle}{\pi V_E^*\langle\psi_E|T|i\rangle}, \tag{2.91}$$

To understand the physical meaning of q, we can think of the initial state i transforming to $\{\Psi_E\}$ through two ways: one is through the continuum state $\{\psi_E\}$ and the other through the modified resonant state Φ. We note that

$$\frac{1}{2}\pi|q|^2 = \frac{|\langle\Phi|T|i\rangle|^2}{|\langle\psi_E|T|i\rangle|^2\Gamma} \tag{2.92}$$

is the ratio of the transition probability to the modified discrete state Φ and to a band width Γ of unperturbed continuum states $\{\psi_E\}$. q is a measure of the coupling strength between the resonant state and the continuum state. If $V_{E'}$ is real, there is no dissipation for the transition from one subsystem to the other. However, if $V_{E'}$ has an imaginary part, this means there is some dissipation in this system which is consistent with Clerk *et al.*'s analysis as we will show later.

Nöckel *et al.* [**68**] calculated the interference lineshape in a quantum wire. They considered an unbound state in one subband coexisting with a bound state in another subband. (For example, one open channel and one closed channel are coupled.) The transmission then exhibits the asymmetric Fano line shape. This is very interesting, especially for our CNT systems.

Clerk *et al.* [**69**] have developed another way to describe the Fano resonance that offers another perspective. They considered the Fano resonance as an interference of direct and resonant transmission by summing the transmission amplitude of direct and resonant transmission. Let the resonant path have the usual Breit-Wigner transmission amplitude $t_r(E - E_0) = z_r\Gamma/[2(E - E_0) + i\Gamma]$ and the direct path have the transmission amplitude $t_d = e^{i\phi}\sqrt{G_d}$, where ϕ is the phase difference between the direct and resonant path. The total conductance is given by the sum of the two

$$G(E) = |t_d + t_r(E - E_0)|^2 = G_d\frac{|\varepsilon + q|^2}{\varepsilon^2 + 1}, \tag{2.93}$$

where

$$\varepsilon = \frac{E - E_0}{\Gamma/2}, \tag{2.94a}$$

$$q = i + z_r\frac{e^{-i\phi}}{\sqrt{G_d}} = |q|e^{i\theta}. \tag{2.94b}$$

Here the Γ is the width of the resonant state and $|q|$ is related to the relative coupling strength and phase difference of the direct and resonant transmission. In this case, q is a complex number. $\Im q$ (the imaginary part of q) is related to dephasing and can be used to calculate the phase coherence time when $T \ll \Gamma$ [**69**],

$$\frac{\hbar}{\tau_\varphi} = \Gamma[|q|^2 + 1 - \sqrt{(|q|^2 + 1)^2 - 4(\Im q)^2}]. \tag{2.95}$$

This model is very clear about the origin of the direct transmission and the transmission through a resonant state. This is especially useful for Fano resonances in Aharonov-Bohm interferometers that we will discuss in the next section.

Figure 2.17 gives the simulation of the Fano profile for different q. We can see that $|q|$ (the modulus of q) determines the ratio of the resonant conductance to the direct conductance, whereas the phase of q affects the asymmetry. When $|q| = 0$, the line shape is a symmetric dip and in the opposite limit $|q| = \infty$, the line shape is a symmetric peak similar to the Breit-Wigner resonance discussed in the last section. The line shape is also symmetric for any value of q when the phase θ is $\pm\pi/2$. If $|q|$ is less (greater) than 1, the dominant feature will be a dip (peak).

At finite temperature and finite bias, the current is

$$I = \frac{2e}{h} \int d\mathcal{E}\, T^{Fano}(\mathcal{E})(f(\mathcal{E} - \frac{eV}{2}) - f(\mathcal{E} + \frac{eV}{2})), \tag{2.96}$$

where $f(\mathcal{E} - \mu) = \frac{1}{e^{(\mathcal{E}-\mu)/k_B T}+1}$ is the Fermi distribution function and $T^{Fano}(\mathcal{E}) = G_d \frac{|q+\varepsilon|^2}{1+\varepsilon^2}$ is the Fano transmission coefficient at zero temperature, with $\varepsilon = \frac{E-E_0}{\Gamma/2}$. In the linear response regime[6], the conductance for a Fano resonance is

$$G = \frac{2e^2}{h} \int d\mathcal{E}\, T^{Fano}(\mathcal{E})(-\frac{\partial f}{\partial \mathcal{E}}), \tag{2.97}$$

Numerical simulations of the temperature dependence of the Fano profile are shown in Figure 2.18. As T increases, the shape of Fano resonance remains almost the same although the

[6]In the linear response regime, $T^{Fano}(\mathcal{E})$ is independent of energy $\mathcal{E}$ at the range of $(-eV/2, eV/2)$.

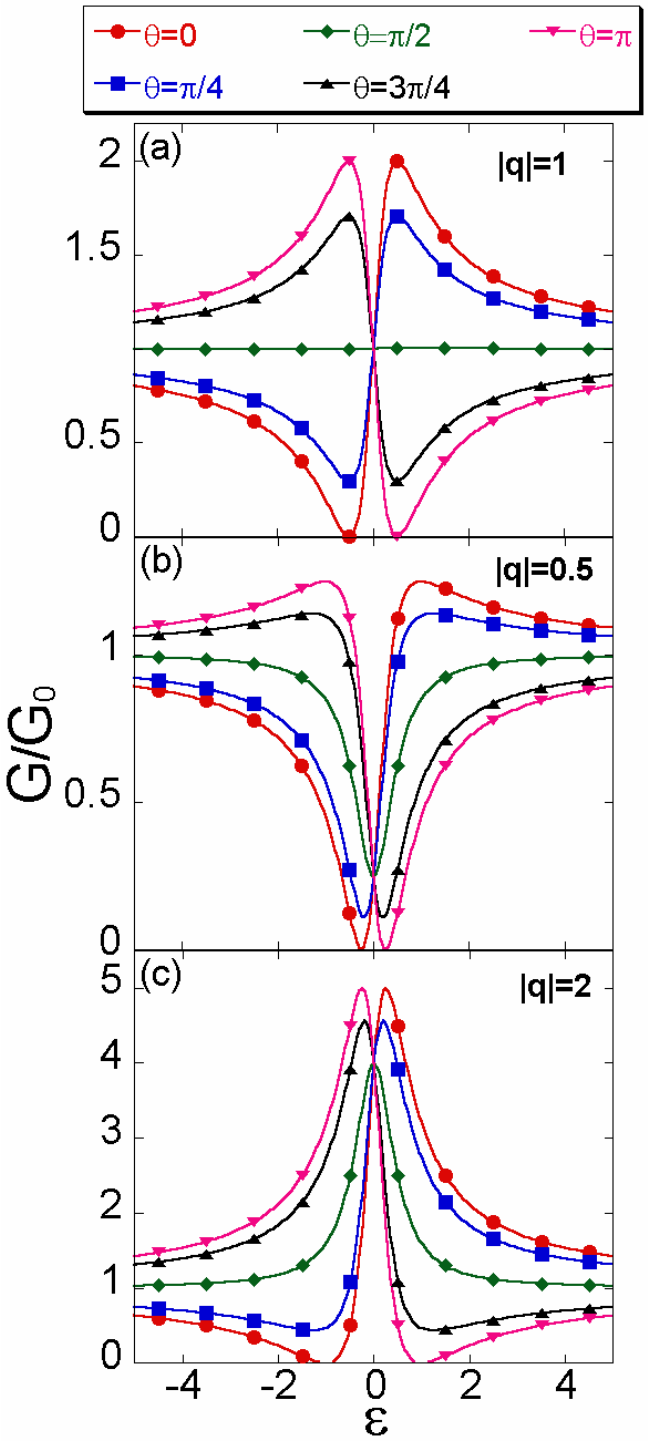

Figure 2.17. (Color) Simulations of Fano profile at zero temperature with different phase of q. G_0 is the conductance far away from resonance. (a) $|q|$=1, (b) $|q|$=0.5, (c) $|q|$=2.

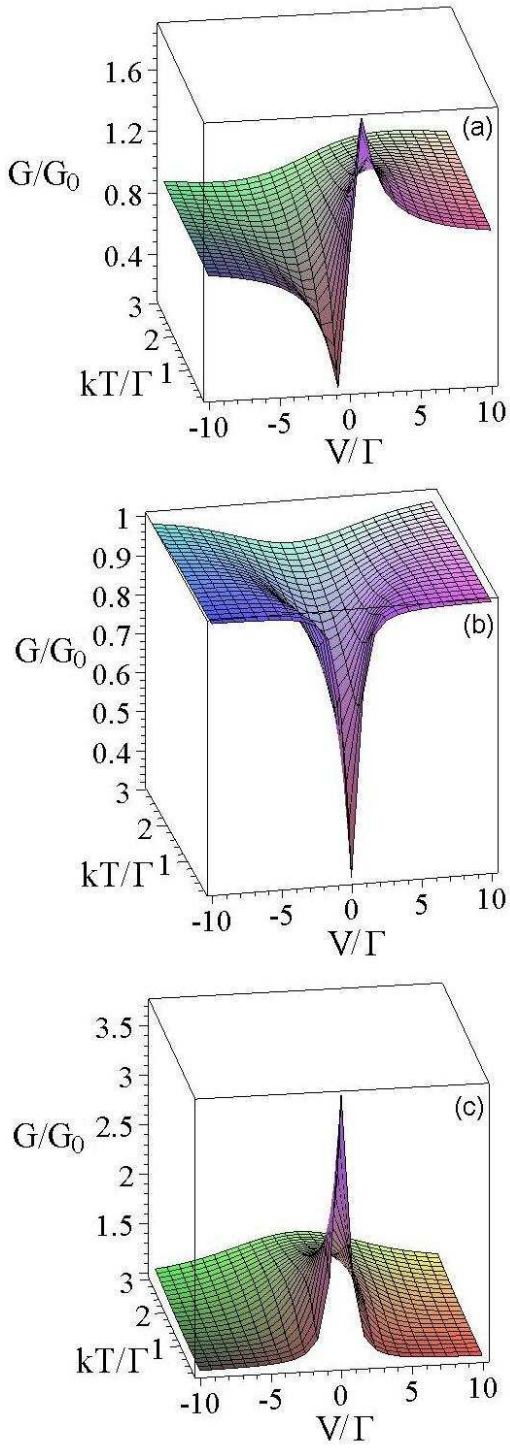

Figure 2.18. (Color) Numerical simulations of temperature evolution of Fano profile. G_0 is the conductance at far away from resonance. (a) $|q| = 1$ and the phase $\theta = 0$, (b) $|q| = 0.5$, $\theta = \pi/2$, (c) $|q| = 2$, $\theta = \pi/2$.

amplitude of the conductance peak or dip decreases and the half width increases. $\Gamma \sim 3.5\, k_B T$ is expected from Fermi broadening. At $T \gg \Gamma$, we can expect the Fano shape to be totally destroyed.

2.3. Transport Measurement of Carbon Nanotubes

There is a tremendous amount of interest in the transport properties of the CNTs for the reasons outlined in Chapter 1. Although a large amount of theoretical and experimental work has been done, some fundamental questions regarding CNT electronic transport remain unanswered and require clarification. In this section we will give a brief review of the experimental work.

2.3.1. Nanotube electronic structure

In Sec. 2.1, we demonstrated that the band structure of SWCNTs depends on their chirality. Wildöer *et al.* [**70**] and Odom *et al.* [**71**] first verified the predicted relation between the atomic structure of the SWCNTs and their electronic structure,. In both groups, they used a scanning tunneling microscope (STM) operating at low temperature to probe the DOS and the atomic structure of SWCNT. An image of atomically resolved SWCNT structure can be found in Fig. 2.1(a). Metallic and semiconducting SWCNTs were observed and their atomic structures are in good agreement with the theoretical predictions. However, small band gap semiconducting CNTs ($n - m = 3l$, $l \neq 0$) were not observed by either group. The small-band gap was later observed by Ouyang *et al.* [**72**] using similar techniques at 5 K. Small band gaps (0.080, 0.042, 0.029 eV) were observed in (9,0), (12,0) and (15,0)

SWCNTs, respectively. In the armchair SWCNT (8,8), a gap-like feature was observed in a bundle of SWCNTs but absent in an isolated SWCNT. This fits very well with the theoretical predictions described in Sec. 2.1.5. Transport measurements are also consistent with the theory. In this kind of measurement, the CNT is typically placed on a substrate, connected to electrodes. A gate is often used in this type of device. Tans *et al.* identified metallic [**73**] and semiconducting [**74**] SWCNTs, by measuring the CNT conductance as a function of gate voltage and Zhou *et al.* [**75**] reported observation of small-band gap SWCNTs using similar techniques. Experimentally, the conductance of a metallic SWCNT shows almost no dependence on the gate voltage, while the a semiconducting SWCNT shows large dependence. The small gap semiconducting SWCNT appears similar to a metallic SWCNT at room temperature. But a dip in conductance with varying gate voltage will show up at low temperatures.

For MWNTs, in the early experiments, the devices showed no dependence on gate voltage [**15**, **62**]. In 2001, Collins *et al.* [**76**] demonstrated each shell of a MWNT can be either metallic or semiconducting. They developed a method to remove single carbon shells from MWNTs. Figure 2.19 shows their technique of electrically breaking down individual shells of a MWNT and individual SWCNTs in a SWCNT rope. Figure 2.20(A) demonstrates that after each shell is burned, the behavior of the MWNT can be semiconducting or metallic depending on the outermost shell. After all the metallic shells are burned, a band gap can be observed as in Fig. 2.20(B). Their experiment demonstrates that a MWNT can have both metallic and semiconducting shells in the same device and the transport in MWNTs is mostly through the outermost shell.

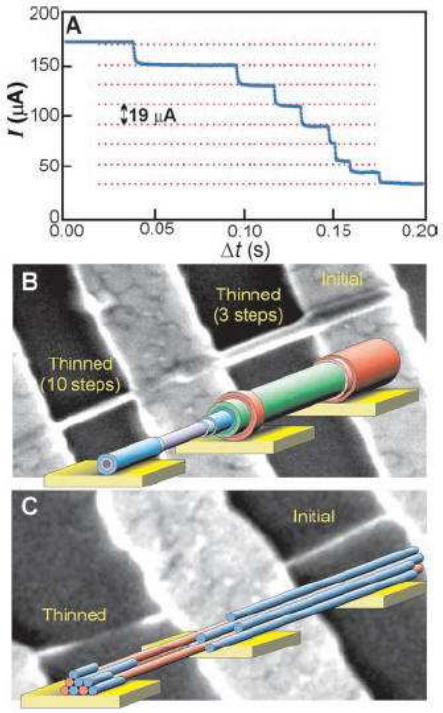

Figure 2.19. (Color) (A) The partial electrical breakdown of a MWNT. (B) Images of partially broken MWNTs show clear thinning. (C) Similar thinning in SWCNT ropes. Adapted from Ref. [**76**].

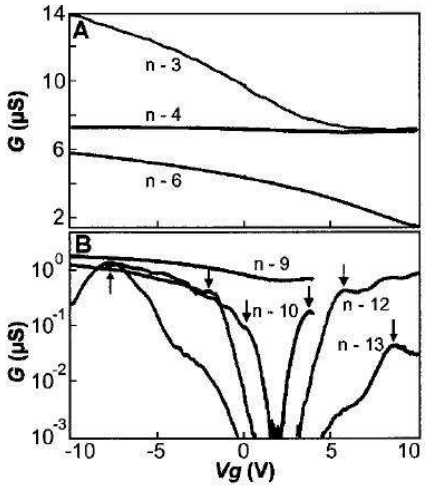

Figure 2.20. (A) The low-bias conductance $G(V_g)$ changes between semiconducting and metallic behaviors due to the nature of the outermost shell at each stage of breakdown. (B) When the last metallic shell (n-9) has been removed, a band gap can be seen. Adapted from Ref. [**76**].

2.3.2. Ballistic transport

A metallic SWCNT has two bands crossing the Fermi energy, the ideal conductance for ballistic transport is $4e^2/h$ from the Landauer formula, taking into account the spin degeneracy. However, in early experiments, it was hard to make good contact to the CNTs. In these devices, single electron tunneling effects were first observed [**73**,**77**]. These experiments demonstrated that metallic SWCNTs behave like a large quantum dot, which indicated the electron in the metallic SWCNT is delocalized. Further details about these experiments will be discussed in Sec. 2.3.4. The first experimental evidence of ballistic transport in a CNT was done in MWNTs. Frank *et al.* [**47**] attached a MWNT to the end of a conducting atomic force microscope (AFM) tip. By dipping the other end of the MWNT in mercury, they were able to measure the conductance of the MWNT as a function of the CNT length. They found the conductance is independent of the length and quantized at $2e^2/h$. They further carried out experiments by putting current in the MWNTs and found MWNTs can sustain a huge current. By their estimation, if the resistance was from the inside of the MWNTs, the MWNTs would have been burned out due to heating by the large current. They concluded that MWNTs are ballistic conductors even at room temperature. However, the value of $2e^2/h$ is only half of what is predicted by theory. This experiment remains controversial until today as other experiments done with MWNTs suggested diffusive transport behavior [**15**,**62**,**78**,**79**]. Urbina *et al.* [**80**] carried out a similar experiment by dipping the MWNTs into Aroclor 1254[7]. They found the conductance was independent of length and the quantization was $4e^2/h$ as the theory predicted. As will be discussed in Sec. 2.3.3,

[7]A mixture of polychlorinated biphenyls.

other experiments showed diffusive behavior in MWNTs [**15**,**62**,**78**,**79**,**81**]. The discrepancy remains unsolved although it might be related to the fact in the experiments showing ballistic behavior, MWNTs were suspended while the experiments showing diffusive behavior, MWNTs lay on substrates. One possible explanation is that the MWNTs on the substrates are electrically doped by the substrate.

Ballistic transport in SWCNTs has also been reported in both metallic [**82**] and semiconducting SWCNTs [**18**]. The criterion of the ballistic transport used by the authors in both papers was that the conductance can approach the theoretically predicted value of $4e^2/h$ when tuned by a gate. However, we should be cautious about this claim as the length dependent resistance measurement, which would be overwhelming evidence of ballistic transport, was not possible in this type of experimental setup. Better evidence of ballistic transport in metallic SWCNTs was shown by Bachtold *et al.* [**81**]. In their experiment, CNT devices were scanned by an electrostatic force microscopy and scanned gate microscopy. The authors scanned the voltage profiles of the CNTs while biasing the CNTs. As there was no measurable voltage drop in the metallic SWCNTs, metallic SWCNTs were determined to be ballistic conductors. MWNTs and semiconducting SWCNTs were also studied and the authors concluded that MWNTs are diffusive conductors while semiconducting SWCNTs have a series of large barriers to conduction along their length. This result with SWCNTs is consistent with their earlier work [**83**] that claims that the metallic SWCNTs are ballistic conductors as the backscattering of electrons by long range disorder is suppressed. In doped semiconducting SWCNTs, backscattering is allowed. For MWNTs, as discussed earlier, there is still controversy about whether the transport is ballistic or diffusive. The result of this

experiment adds weight to the view that MWNTs are diffusive conductors, but the debate far from over. A very recent experiment even claims observation of multichannel ballistic transport in MWNTs [**84**].

2.3.3. Diffusive transport

Diffusive transport behavior in MWNTs was discovered in the first attempt of measuring MWNT devices by Langer *et al.* [**78**]. A MWNT 800 nm long with a diameter of 20 nm was measured down to 20 mK. A logarithmic temperature dependence of conductance was observed at high temperature. At low temperature the conductance saturated. This was explained as arising from two-dimensional WL. At low temperatures, a magnetic field was applied perpendicular to the MWNT tube axis. The conductance increased with aperiodic fluctuations as shown in Fig. 2.21(a). The temperature dependence of the amplitude of the fluctuation is shown in Fig. 2.21. The data from Langer *et al.*'s experiment support the presence of WL and UCF in MWNTs. The idea of MWNTs being diffusive conductors was further strengthened by a series of experiments [**15**,**62**,**79**,**81**]. In Ref. [**79**], a magnetic field was applied along the tube axis. If MWNTs were ballistic, the nanotube resistance would oscillate with the enclosed magnetic flux with a period of h/e due to the Aharonov-Bohm effect [**85**]. On the other hand, if transport is diffusive, the oscillation period would be $h/2e$ [**86**]. As the conductance oscillates with a period of $h/2e$, the authors concluded that transport in MWNTs was diffusive with an estimated phase coherence length $l_\varphi \approx 54$ nm at 1.8 Kelvin. Another implication of this experiment is that the conduction of MWNTs

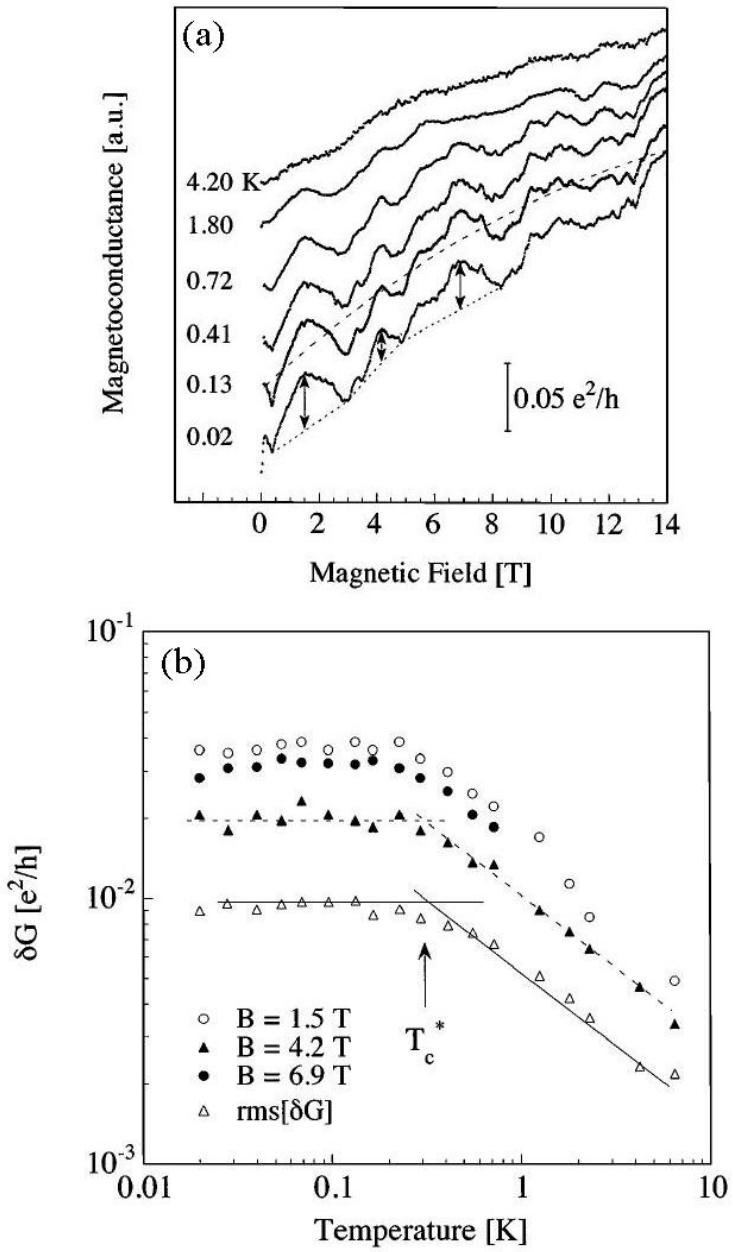

Figure 2.21. (a) Magnetic field dependence of the magnetoconductance at different temperatures. (b) Temperature dependence of the amplitude of δG for three select peaks in (a) as well as rms[δG]. Adapted from Ref. [**78**]

is through the outermost shell. This assumption was supported by Ref. [**76**] as discussed before.

The phase coherence length l_φ was measured by Stojetz *et al.* [**87**] using a sweeping gate voltage to get an ensemble averaged magnetoresistance. This ensemble average would decrease the contribution from UCF, but would not affect WL. Their results are shown in Fig. 2.22.

More recently, Stojetz *et al.* [**88**] measured the the conductance of a MWNT as a function of gate voltage and perpendicular magnetic field. They found the phase coherence length l_φ was dependent on the gate voltage U. The averaged phase coherence length was about 120 nm at 1K with a power law dependence with temperature. The exponent -0.31 was close to the theoretical predictions as in Eqn. 2.63a.

In closing, only a few experiments have studied the phase coherence length. MWNT have been cooled below 300 mK only in Ref. [**78**]. This study yielded a very short phase coherence length, which is inconsistent with other studies [**62**, **79**, **88**].

2.3.4. Nanotube quantum dot

Bockrath *et al.* [**77**] measured SWCNT bundles and Tans *et al.* [**73**] measured individual SWCNTs. In their experiments, the SWCNTs or SWCNT bundles were poorly connected to the electrodes resulting in high contact resistance between the SWCNTs and the electrodes. In this case, the transport was dominated by Coulomb blockade. The CNT device conductance measured in both experiments was on the order of 0.01$\sim$0.1 e^2/h, where e^2/h=25.898 kΩ is the conductance quantum. Coulomb blockade effects were found in these

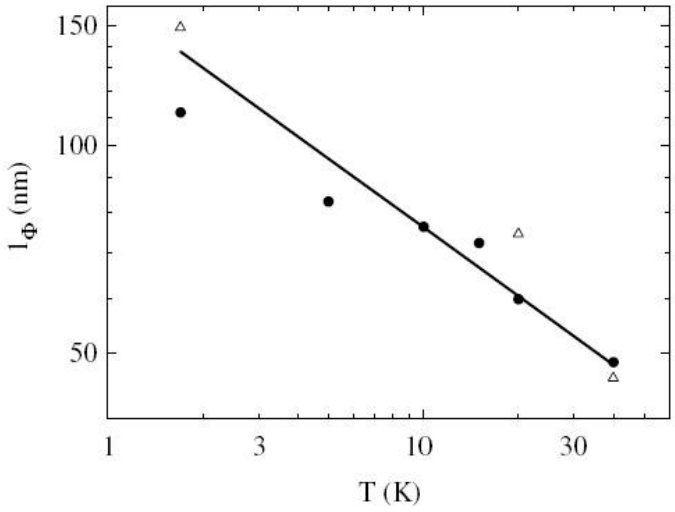

Figure 2.22. Temperature dependence of phase coherence length of a MWNT derived from WL (hollow triangle) and UCF (solid circle). The solid line is a fit to $T^{-1/3}$. Adapted from Ref. [**87**].

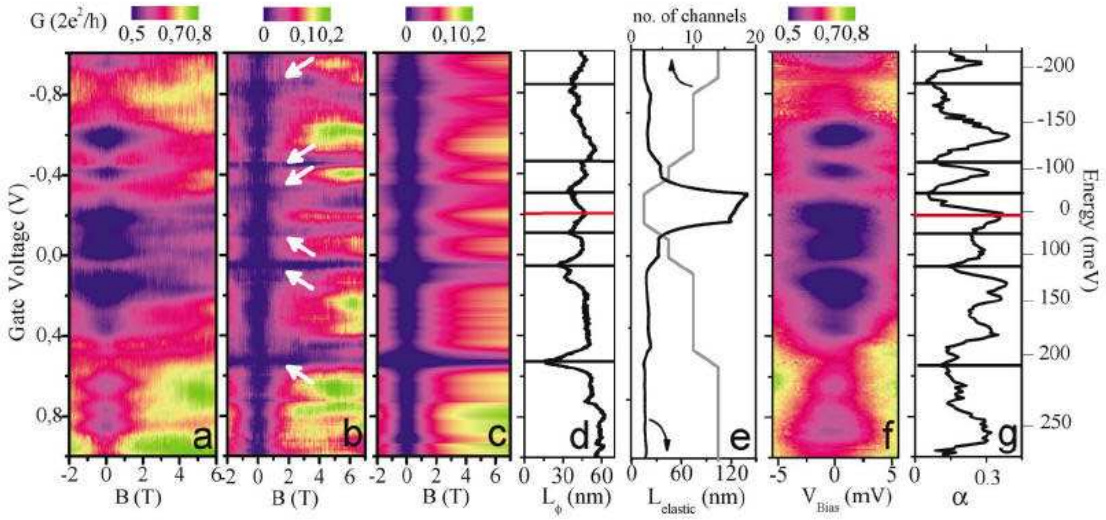

Figure 2.23. (Color) (a) Conductance G as a function of gate voltage U and perpendicular magnetic field B at a temperature 10 K. (b) The deviation of G from the zero-field conductance $G(U,B) - G(U,0)$. (c) Reproduction of the magnetoconductance by 1D WL. (d) Phase coherence length l_φ vs gate voltage as obtained from the fit. (e) Elastic mean free path and number of transport channel per spin direction. (f) Differential conductance as a function of U and dc bias voltage V at T=10 K. (g) Exponent α vs U from power law V^α to $G(U,V)$ in the range $eV \gg k_B T$. Adapted from Ref. [**88**].

systems, manifesting themselves as periodic oscillations with applied gate voltage. For doped semiconduting SWCNTs with high contact resistances, Coulomb blockade manifested itself as an irregular oscillation because the impurities or defects effectively cut the SWCNT into multiple sections. Each section with different length, had a different period with respect to gate voltage [**83**].

For SWCNTs with intermediate contact resistances with a conductance on the order of e^2/h, Kondo physics was discovered [**89**]. In this regime, charging effects still play a central role. But high order processes known as co-tunneling can be present. As there is more than one electron in the CNT quantum dot and the electron has spin, spin shell filling was observed as a result of the Pauli exclusion principle [**90**]. Fabry-Perot interference was found in SWCNTs with a conductance approaching $3\sim4\ e^2/h$ [**91**]. In this limit, the transparency is high and the electron can be reflected from the two CNT-electrode contacts. The interference effect can be tuned by a gate. The Fabry-Perot effect in SWCNTs was regarded as a proof of ballistic transport in SWCNTs. This is because to observe Fabry-Perot interference, the electron must coherently travel many times through the device, being reflected only at the contacts, so the mean free length must be very long.

In all these measurements, the SWCNTs were clean. In MWNTs, clean quantum dot behavior was not observed until 2002. Buitelaar *et al.* [**92**] observed Coulomb blockade behavior in some of the MWNT devices. Two devices were presented in the paper. The first device constituted an open system which showed conductance variations as a function of gate and bias voltage. The variations were explained as a quantum interference effect and differed from Coulomb blockade patterns since they lacked periodicity. In the second

device, Coulomb blockade patterns were observed as well as the Kondo effect. The difference between the two devices was explained in the following way: the first MWNT device is a diffusive conductor and the conduction is through the outermost shell. In the second device, however, the conduction is through more than one shell. The outer shell is semiconducting and the inner shell is metallic. While the outer shell has a lot of disorder, the inner shell is clean and constitutes a large quantum dot. This argument is very interesting; however, no further evidence supports their model.

2.3.5. Zero bias anomaly

Ohm's law states the resistance (or conductance) of a conductor is independent of the bias applied. The term "zero bias anomaly" is used for conductors with resistance (or conductance) that deviates from Ohm's law at zero bias. In both SWCNTs [**57**] and MWNTs [**93**], a suppression of conductance near zero applied bias has been observed. This zero bias anomaly observed in both experiments shows a power law dependence on temperature T and bias voltage V. The power law behavior of SWCNT experiments was explained as arising from Luttinger liquid behavior. This explanation has yet to be verified or challenged. In MWNTs, as the diameters are large and diffusive behavior was observed in similar devices, unconventional Coulomb blockade theory [**64**] is favored [**94**]. Both theories yield a similar power law dependence as described in Sec. 2.2.6. Further work is needed to clarify this intriguing behavior.

2.3.6. Fano resonances in quantum dots

Fano resonances have been observed in quantum dots formed from two dimensional electron gases [**66**, **95**–**98**]. In Refs. [**66**, **95**], the quantum dot is defined by top gates and there is no spatial difference between the direct and resonant transmission. Although these experiments were the first observation of Fano resonances in a mesoscopic system, the nature of the direct and resonant transmission paths was not clear. Kobayashi *et al.* [**96**–**98**] used an Aharonov-Bohm interferometer with a quantum dot embedded in one arm. With this configuration, the direct path and the path through a resonant state is clear. This configuration has the additional advantage that the phase difference between the two paths can be easily tuned by applying a magnetic field. As discussed in Sec. 2.2.7, Clerk *et al.* [**69**] derived the expression for the phase coherence time by looking at the real and imaginary part of q. However, the decoherence caused by finite temperature was not considered. As in the Aharonov-Bohm system, the phase of q can be tuned. The dephasing effect due to temperature can be separated from intrinsic dephasing.

2.3.7. Summary

As discussed, the transport physics of CNTs, although intensively studied, has still left many unsolved questions. The physics is rich and rewarding. The temperature regime studied ranged from room temperature to a hundred milliKelvin, with most experiments being done above a few Kelvin and very few experiments being done in the millikelvin temperature

regime. The measurement of phase coherence length below 300 mK is insufficient. There is still plenty of work left to be done which motivates this research.

CHAPTER III

Experimental Techniques

The techniques of sample fabrication and measurement will be discussed in detail in this chapter. The techniques described here are most frequently used. As the techniques are constantly improving and equipment conditions keep changing, different techniques, approaches and/or recipes were used in the experiments even for the same tasks at different time period of the experiments.

3.1. Sample Fabrication Techniques

Our sample fabrication process for mesoscopic devices consists of wafer preparation, lithographic patterning process, pattern transfer process such as thin film deposition or etching depending on the application. Figure 3.1 shows the general process flow for our fabrication. We start with wafer preparation, the next step is resist coating (photoresist or e-beam resist), followed by lithographic patterning. The patterning can be done either by photolithography or e-beam lithography. Depending on application, the next step can be thin film deposition or etching. (Etching is not used in this work, but we still show it in the flow chart for completeness of sample fabrication processes.) After thin film deposition and the lift-off process, (or etching process as shown in the process flow chart,) the whole process is repeated if multi-layer processing is required.

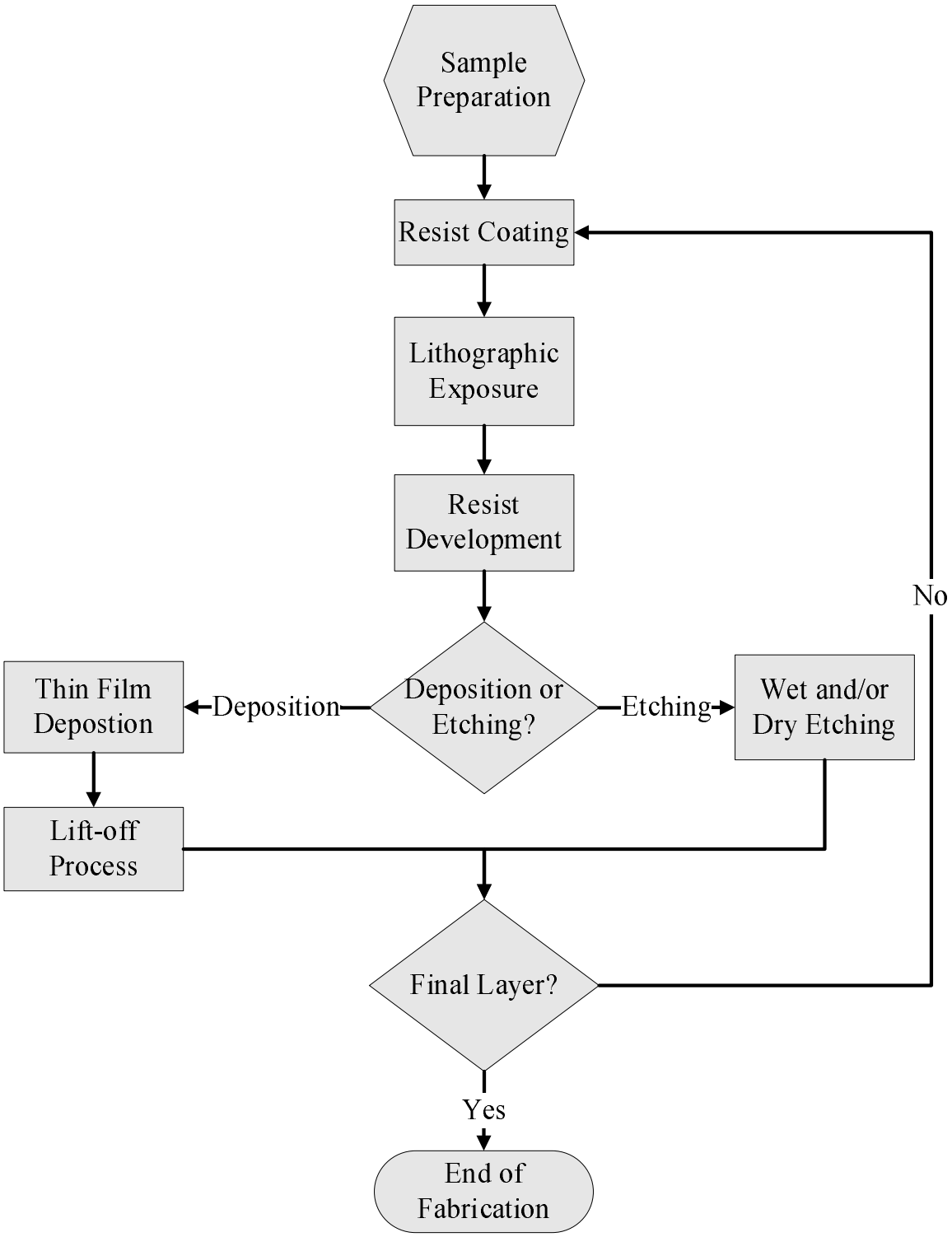

Figure 3.1. Process flow of sample fabrication.

3.1.1. Wafer selection and preparation

We started with commercial silicon wafers. Different wafers were used in different time periods. In the early experiments, the wafers were polished on one side with 300 nm thermal oxide layer for insulation[1]. These silicon wafers were not doped. At low temperature, the substrates are essentially insulating. For backside gated experiments, highly doped (p^{++}) silicon wafers polished on one side with 350 nm thermal oxide layer were purchased[2]. In those wafers, the silicon remained conductive even at low temperatures and was used as a backside gate. As the wafers were $3 \sim 4''$ in diameter while the size of the samples we could process at one time was no more than $1'' \times 1''$[3], the whole wafers were diced by a diamond scriber before use. After the wafers were diced to the desired size, they were cleaned with the following procedure:

(1) Ultrasonication for 3 minutes in an acetone bath.

(2) Ultrasonication for 3 minutes in an isopropyl alcohol bath.

(3) Ultrasonication for 3 minutes in an 18 MΩ Deionized (DI) water bath.

(4) Ultrasonication for 3 minutes in an isopropyl alcohol bath.

(5) Blow dry with dry N_2 immediately after the wafers were taken out from the last isopropyl alcohol bath.

The cleaning process should clean off any dust generated by dicing, and remove any organic and inorganic contamination. At the end of the process, the isopropanol should come off the

[1]Purchased from Polishing Corporation of America, Santa Clara, CA.
[2]Purchased from Si-Tech Inc., Topsfield, MA.
[3]This limit is given by the size of our photomask.

wafer surface uniformly. If it forms droplets on some spots, this means that the wafer is not clean enough and the process should be repeated.

3.1.2. Photolithography

Photolithography was used for large area patterning and e-beam lithography was used to pattern the small structures. This is because our device feature size is below 100 nm. The photolithography system we used has a resolution limit of $1 \sim 2\ \mu m$ depending on the exact system used. Electron beam lithography is needed for the small feature size needed for our devices. Besides the resolution requirement, the design of the pattern changes from sample to sample. E-beam lithography gives us the flexibility to pattern different samples by simply generating a new computer pattern. However, although e-beam lithography has the advantage of high resolution and flexibility, the writing speed is slow. For large area patterning, it is often too time consuming.

For our samples, although the active area of the devices we fabricated is only a few tens of square micrometers, in order to connect them to the electronic measuring apparatus, large wirebonding pads of size at least $100 \times 100\ \mu m^2$ are needed. The strategy we use is to pattern the large contact pads by photolithography, then pattern the fine structure by e-beam lithography.

At different time periods, different recipes were used for photolithography. At the beginning, we used a single layer photoresist (Shipley 1813[4]) and a Quintel Q-2000 mask aligner[5] to expose the substrate. As this method only used a single layer of resist, after lift-off, the

[4]Purchased from MicroChem Inc., Newton, MA.
[5]From Quintel Corp. Morgan Hill, MA.

edge of the deposited metal became warped, creating a sidewall as shown in Fig. 3.2. The consequence of this detrimental effect was that the subsequent layer of metal might lose electrical contact with the first layer although visual inspection with a scanning electron microscope (SEM) would look fine. To avoid this problem, bilayer resist was used. The idea is to create an undercut, so the lift-off will be clean without warp at the edges. See Fig. 3.3 for an illustration of the process. Two techniques were developed and both give good results with clean lift-off.

The steps in the first technique are listed below:

(1) Spin lift-off resist LOR 7B[4] at 3000 rpm for 60 seconds for a 750 nm thick coating.

(2) Bake the substrate in a convection oven at 170 °C for 30 minutes.

(3) Spin Shipley 1813 photoresist at 4000 rpm for 60 seconds for a 1.5 μm thick coating.

(4) Bake the substrate in a convection oven at 110 °C for 30 minutes.

(5) Put the substrate in a homemade contact exposure apparatus[6] and expose the substrate under a 100 W spotlight halogen lamp for 7 minutes 30 seconds, using a Cr on quartz photomask[7].

(6) Mount the substrate on spinner and spin at 500 rpm. Develop the pattern by spraying MF-319 developer[4] on the substrate for 1 minute, followed by spraying DI water for 1 minute. The substrate is then spun dry at 5000 rpm for 1 minute.

[6]The schematic of the home-made exposure device can be found in Ref. [**99**].
[7]Ordered from Photronics Corp., Milpitas, CA.

A large undercut (1 μm) was present for this process. This undercut can be seen in an optical microscope.

In the early experiments, an alternative technique was also used as described below:

(1) Spin Methylmethacrylate/methacrylic acid (MMA/MAA)(8.5)[4] at 3000 rpm for 60 seconds for a 160 nm thick coating.

(2) Bake the substrate in a convection oven at 110 °C for 30 minutes.

(3) Spin Polymethylmethacrylate (PMMA) 950K (4% in anisole)[4] at 4000 rpm for 60 seconds for a 200 nm thick coating.

(4) Bake the substrate in a convection oven at 110 °C for 30 minutes.

(5) Expose the substrate in a Quintel 4000 mask aligner in deep ultraviolet (DUV) mode for 999 seconds (maximum allowed by the mask aligner). The wavelength of the ultravilet light is 220 nm.

(6) Develop the pattern by spinning the substrate at 500 rpm while spraying MIBK:IPA 2:3 on the substrate for 3 minutes, followed by spraying isopropyl alcohol for 3 minutes. The substrate is then spun dry at 5000 rpm for 1 minute.

The undercut is not visible although believed to be present because MMA/MAA resist is more sensitive to exposure than PMMA resist. Figure 3.4 shows the spin curve for the MMA/MAA copolymer and PMMA.

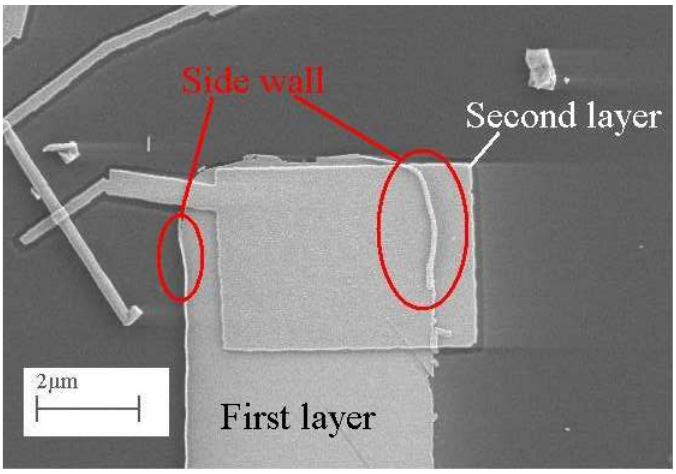

Figure 3.2. (Color) SEM image of a device with bad lift-off. The first layer was patterned by photolithography and the second layer was patterned by e-beam lithography. The red solid line circles the sidewall due to bad lift-off of the first layer.

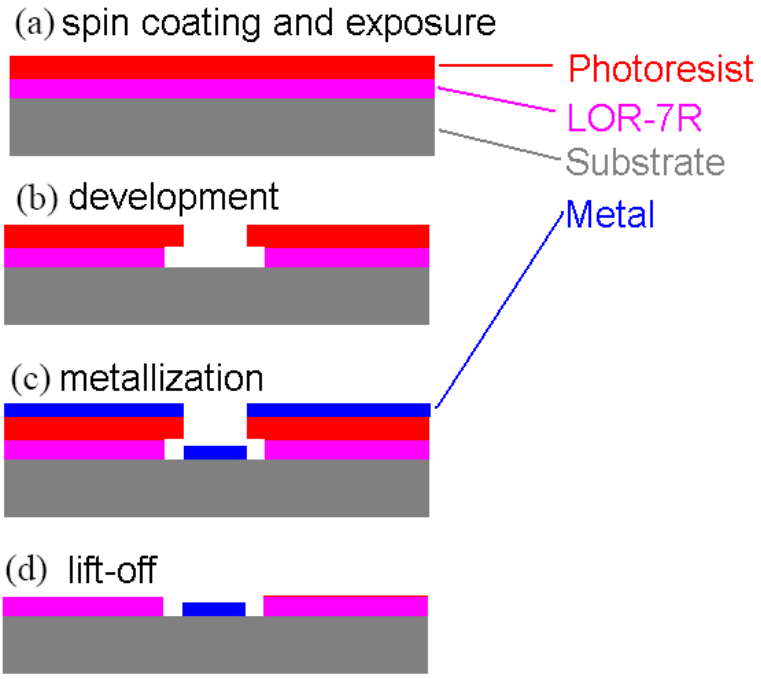

Figure 3.3. (Color) Steps in the photolithographic process. (a) Spin coat two layers of resist and expose, (b) Development opens windows on the substrate, the bottom layer is more sensitive to exposure resulting in an undercut, (c) Evaporate metals, (d) Lift off the resist, leaving only metal on the substrate.

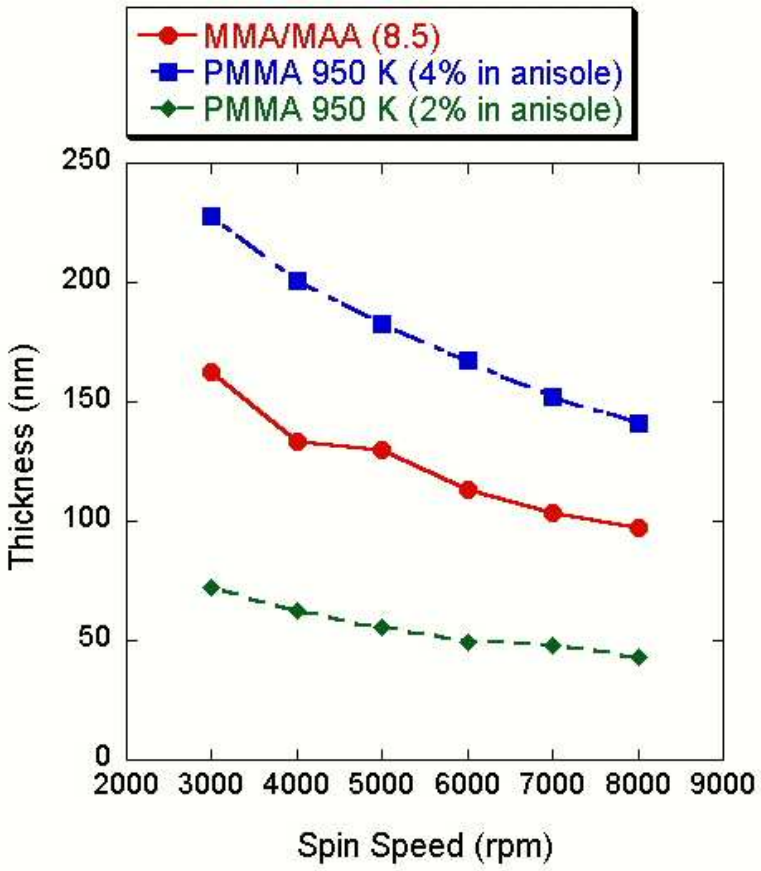

Figure 3.4. (Color) The spin curves of MMA/MAA (8.5), PMMA 950 K 4% in anisole and 2% in anisole.

3.1.3. Electron beam lithography

The e-beam lithography is done in an e-beam writer converted from a JEOL JSM-840 SEM. The software *ElectronScribe* for e-beam writing was developed by Prof. Venkat Chandrasekhar. The program controls a National Instrument card NI-6052E card[8] for communicating with the JEOL JSM-840[9] through a home-made electronics box. The analog output DAC0OUT (DAC1OUT) of the NI-6052E is connected to the X (Y) scan coil input of the SEM through a buffer amplifier. The single-bit digital output DIO0 (DIO1) is connected to the external control enable (beam blanker signal). The analog input ACH0 is connected to the image signal. Figure 3.5 shows the circuit diagram of the electronics box constructed by the author[10]. The external control enable signal enables (0 V) and disables (5 V) the computer control of the X Y scan coil. The beam blanker signal enables (5 V) and disables (0 V) the beam blanking. The beam blanking is done by an electromagnetic coil to deflect the electron beam. If the voltage is too small (in terms of absolute value), the beam blanker will not be able to effectively deflect the beam while too big a voltage will slow down the beam blanking time. We tune the resistor shown in Fig. 3.5(d) to set the voltage just high enough to trigger the blanking. At present the voltage is -0.6 V and the blanker works well at frequency up to 100 kHz at the lowest probe current. At higher probe current the response time of the beam blanker is longer. The following outlines the steps for e-beam lithography.

(1) Spin MMA/MAA (8.5) at 3000 rpm for 60 seconds for a 160 nm thick coating.

(2) Bake the substrate in a convection oven at 140 °C for 30 minutes.

[8]From National Instrument, Austin, TX.
[9]JEOL-USA, Peabody, MA.
[10]This box replaces the old circuit box in Ref. [**100**].

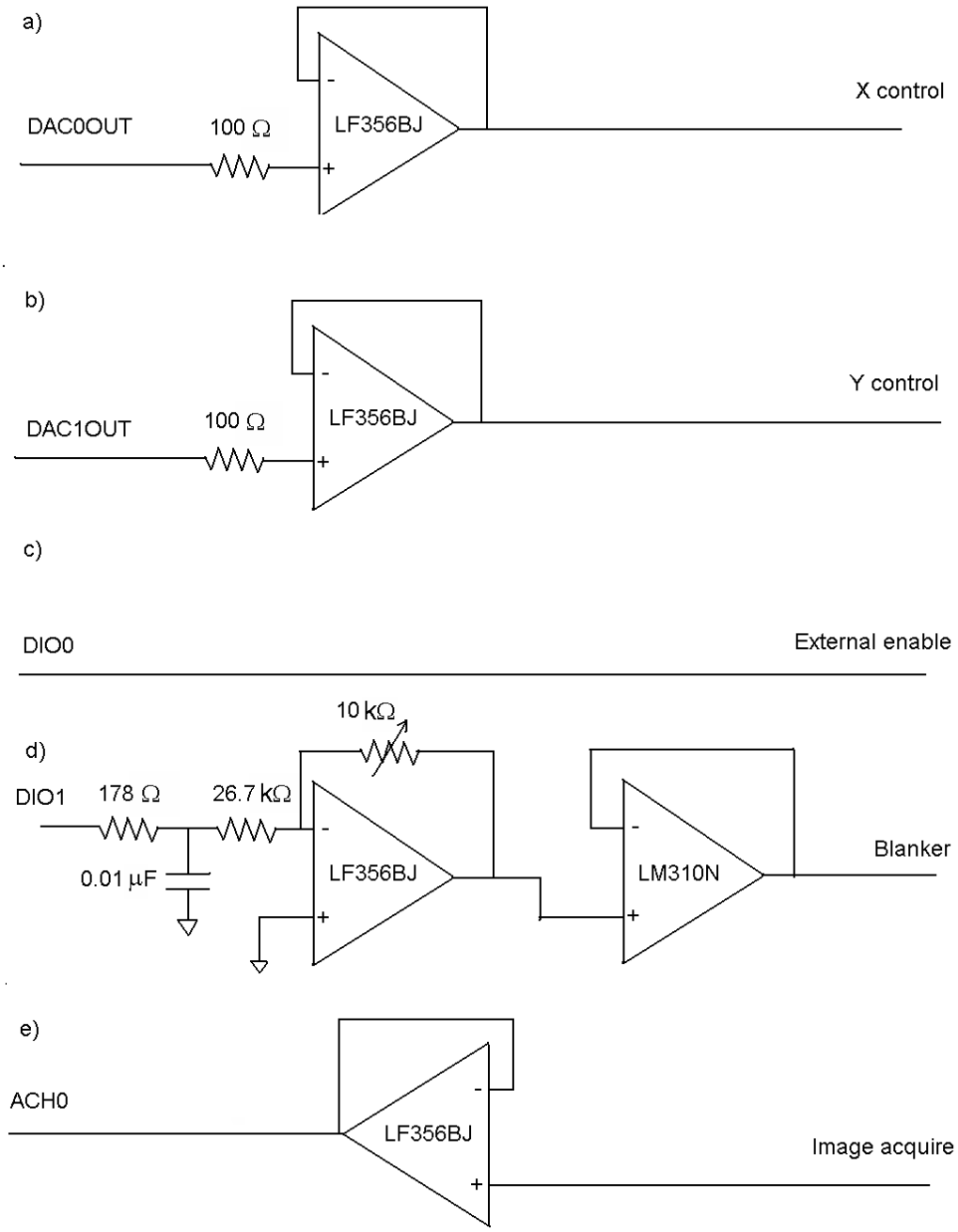

Figure 3.5. The circuit diagrams of the SEM control electronics connecting the NI-6052E card and JEOL 840 SEM. (a) DAC0OUT (card)-X scan coil (SEM), (b) DAC1OUT (card)-Y scan coil (SEM), (c) DIO0 (card)-External control enable (SEM), (d) DIO1 (card)-Beam blanker signal (SEM), (e) ACH0 (card)-Image signal (SEM).

(3) Spin PMMA 950K (4% in anisole) at 6000 rpm for 60 seconds for a 170 nm thick coating.

(4) Bake the substrate in a convection oven at 170 °C for 30 minutes.

(5) Expose the substrate in the JEOL JSM-840 SEM converted e-beam writer at 30 KV. The dosage is from 300 μC/cm^2 up to 650 μC/cm^2 depending on the size and geometry of the pattern. The most frequently used value is 400 μC/cm^2.

(6) Develop in MIBK:IPA (1:3) for 60 seconds and rinse in isopropyl alcohol for 60 seconds. Spin dry at 5000 rpm for 1 minute.

3.1.4. Plasma etch

For many of the samples, a plasma etch is used for various reasons. After photolithography (e-beam lithography), the exposed photoresist (or PMMA) is removed except for a very thin layer of residue. This will pose a problem for metallization and lift-off. A short-time O_2 or Ar^+ plasma etch is used to completely remove the photoresist (or PMMA) residue while minimizing the unwanted etch on the unexposed photoresist (or PMMA). There are four etchers built and used in this group. Two etchers are inside two evaporators for *in situ* etching while the other two etchers are external. All the etchers are essentially made of two parallel planar metal electrodes. The sample is attached to one electrode, after the system is pumped down, O_2 or Ar gas is introduced into the chamber and maintained at a constant pressure. A DC, AC, or RF power supply applies high voltage on one of the electrodes while the other electrode is kept grounded to generate a plasma. The power supply is turned off to stop the plasma after a certain time has elapsed. We note that depending on the power

supply used and the geometry of the etcher, the samples need to be attached to either the high voltage electrode or the counter electrode to optimize the etching process. The *in situ* etchers will be described in Sec. 3.1.5. We only describe the working condition for the two external etchers here.

The small external etcher can hold a sample of size up to 1 cm $\times$ 1 cm. The etcher is pumped by a sorption pump which needs liquid nitrogen for pumping. Prior to use, the pump is baked for a few hours for faster and better pumping. Sorption pumps are oil free and thus can avoid the contamination of the sample by oil. After the chamber is pumped down, 100 mTorr O_2 is introduced in the chamber without closing the pumping valve. As equilibrium is established, a plasma is started by a dc power supply[11] to apply -700 V to the electrode 2 cm above the sample. The etch rate of PMMA under such conditions is $\sim$1.5 nm/second. This is measured by using an AFM[12] before and after a 30 second etch. The height difference is 45 nm. For general sample etching, a 30-second etch is used.

The reactive ion etcher (RIE) built by the author can hold samples up to $3''$ in diameter. The etcher is pumped by a rotary pump. After pump down, O_2 is introduced through a needle valve in the chamber without stopping pumping. After the pressure stabilizes at 100 mTorr, a 100 kHz ac voltage[13] with a power of $\sim$0.11 W is applied to the electrode where the sample mounted. The counter electrode is $1''$ above the sample. The etch rate for PMMA for O_2 plasma etching in this etcher is $\sim$50 nm/second. Figures 3.6 and 3.7 show photos of this RIE.

[11]SRS PS325 high voltage power supply from Stanford Research Systems, Sunnyvale, CA.
[12]Purchased from Thermomicroscopes Inc.. Thermomicroscopes Inc. was acquired by Veeco Instruments Inc. Woodbury, MA, in 2001.
[13]PE-1000 from Plasma-Therm, Inc., St. Petersburg, FL.

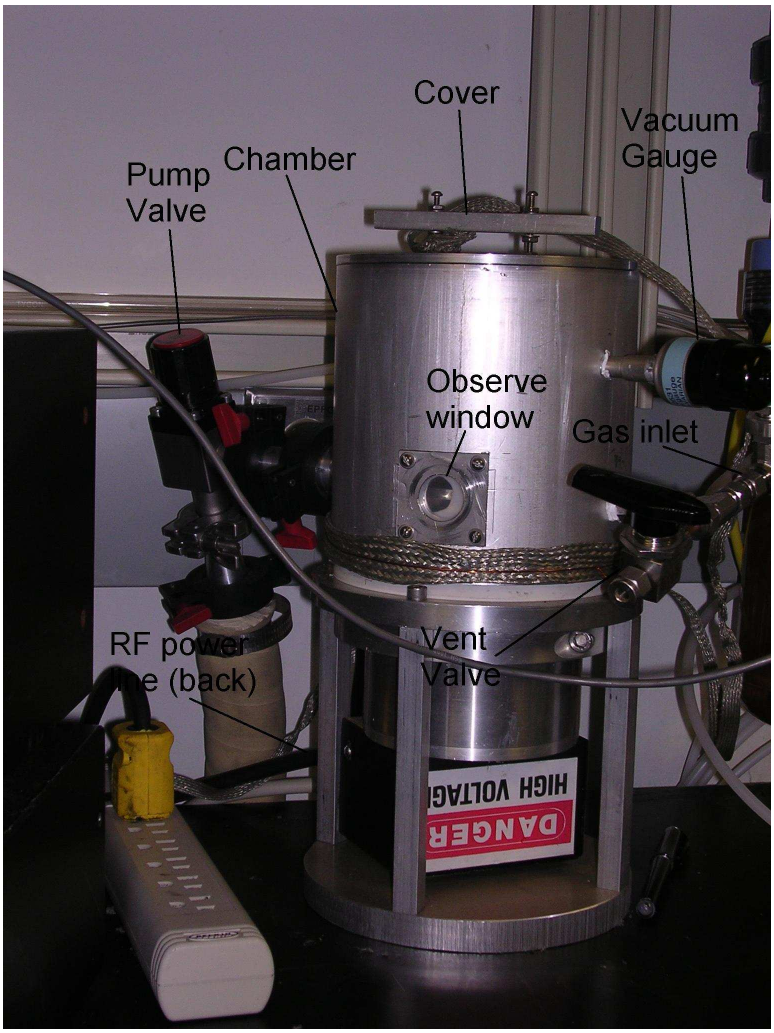

Figure 3.6. (Color) RIE system designed and constructed by the author. (The cooling water lines behind the etcher that are not shown here can be seen in Fig. 3.7.)

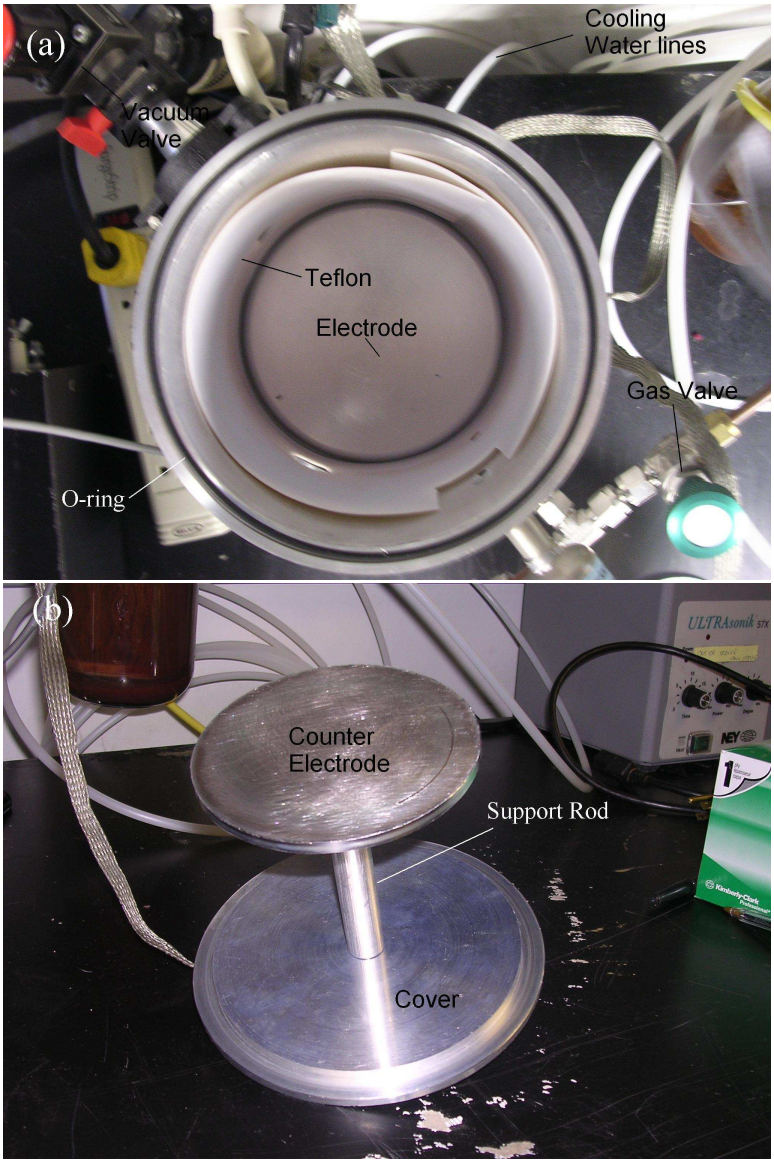

Figure 3.7. (Color) Inside view of the RIE. (a) Inside view from the top. Teflon sheet is used as insulation to prevent unwanted arcing. (b) The top piece consists of the counter electrode, the cover, and the connecting rod. The rod is adjustable by a set screw to achieve the optimum separation between the electrode and counter-electrode.

3.1.5. Thin film deposition

For most of the samples, after photolithography or e-beam lithography, a thin layer of metal is deposited in our e-gun evaporator or thermal evaporator. The e-gun evaporator[14] is used to evaporate Ti, Au, Al, Py, and Ni. It is equipped with an *in situ* etcher and a tiltable sample stage. The thermal evaporator with an *in situ* etcher is used to evaporate 5N Au or Al only. For this thesis, all work was done in the e-gun evaporator, thus we will only describe the evaporation procedure and conditions for the e-gun evaporator. The chamber is pumped by a diffusion pump for a few hours until the pressure drops to $1 - 5 \times 10^{-7}$ Torr. For samples that need a plasma etch, 40 mTorr Ar is introduced after closing the diffusion pump. A 60 Hz AC power supply applies 400 V to the sample stage to generate a plasma. The sample is etched for 80 seconds. After etching, the chamber is immediately pumped down. The metal is evaporated by a 3 kW e-gun. The metal is preheated with the electron beam without opening the shutter. After the desired evaporation rate is achieved, the shutter is opened to allow metal evaporation to start. After the desired thickness of metal has been evaporated, the shutter is closed and the power supply is turned off. The thickness and the evaporation rate is monitored by a thickness monitor. Typical evaporation rates are 0.4-1.0 Å/s for Ti, 1.5-10 Å/s for Au, 0.4-5.0 Å/s for Al and 0.1-0.6 Å/s for Py and Ni. The actual rate depends on the condition of the power supply and how well the metal sits in the crucibles. The amount and position of the metal shots needs to be fine tuned to achieve an optimum evaporation rate. If more than one type of metal is deposited, at least 20-minute pumping between the two depositions is used.

[14]Built by José Aumentado. Schematic can be found in Ref. [**101**].

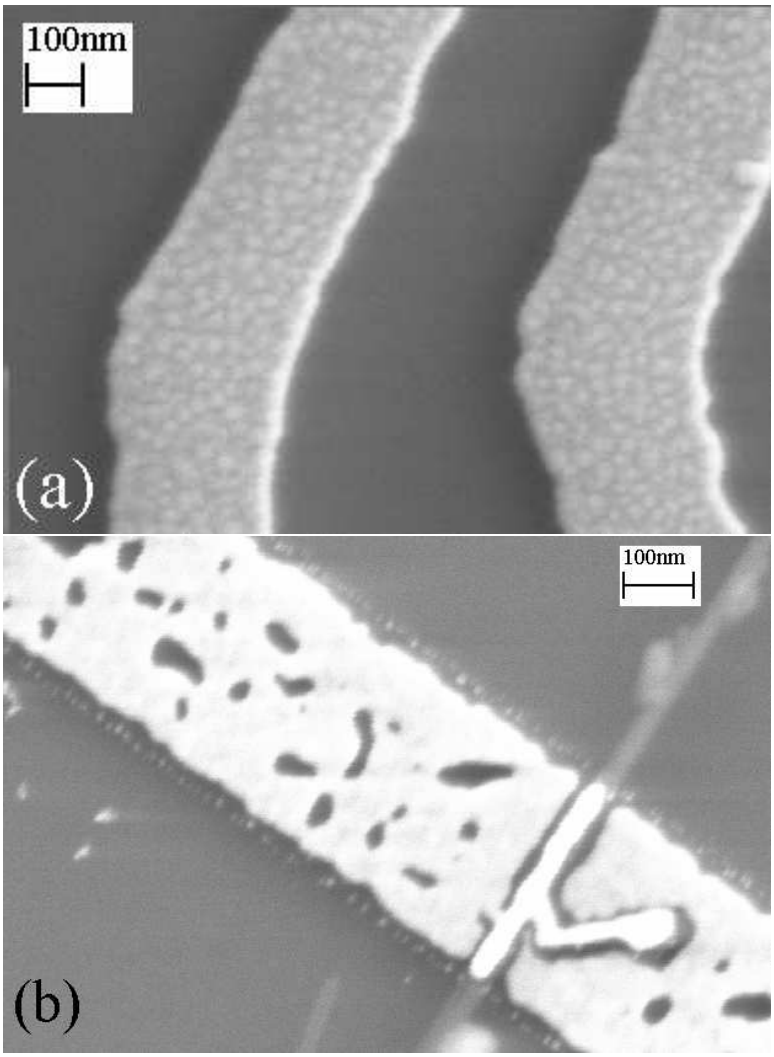

Figure 3.8. (a) The grain structures of a Ti/Au film. The Ti layer is 4 nm thick and Au layer is 44 nm thick. (b) Nonuniform film for a 5 nm thick Au layer.

Grain structure is observable in some of the metals such as Fig. 3.8(a). If the film is too thin, it tends to become nonuniform as in Fig. 3.8(b). The grain structure and uniformity can be an important factor in achieving good metal-CNT contacts.

3.1.6. Lift-off process

After metalization, the sample is fully covered by the thin film. The unwanted parts of the film are removed by the lift-off process. Depending on the resist used for patterning, the lift-off process is different.

For the LOR/Photoresist pattern, the sample is immersed in Photoresist Remover 1165[4] at 70 °C for 30 minutes. Most of the unwanted metal scrap will be lifted-off in this step. The sample is then transferred to a second bath of Photoresist Remover 1165 at 70 °C for 30 minutes. This is to ensure a clean lift-off. Finally the sample is rinsed in DI water and isopropyl alcohol before being blown dry using N_2 gas.

For the PMMA/Copolymer pattern, the sample is immersed in acetone and a syringe is used to shoot acetone on the sample surface to facilitate lift-off. If the unwanted metal does not come off immediately, the sample will be soaked in acetone for some time. Depending on the condition of the PMMA, this time is from 15 minutes up to overnight before the lift-off can be thoroughly achieved. The sample is then rinsed in clean acetone, followed by isopropyl alcohol before being blown dry by N_2 gas.

3.1.7. Carbon nanotube sample fabrication procedure

Fabrication of CNT devices uses the same basic techniques described above. But as we cannot control the positions of the nanotube on the substrate, special procedures have been developed.

We first photolighographically pattern big gold pads on those substrates that will be used later for wirebonding. Then we use electron-beam lithography to pattern gold alignment marks in the central region of the photolithographically defined pattern. The typical design for the alignment marks is shown in Fig. 3.9(a). Each individual alignment mark is unique as this can help in finding the exact location without counting the number of marks. MWNTs obtained from Prof. R.P.H Chang's group suspended in dimethylformamide (DMF) are spun on the substrate. Those MWNTs were grown by an arc-discharge method without catalyst [**102**]. We then use the high resolution LEO SEM[15] to find the MWNTs and map out their position with regard to the alignment marks. Electrodes connecting the MWNTs and the big gold pads are designed according to the map and patterned using electron beam lithography. Figure 3.9(b) shows the AutoCad design pattern and Figs. 3.9(c)(d) show the actual device. Prior to metal deposition, an O_2 plasma etch was performed for 1-10 seconds. This significantly improves the contacts and the contact resistances decrease from an average of a few MΩ to below one kΩ. (The contact resistance is further discussed in Chapter 4.) Why is an O_2 plasma etch such an efficient way of improving the contacts? Figure 3.10 shows a transmission electron microscope (TEM) image of a MWNT that is from the same source as all our measured MWNTs. We can see a lot of amorphous carbon covering the outside

[15]LEO Gemeni 1525 located at the EPIC facility at NUANCE center.

of the CNTs. Our initial guess was the O_2 plasma etch removes the amorphous carbon. We were worried that the O_2 plasma etching might etch through the amorphous carbon and damage the CNTs. However, the subsequent TEM image after plasma etching still shows CNTs coated with amorphous carbon and the CNTs do not show visible damage from the etch. Although it is good to know that our tubes are not damaged, this also shows our initial guess was wrong. We have several possible explanations, but are not exactly sure why the contacts are improved at this point. One possible explanation is the TEM can deposit a lot of amorphous carbon. Even though the plasma etch had etched away the amorphous carbon, it was redeposited during the image process. Secondly, it is possible that the plasma cleaning process removes the residual PMMA resist left on the CNT surface after the development process. Finally, we cannot completely rule out that the plasma process will not introduce defects, as suggested by other groups [**103**].

3.2. Measurement Setup

Our measurement is carried out both in a ^{3}He refrigerator and a dilution refrigerator. The ^{3}He cryostat was purchased from Janis Research Company, Inc.[16]. It can reach 260 mK at base temperature. The temperature is read out by a homemade temperature bridge [**104**] from a 1 kΩ RuO_2 thermometer. The samples are mounted on the end of a cold finger that extends from the ^{3}He pot. A home made proportional-integral-differential (PID) control unit is used for temperature stabilization. The circuit diagram can be found in Refs. [**100**, **104**]. A two-axis magnet which can reach 3 Tesla perpendicular to the sample plane and 1.8 Tesla

[16]Janis Research Company Inc. Wilmington, MA.

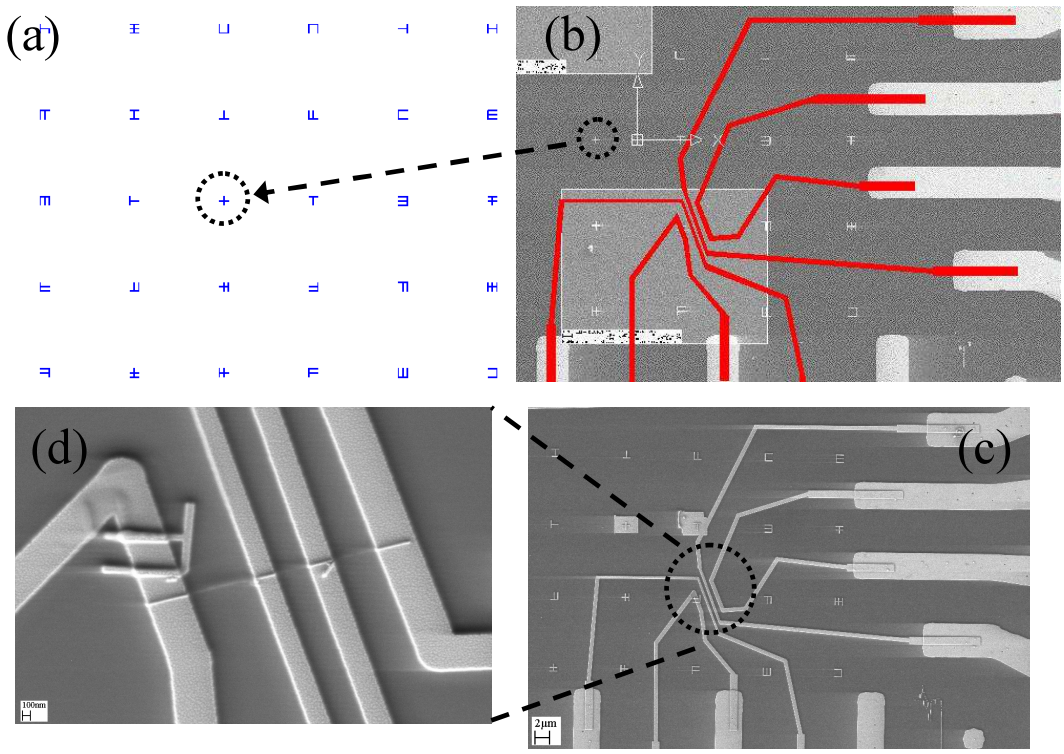

Figure 3.9. (Color) (a) Alignment mark pattern used to locate the CNTs. The total size of the pattern shown is 50 μm $\times$ 40 μm. The size of each mark is 2 $\times$ 2 μm^2. (b) An AutoCAD design for e-beam patterning. The circled cross is the corresponding mark in (a). (c) An SEM image of one of our samples. (d) Zoom-in view of the device.

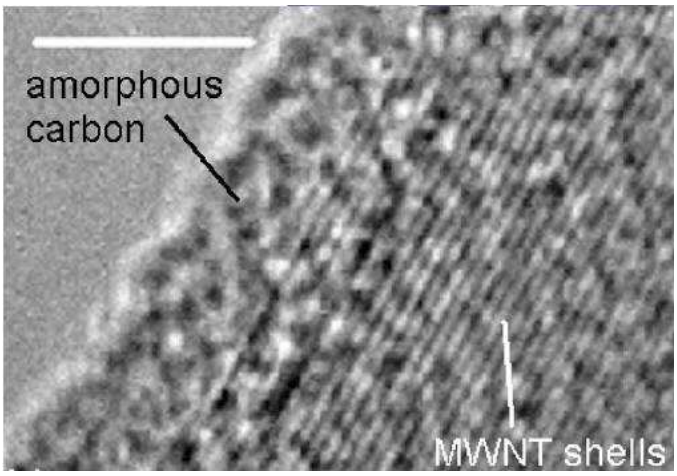

Figure 3.10. A TEM image of a multiwalled carbon nanotube coated with a layer of amorphous carbon. Image was taken by Dr. Dmitriy A. Dikin.

parallel to the sample plane[17] is attached to the dewar used by this refrigerator. The magnet can run in current or voltage mode. A 20 A Kepco bipolar power supply[18] or a 1 A Kepco bipolar power supply[19] can be used to energize the magnet.

The dilution refrigerator is an Oxford Kelvinox 300 dilution refrigerator[20] and it can cool the samples down to 15 mK. In this refrigerator, a RuO_2 thermometer[21] is used to read out the temperature. The RuO_2 thermometer was calibrated against another calibrated Ge thermometer[22]. A TRMC2 bridge[23] is used to read the temperature with a small current of only 80 pA at the base temperature. The readout is used as the input to a PID controlling circuit similar to the one used in the ^{3}He refrigerator if the temperature needs to be stabilized. To minimize the noise interference, care was taken about grounding and filtering. On the top of the refrigerator, π-section filters with a cut-off frequency of 5 MHz were installed. The electrical lines from the π-filters are connected to a breakout box inside a mumetal shielded box[24].

At the beginning of each measurement, the noise is checked by a spectrum analyzer[25]. The noise level was recorded for 60 Hz noise and the background noise. The background noise is then compared with the theoretical noise of the sample plus the noise from the amplifier. The theoretical noise is composed of three parts: Johnson noise, shot noise and

---

[17]From Cryomagnetics, Inc., Oak Ridge, TN.
[18]Kepco Bop 20-20M, from Kepco, Inc. Flushing, NY.
[19]Kepco Bop 100-1M, from Kepco, Inc. Flushing, NY.
[20]From Oxford Instrument Inc., UK.
[21]Model SMT1206R from Vector Electronic Company, North Hollywood, CA.
[22]Calibrated by Lake Shore Cryotronics inc. Westerville, OH.
[23]Purchased from AIR LIQUIDE DTA, France.
[24]Designed by Sergey Rozhok, manufactured by Amuneal Manufacturing Corp..
[25]SR760 FFT spectrum analyzer, from Stanford Research Systems.

flicker noise [**105**]. With zero current and ideal resistor R, the shot noise and flicker noise is zero. The theoretical Johnson noise is $< \delta V^2 >= 4k_BTRd\omega$. We need to consider the Johnson noise of the sample in the refrigerator at low temperature and the Johnson noise of the balance resistors in the resistance bridge at room temperature. We generally can minimized the background noise down to 15 nV/$\sqrt{Hz}$, which is close to the 10 nV/$\sqrt{Hz}$ Johnson noise of the sample plus the 4 nV/$\sqrt{Hz}$ input noise from the AD 624 amplifier[26]. A magnet which can reach 12 Tesla is attached to the dilution refrigerator. The field direction is perpendicular to the sample plane. After turning on the magnetic field, the noise goes up as the magnet will generate 60 Hz noise.

For most of the measurements performed in this thesis, the samples were measured by a four-probe method with ac resistance bridges[27]. The circuit diagrams of our measurement electronics are shown in Figure 3.11. The excitation current is generated by a lock-in amplifier (PAR 124[28]). The "A" and "B" ports are connected to a AD624 differential amplifier and sent to the input of the lock-in amplifier. The analog dc output from the lock-in amplifier is read by a HP multimeter[29]. We often measure the differential resistance as a function of dc bias current. The part inside the dashed line box in Fig. 3.11 is used for sending the bias current. If one is interested only in the zero bias resistance, this part does not need to be connected. A HP synthesizer[30] is used to drive the input of the current source (Figure 3.12(a) shows the circuit diagram of the current source.). As we need to measure the ac

[26]Manufactured by Analog Devices, Inc., Norwood, MA.
[27]This is an Adler-Jackson type bridge, based on a General Radio 1433-X or 1433-F decade resistance box.
[28]From Princeton Applied Research, Princeton, NJ.
[29]Model 34401A, from Hewlett Packard, Cupertino, CA.
[30]Model 3325A, from Hewlett Packard, Cupertino, CA.

resistance as a function of dc bias current, we normally sweep the the voltage by the HP synthesizer at a very low frequency (0.3 mHz).

Alternatively, we do direct four-terminal measurements using the circuit shown in Figure 3.11(b) as a double check to avoid experimental artifacts. In this case, a summer is used to sum the ac current excitations with dc bias current. The circuit diagram for the summer is shown in Fig. 3.12(b).

One challenge in doing low temperature measurements is how can we be sure the temperature reading is accurate. Meticulous calibration of the thermometer is required. But the art of calibration is beyond the scope of this thesis. Here we only describe several techniques to ensure the sample temperature is the same as the thermometer. The primary cause for the difference is heating effect from the current applied to the sample. To avoid this problem, we do systematic checks. One method is the check the temperature dependence of the sample resistance down to the base temperature of the refrigerator, if the resistance showed no sign of saturation while the sample cools down, we can then state the current does not heat the sample significantly. The other method is using different currents to see if they give the same result, if heating is absent, the readings should be identical. Another simple rule is to estimate the voltage across the sample, if the condition $eV \ll k_B T$, we can safely assume heating will not be significant.

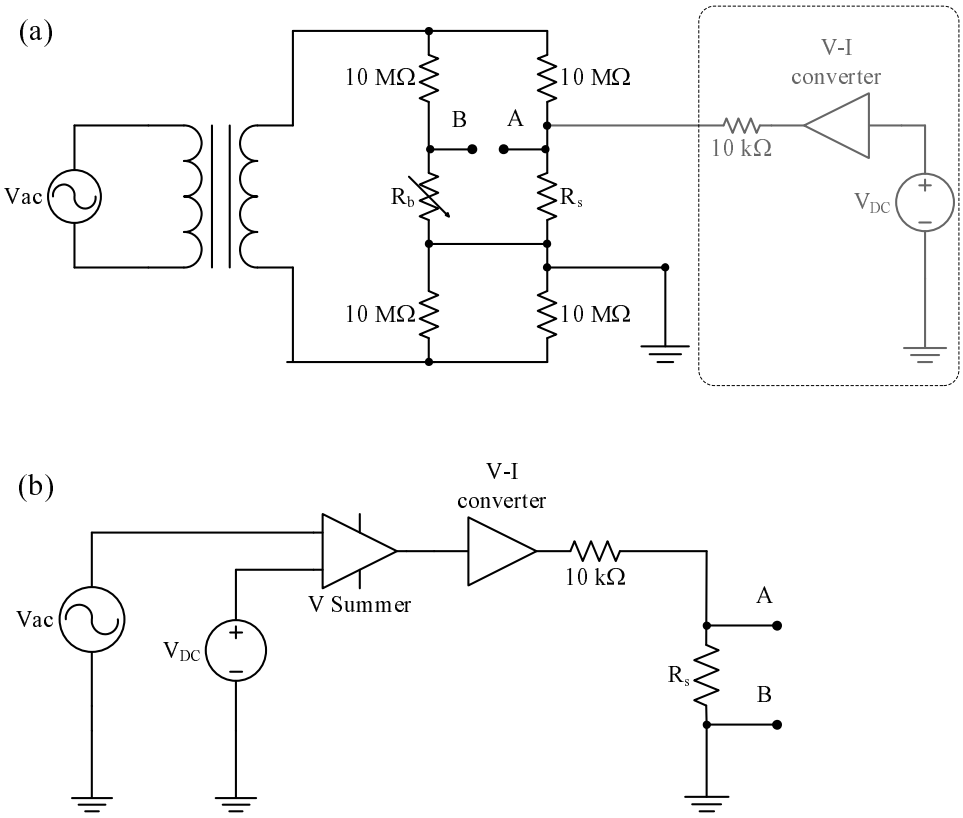

Figure 3.11. (a) Circuit diagram of differential resistance measurement by ac resistance bridge. The part inside the dashed box is not connected for zero dc current bias measurement. (b) Circuit diagram of differential resistance measurement by direct measurement. V_{DC} is the dc voltage, V_{ac} is the output of the lockin amplifier. Ports **A** and **B** are connected to the lock in amplifier input. The circuit diagram of voltage-current converter and voltage summer can be found in Fig. 3.12.

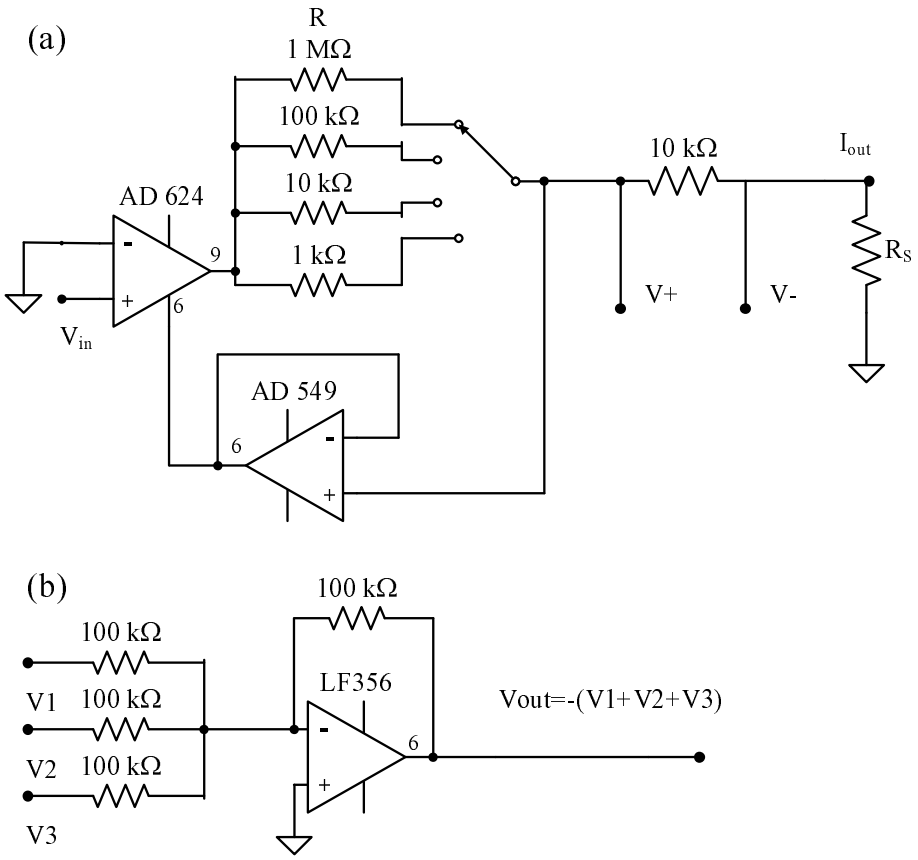

Figure 3.12. Circuit diagram of a homemade electronics utility box. (a) the current source converts the input voltage V_{in} to output current $I_{out} = V_{in}/R$, (R=1 kΩ, 10 kΩ, 100 kΩ, 1 MΩ). Ports **V+** and **V-** are used to determine the current by measuring the voltage drop over the 10 kΩ resistor. (b) the voltage summer, whose output voltage is the inverted sum of the input. If one of the inputs is not used, it should be left floating.

CHAPTER IV

Results and Discussions

In this chapter our measurement results and discussion will be presented. Over the course of the thesis work, 102 CNT devices were fabricated. 82 devices appeared to be viable after the fabrication process on inspection with a SEM and were wirebonded for measurement. Of these, 32 samples were cooled down in a refrigerator[1], from which 29 samples were studied in detail. We will only show data from a selected subset of these 29 samples. We begin with the specific techniques to measure these CNT samples[2]. After the results of MWNTs are shown, we will present our analysis and interpretation of our findings. This work has been published in Refs. [**106**, **107**].

4.1. Probe Configurations and Data Presentation Format

Our MWNT devices have multiple electrodes. In the early devices, four electrodes were patterned on each MWNT, enabling four-terminal measurements on those devices. Later devices with eight electrodes were fabricated because the additional leads provided us the possibility of measuring the four-terminal resistance of the contacts in addition to the four-terminal resistance of the device. Compared to the standard two-terminal devices often used by other groups, our devices allowed measurements that provided much more information about the device. Figure 4.1 shows a typical MWNT device which has eight leads. The

[1]Either in the ^{3}He or the dilution refrigerator.
[2]Techniques that are generally used are discussed in Sec. 3.2.

leads are numbered to distinguish different measurement configurations. The electronic circuits for the four terminal measurement can be found in Fig. 3.11. We shall use the notation $R_{mn,kl} = dV_{kl}/dI_{mn}$, ($G_{mn,kl} = 1/R_{mn,kl} = dI_{mn}/dV_{kl}$) as the differential resistance (conductance) with leads m, n as the current leads, and leads k, l as the voltage leads. There is more than one configuration to measure the CNT four-terminal resistance. The most often used configuration is $R_{14,23}$ ($G_{14,23}$), using the outside (inside) leads as the current (voltage) leads. Classically, this is the configuration that excludes the contact resistance, however, in mesoscopic devices where the phase coherence length is comparable to the device size, the influence of contacts cannot be completely eliminated. The dc bias is sent through lead 1 and taken out from lead 4, where lead 4 is ground. Unless otherwise noted, for brevity, R or R_{4t} (G or G_{4t}), omitting the indices, will be used for the configuration $R_{14,23}$ ($G_{14,23}$). I is used for the dc current I_{14}. $R_{23,14}$ was also used from time to time to check the consistency of the device measurement as well as to check the Landauer-Büttiker probe symmetry, also known as the Onsager symmetry relation as described in Sec. 2.2.3. Other configurations such as $R_{67,23}$ ($G_{67,23}$) were also used occasionally to check the consistency of the data. We note that configuration $R_{67,23}$ ($G_{67,23}$) includes the resistances of the two inner contacts. The differential resistance of the two contacts was measured using the configuration $R_{23,61}$ and $R_{23,47}$. The notation $R_{C1} = R_{23,61}$, $R_{C2} = R_{23,61}$ will also be used when there is no danger of confusion. In the early devices, only four electrodes (1,2,3,4) were patterned. In these devices, it is impossible to directly measure each of the individual contact resistances. For those devices, the contact resistance R_C was estimated from the difference between the

two-terminal and four-terminal resistance using the equation

$$R_C = (R_{23,23} - R_{14,23})/2 - R_{ext}, \tag{4.1}$$

where R_{ext} is the resistance of the wire from the sample stage to the breakout box plus the resistance of half of the lead resistance in the chip. In the ^{3}He refrigerator, $R_{ext} \approx 180\ \Omega$ for a typical sample. As will be discussed later, the samples are metastable, therefore it is important that the time interval between different measurement be minimized. Ideally, measurements of R, R_{C1} and R_{C2} should be done simultaneously. We have verified this by using two or more resistance bridges with ac excitations at different frequencies, but with a common ground, simultaneous measurements of different sections of the same device did not interfere with each other. However, in our measurement setup, the "mu-metal box" had space only for measurement electronics for two simultaneous measurements. The simultaneous measurements were therefore R with R_{C1}, R_{C1} with R_{C2}, or R with R_{C2}.

It is advantageous to have a gate control for the CNT devices. A backside gate was used by making electric contact to the backside silicon as shown in the schematic in Fig. 4.2. In early experiments, we found the backside gate had no effect on the MWNT resistance. However, this might have been due to the fact that the silicon wafers were not highly doped and might have been insulating at low temperatures. Thus highly doped silicon wafers were used in later experiments.

Although we measure R and I, sometimes it is more convenient to discuss the data in terms of G and V_{dc}. This is because the conductance G is directly related to the Landauer

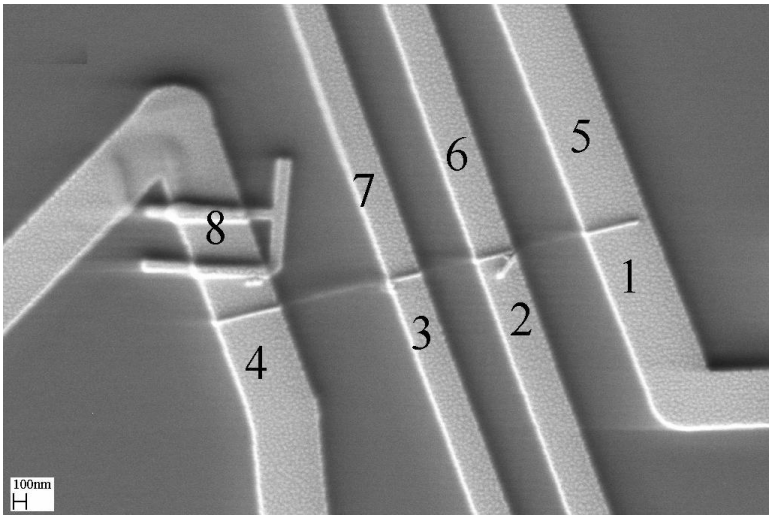

Figure 4.1. An SEM image of one of our MWNT devices (Sample C). The numbers are used as indices for referring to different measurement probe configurations.

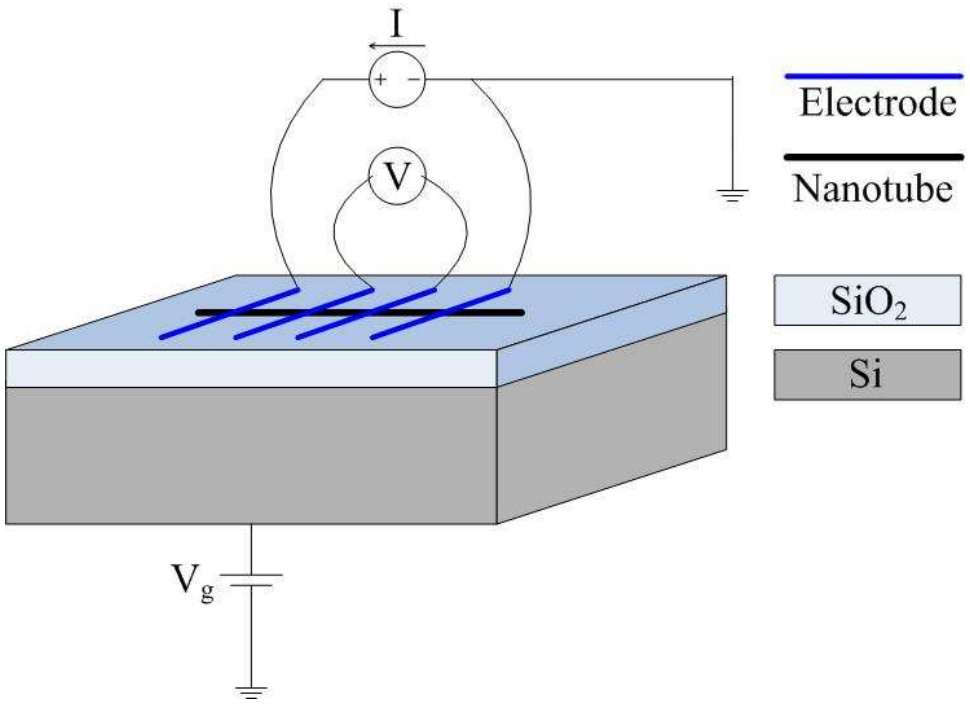

Figure 4.2. (Color) Schematic of four-terminal measurement of CNT resistance with a backside gate.

formula and V_{dc} defines the energy scale. G is obtained by calculating the inverse of the resistance R ($G = 1/R$) and V_{dc} is obtained by numerical integration of dV/dI versus I. We further express G in units of e^2/h.

Table 4.1 shows R_{4t}, and R_C of 14 samples that were measured in detail at different temperatures. We can see that although those samples were fabricated in the same manner, their characteristics are different from each other. At room temperature, R_{4t} is 1.3 kΩ for Sample B and 29.0 kΩ for Sample M. The difference is nearly 30 times. R_C also varies a lot as the lowest in Sample D and highest in Sample E. We note that, for the sample resistances R_{4t}, they appear to increase with the decreasing temperature. Although this is a general trend, for some low resistance samples, such as Sample C, this temperature dependence can be different as will be discussed in Sec. 4.3. For the contact resistances R_C, they can either increase, decrease, or show non-monotonic behavior with decreasing temperature as shown for Samples E, G, and C respectively. As we believe it is unnecessary to describe all our samples in great detail as many of them share the same characteristics, we choose Samples A-E to represent the general characteristics observed in all of our samples.

As an example, Fig. 4.3 shows our preliminary measurement of the sample resistance and the two contact resistances of Sample C as we cool down the sample from the room temperature to the base temperature of the dilution refrigerator. As we can see, at room temperature or liquid nitrogen temperature, the $R(I)$, $R_{c1}(I)$ and $R_{C2}(I)$ curves are almost featureless, while at 23 mK, very sharp structures can be observed in all three resistances. For the MWNT resistance, as the sample cools down, the resistance increases, while for both of the contact resistances shown here, they decrease as the temperature goes down. Our

Table 4.1. Resistance table of selected samples at room temperature (RT), liquid nitrogen temperature (77 K LN_2), liquid helium temperature (4 K LHe) or other specified temperature.

Sample	Temp	R_{4t}(kΩ)	R_C (kΩ)	Sample	Temp	R_{4t}(kΩ)	R_C (kΩ)
A	RT	2.2		H	RT	11.0	
	LN_2	2.4			LN_2	18.3	
	LHe	4.9	1.0[a]		LHe	44.0	3.8[a]
	300 mK	6.3			300 mK	70.0	
B	RT	1.3		I	RT	7.1	
	LN_2	2.3			LN_2	11.0	
	LHe	3.1	0.9[a]		LHe	19.0	1.0[a]
	300 mK	3.6			300 mK	39.0	
C	RT	1.78	0.247 0.326	J	RT	3.1	0.7[a]
	LN_2	2.03	0.206 0.158		LN_2	4.4	0.5[a]
	12 K	2.06	0.173 0.133		12 K	6.4	0.25[a]
	18 mK	3.00	0.700 0.122		18 mK	8.3	0.35[a]
D	RT	1.31		K	RT	2.23	
	LN_2	1.42			LN_2	3.76	
	LHe	1.75	0.1[a]		LHe	6.8	1.0[a]
	300 mK	1.71			300 mK	13.0	
E	RT	5.5	0.40 0.30	L	RT	5.6	0.20 0.15
	LN_2	8.3	0.60 0.50		LN_2	13.0	0.73 0.48
	300 mK	28.0	5.0 6.0		300 mK	36.0	5.40 1.40
F	RT	2.9	0.40[a]	M	RT	29.0	0.20 0.30
	14 K	3.6	0.44[a]		14 K	35.0	0.19 0.22
G	RT	2.65	0.185 0.38	N	RT	2.6	0.20 0.18
	LN_2	4.69	0.155 0.34		LN_2	5.0	0.46 0.36
	300 mK	8.26	0.140 0.31		300 mK	11.7	0.70 0.60

[a] Estimated by Eqn. 4.1

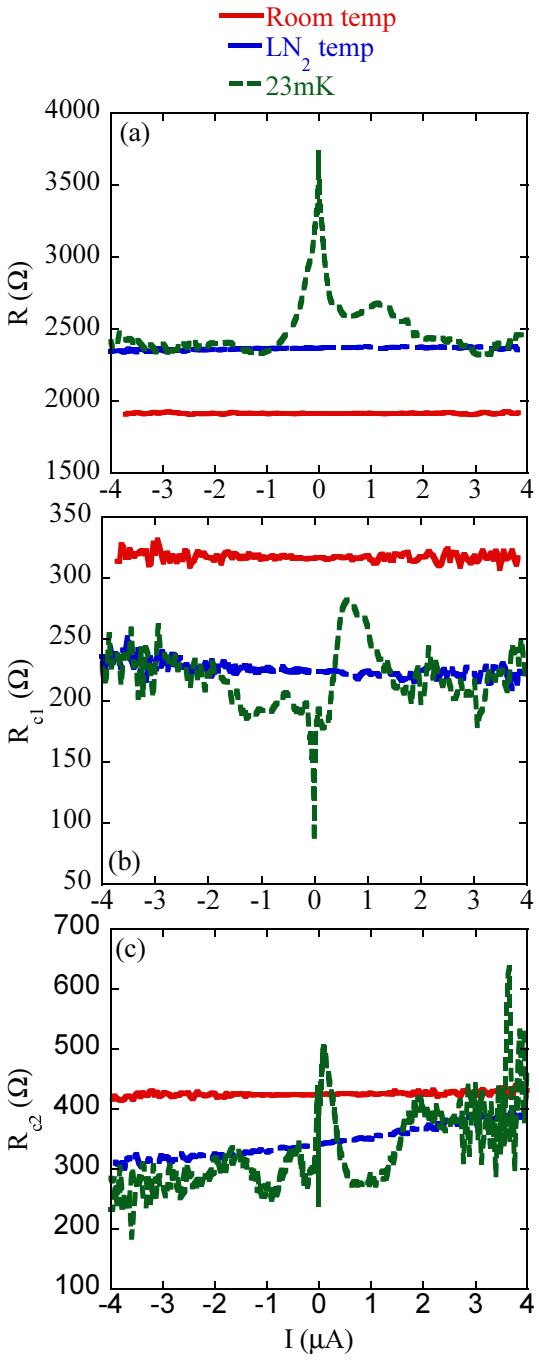

Figure 4.3. (Color) (a) The sample resistance R, (b) the contact resistance R_{C1} (c) the contact resistance R_{C2} of Sample C as a function of dc current I. The red (blue) curve is the data measured at room (liquid nitrogen) temperature. The green curve is the data measured at 23 mK, which is close to the base temperature of our dilution refrigerator.

main interest has been to study the low temperature behavior and the underlying physics of those features.

For low temperature measurement of samples with resistances on the order of kilo-ohms, special care needs to be taken to avoid measurement artifacts. Before measurement, the electronic circuits are checked carefully. The offsets of the amplifiers are minimized to the level of 0.2 nA, which corresponds to 2 μV for a 10 kΩ sample. By using different ac excitation currents, different probe configurations, and different electronic circuits, we are confident that no unwanted heating of the samples occurs, no shorts exist in our samples, and our electronic circuits function correctly. Only after these careful measures were taken, did we proceed to detailed, systematic studies. The current heating should not be significant if the voltage across the sample satisfy the relation $eV < k_BT$. Figure 4.4 shows two traces of the measurement with different ac excitation current as 0.2 nA and 1.0 nA on Sample C. We can see there is little difference between the two curves, which confirms heating from the ac excitation current is not significant in our samples. Figure 4.5 shows that the four terminal resistance $R_{14,23}$ is consistently lower than the configuration $R_{67,23}$, which includes the two inner contact resistances R_{C1} and R_{C2}. This makes sense as the four-terminal resistance should be lower than the resistance including the contacts. However, the difference is not constant as a function of I, which indicates the contact resistances vary as a function of I. Our direct measurements of contact resistances confirm this conclusion. Figure 4.6 shows the ac resistance bridge (circuit diagram shown in Fig. 3.11(a)) and the direct four-terminal measurement of Sample C with the same parameters (circuit diagram shown in Fig. 3.11(b)). We can see the two curves closely resemble each other. The small

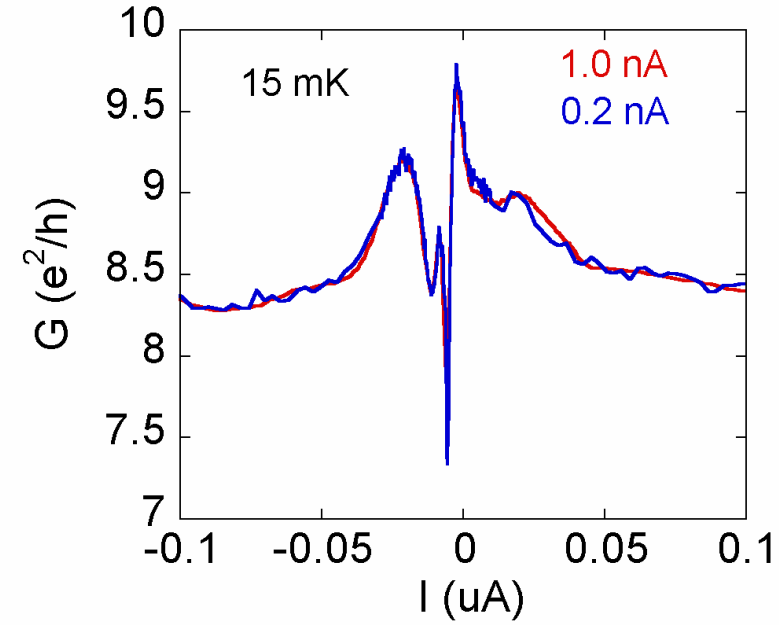

Figure 4.4. (Color) Measurements of Sample C at 15 mK with ac excitations of 1.0 nA, and 0.2 nA, respectively

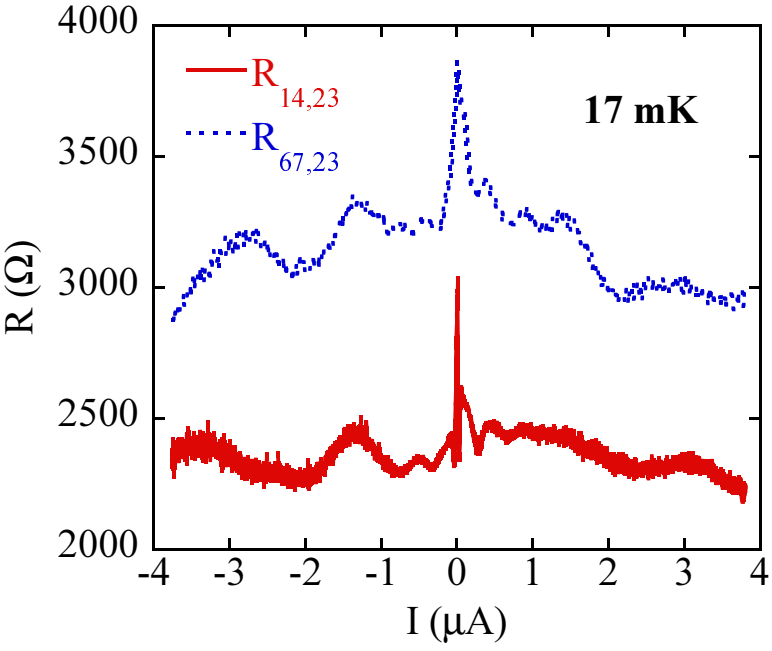

Figure 4.5. (Color) Measurements of Sample C at 17 mK with configurations $R_{14,23}$ (Red solid curve) and $R_{67,23}$ (Blue dotted curve). The dc bias current I is I_{14}

difference is due to a switching effect with the sample which will be discussed later. We conclude that our measurement circuits are good.

4.2. Multiwalled Nanotubes with Contact Resistances 1 kΩ or Higher

As an example of sample with high contact resistances, we first discuss Sample A. Figure 4.7 shows the four-terminal MWNT resistance at zero bias as a function of temperature. The resistance R increases monotonically when the temperature decreases. If the MWNT is semiconducting, it should obey thermal activation conducting behavior which is governed by the formula [**24**],

$$1/R = G \propto \exp(-\frac{E_g}{k_B T}), \tag{4.2}$$

where E_g is the energy gap. 1D, 2D, and 3D variable range hopping models were also used to fit our data. For variable range hopping, the temperature dependent conductance is given by [**108**]

$$1/R = G \propto \exp(-(T_0/T)^{\frac{1}{d+1}}), \tag{4.3}$$

where T_0 is a constant which depends on the localization length ξ and d is the sample dimensionality with respect to the localization length ξ. As we can see in Fig. 4.7, none of the above models give good fits. Therefore new physics must be present.

From the discussion in Sec 2.2.4, 2.2.6, and 2.3.5, we know that experiments have shown that at low temperature in the tunneling regime, the conductance of CNTs is suppressed at

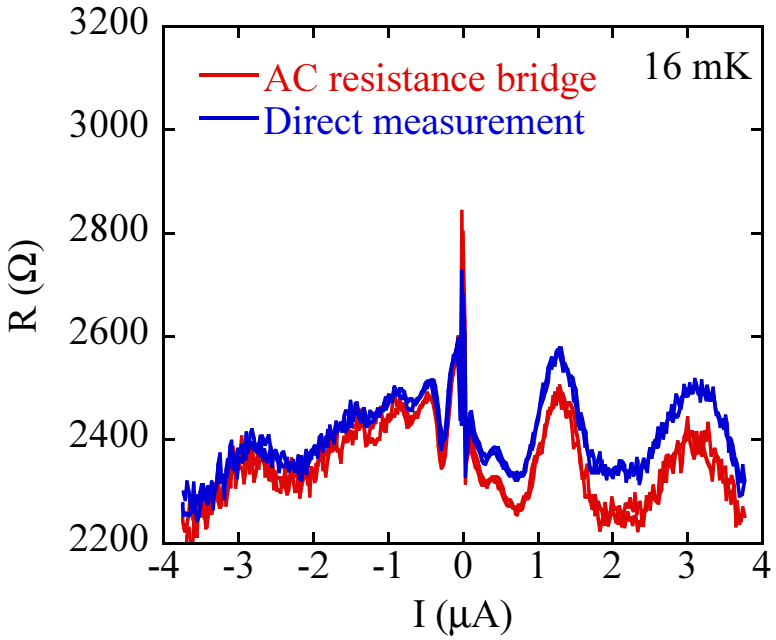

Figure 4.6. (Color) dV/dI vs I measurements on Sample C at 16 mK by an ac resistance bridge (red curve), and direct four-terminal measurement (blue curve).

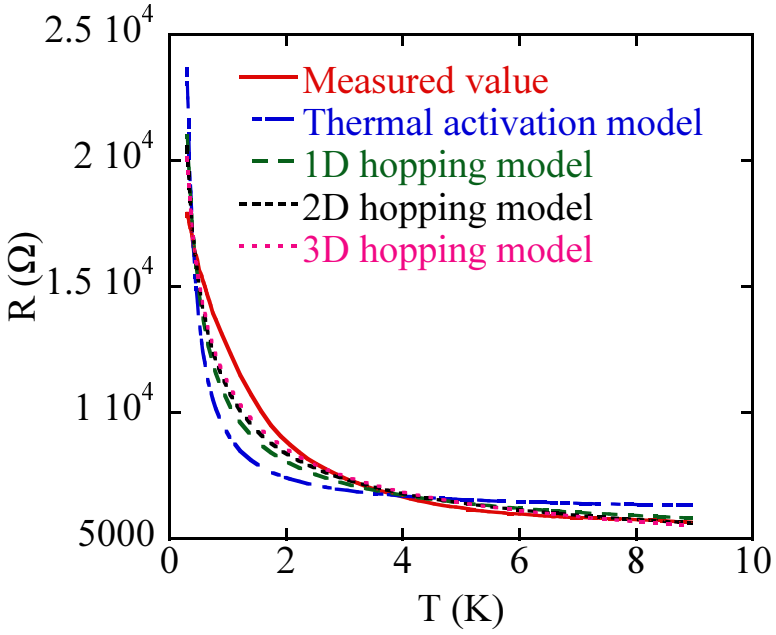

Figure 4.7. (Color) The temperature dependence of a high contact resistance Sample A with fits to thermal activation model, 1D, 2D, and 3D variable range hopping.

zero bias. A power law dependence of conductance has been found in both SWCNTs and MWNTs [**57**, **93**]. In the samples shown in Table 4.1, the contact resistances are much less than R_K=25.898 kΩ and so the sample is not in the tunneling regime. Occasionally, we have a "bad" sample with much high contact resistance. The characteristics are similar to those observed by other groups. We have found zero bias suppression in these samples with relatively high contact resistances. They are only absent in samples with contact resistances smaller than 400 Ω.

For Sample E with high contact resistances (the conductance of Sample E is similar to Sample A shown in Figs. 4.9(a)(b)), the contact conductance $G = 1/R_{C1(,C2)}$ varies as a function of bias current $I = I_{23}$ as shown in Fig. 4.8(a). The contact conductances show highly asymmetric behavior as a function of dc bias current. Both C1 and C2 show that when the bias current is going from the electrode to the MWNT, the conductance is high and when the current is reversed, the conductance is much lower. One possible explanation is a Schottky barrier appears between the CNT and the metallic electrodes. A Schottky barrier is formed when a metal comes in contact with a semiconductor. As the electron density in metal is much higher than in the semiconductor, the electrons diffuse from the metal to the semiconductor until a charge barrier is formed and the chemical potentials on both sides are equal. The electron-like negative charges accumulate at the surface of the semiconductor while the positive charges accumulate at the surface of the metal. Depending on the separation between these two layers of charges, the barrier can be small or big. For a Schottky barrier, the forward bias narrows the width of the barrier. Thus the forward bias configuration has higher conductance and the reverse bias has lower conductance. As the

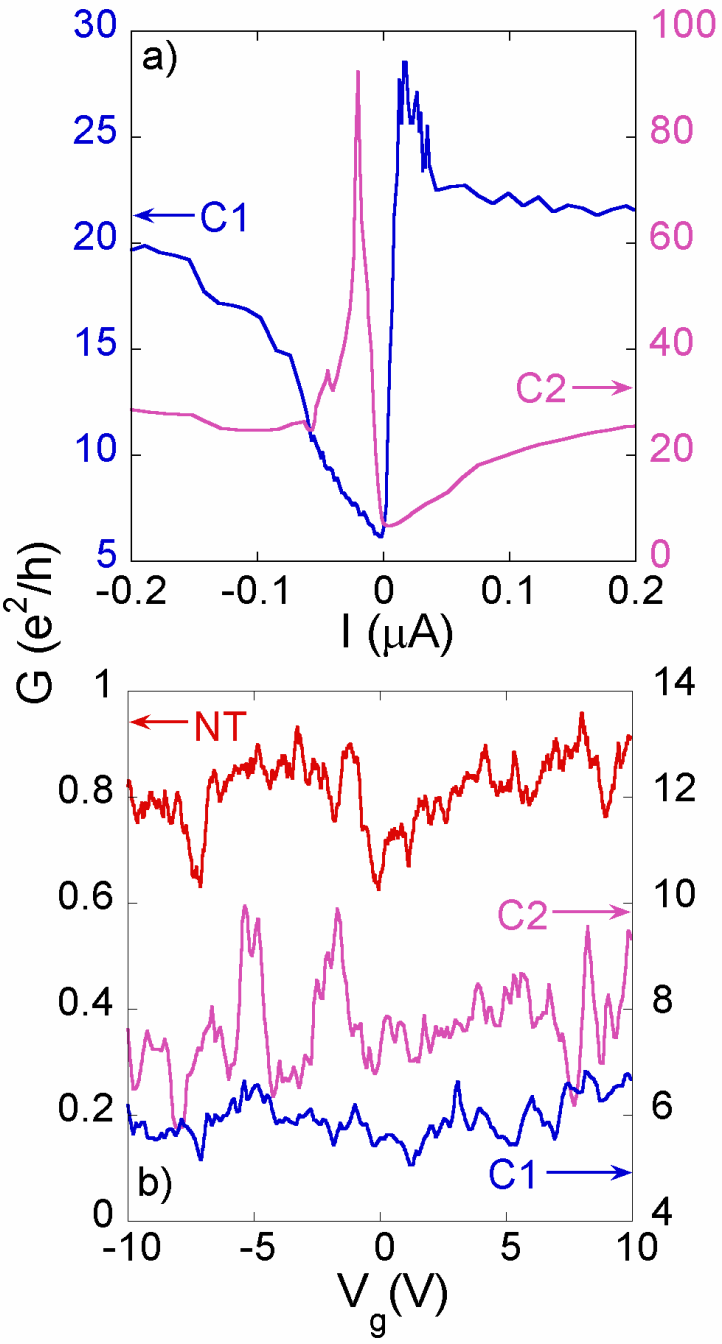

Figure 4.8. (Color) For Sample E with a high average contact resistance of 5 kΩ, (a) The contact conductance $C1$ and $C2$ as a function of dc bias current I at 330 mK. Here $I = I_{23}$ and G_{C1}, G_{C2} is defined in Sec. 4.1. (b) The differential conductance and the contact conductance as a function of backside gate voltage V_g. The correlation of the random fluctuations between the CNT and C1 is 0.66. Between the CNT and C2 is 0.27 and 0.22 between the two contacts C1 and C2.

voltage bias is much larger than the Schottky barrier height, the difference between forward bias and reverse bias will disappear. The work function of the materials and the geometry of the contact determine the height of the barrier. But the barrier also can be strongly influenced by impurities at the interface. A large device to device variation is expected. Semiconducting SWNTs have been found to form a Schottky barrier when in contact with a metal [**17**] or another metallic SWCNT [**109**]. A strong rectifying effect has also been observed in the junctions between a semiconducting SWCNT and a metallic SWCNT [**109**]. Although this theory is appealing, we cannot rule out other possibilities such as thermopower effects. The current actually heats the part of the sample of which results in an antisymmetric component of the conductance [**104**].

The gate voltage dependence of the sample conductance and contact conductances of Sample E is shown in Fig. 4.8(b). Without considering the fluctuation that appears to be random, the conductance of the whole MWNT device and both contacts show weak dependence on gate voltage, with slightly higher conductance at high positive gate voltage. This might be because it is a n-type semiconductor for the outermost shell.

All the above results of MWNT devices with high contact resistances are close to other groups' findings.

4.3. Multiwalled Nanotubes with Contact Resistances below 1 kΩ

The characteristics of samples with contact resistances higher than 1 kΩ are fairly similar to other groups' findings [**93**]. However, for samples with contact resistances below 1 kΩ, the behavior is fairly different and interesting. Figure 4.9 shows representative behavior of four

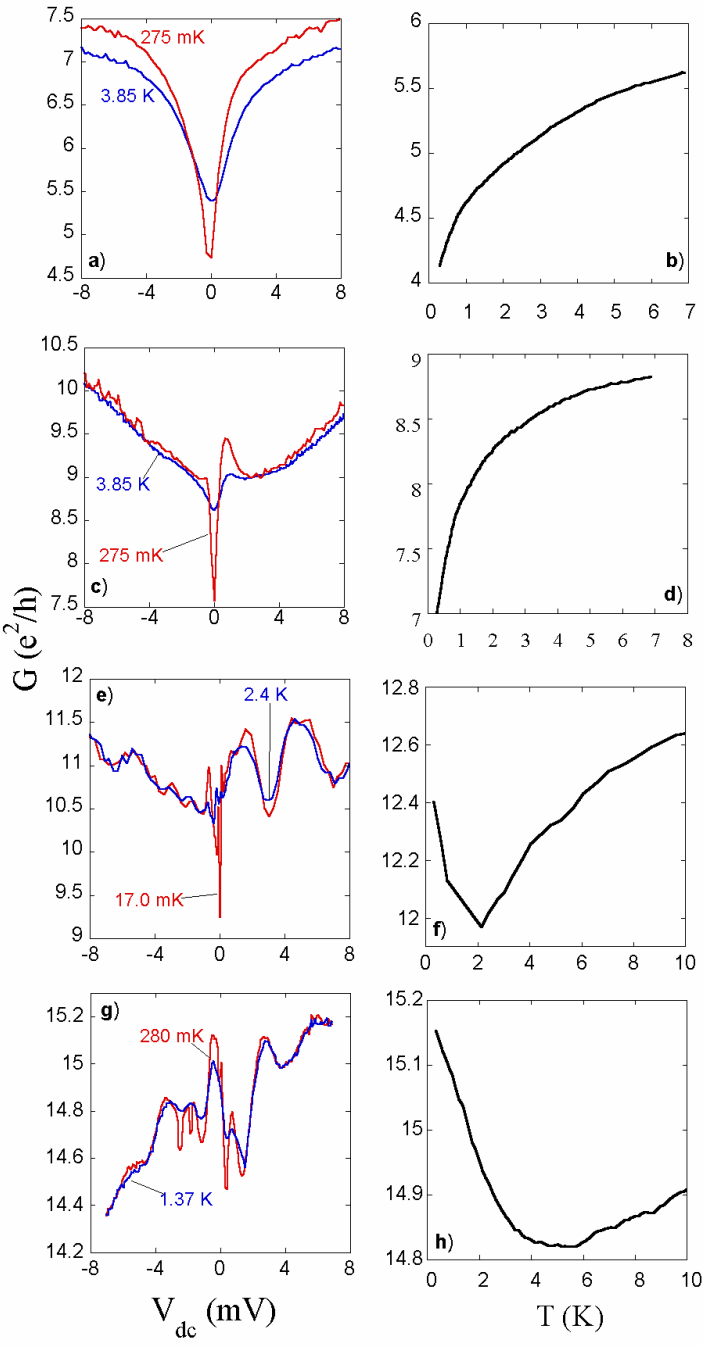

Figure 4.9. (Color) Differential conductance G vs voltage V_{dc} at two temperatures ((a)(c)(e)(g)) and zero-bias conductance vs temperature T ((b)(d)(f)(h)) for four different MWNT devices in decreasing order of contact resistances at 4 Kelvin. (a)(b) Sample A with an average contact resistance around 1 kΩ, (c)(d) Sample B with contact resistance around 900 Ω, (e)(f) Sample C with averaged contact resistance around 400 Ω, (g)(h) Sample D with contact resistance around 100 Ω. Adapted from Ref. [**107**].

devices. The left column ((a)(c)(e)(g)) shows the conductance G as a function of dc voltage bias V_{dc} at two different temperatures. The right column ((b)(d)(f)(h)) shows the measured zero-bias temperature dependence. The graphs are arranged in order of decreasing contact resistance. We can see the characteristic evolves with decreasing contact resistances. For Sample A with an average contact resistance at 1 kΩ, the conductance is nearly symmetric with a dip at zero bias. The dip goes deeper at lower temperature. The temperature dependence of G is monotonic, decreasing with decreasing temperature. For Sample B with 900 Ω contact resistances, the conductance still has a dip at zero bias, but we can see a small peak close to the dip and the shape is no longer symmetric with respect to zero bias. The dip drops lower and the peak goes higher at lower temperature. The temperature dependence of the conductance G is still monotonic decreasing with temperature. For Sample C with contact resistances at around 400 Ω, there are many more features and the features becomes sharper as the temperature decreases. However, for this sample, the temperature dependence is not monotonic. (We note that this sample shows metastable behavior. Both monotonic and nonmonotonic behavior was observed in the same sample.) After the sample is cooled down below 2 K, the conductance starts to increase, which is a typical signature of transport through a resonant state. The last sample, Sample D with contact resistances below 100 Ω, shows even more features and the turning point from decreasing conductance to increasing conductance is at around 4 K. We note that, the sharp features were only observed with low contact resistance samples at very low temperatures in a dilution refrigerator. This might be the reason why they have not been previously observed by other groups.

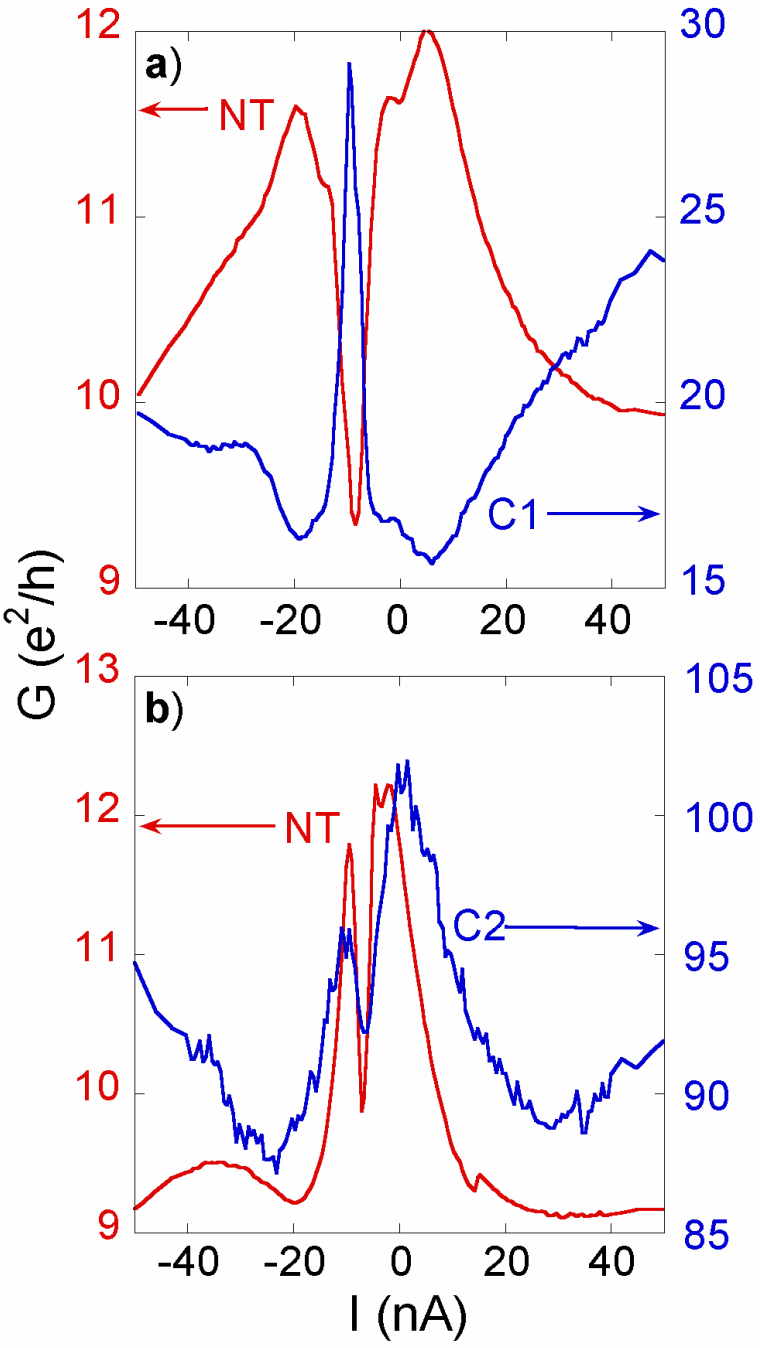

Figure 4.10. (Color) For Sample C with low contact resistance, (a) the simultaneous measurement of the CNT conductance and contact 1 (C1) conductance at 25 mK. (b) the simultaneous measurement of the CNT conductance and the contact 2 (C2) conductance. The correlation is -0.96 for CNT and C1 curves in (a) and 0.81 for CNT and C2 curves in (b).

We also performed direct four-terminal measurements of the contacts and the MWNT. As discussed in Sec. 4.1, we can only do two simultaneous measurements at the same time. Figure 4.10(a)(b) shows two consecutive simultaneous measurements. We found the sample behavior changed after the first measurement (See the difference between the measured conductance of MWNTs in Fig. 4.11(a) and (b). Both are quite different from the data shown in Fig. 4.9(e)). The cause of the change will be discussed later. As we can see, there are correlations between the sample resistance and the contact resistances. The correlation is -0.96 for the CNT and C1 curves in Fig. 4.10(a) and 0.81 for CNT and C2 curves in Fig. 4.10(b). The strong correlation reflects the long range phase coherence in the sample.

In addition to the large sample to sample variation shown in Fig. 4.9, the behavior in the same sample changes on different cooldowns. Figure 4.11 shows the conductance of Sample C in Fig. 4.9. Figures 4.11(a)(c) correspond to the first cooldown and Figs. 4.11(b)(d) correspond to the second cooldown, after warming up the sample to room temperature. The major feature in Fig. 4.11(a) is the conductance peak at around $V_{dc} = -25\mu V$. This feature grows as the temperature decreases. However, at zero bias there is a dip that also becomes sharper with decreasing temperature. Therefore the temperature dependence of G decreases with decreasing temperature as shown in Fig. 4.11(c). Figure 4.11(b) shows the conductance peak in Fig. 4.11(a) turns into a conductance dip on the second cooldown. The temperature dependence in Fig. 4.11(d) now increases with decreasing temperature, corresponding to the peak at zero bias. We note that for both the peaks and dips, the shapes look asymmetric. This feature turns out to be very important as will be discussed later.

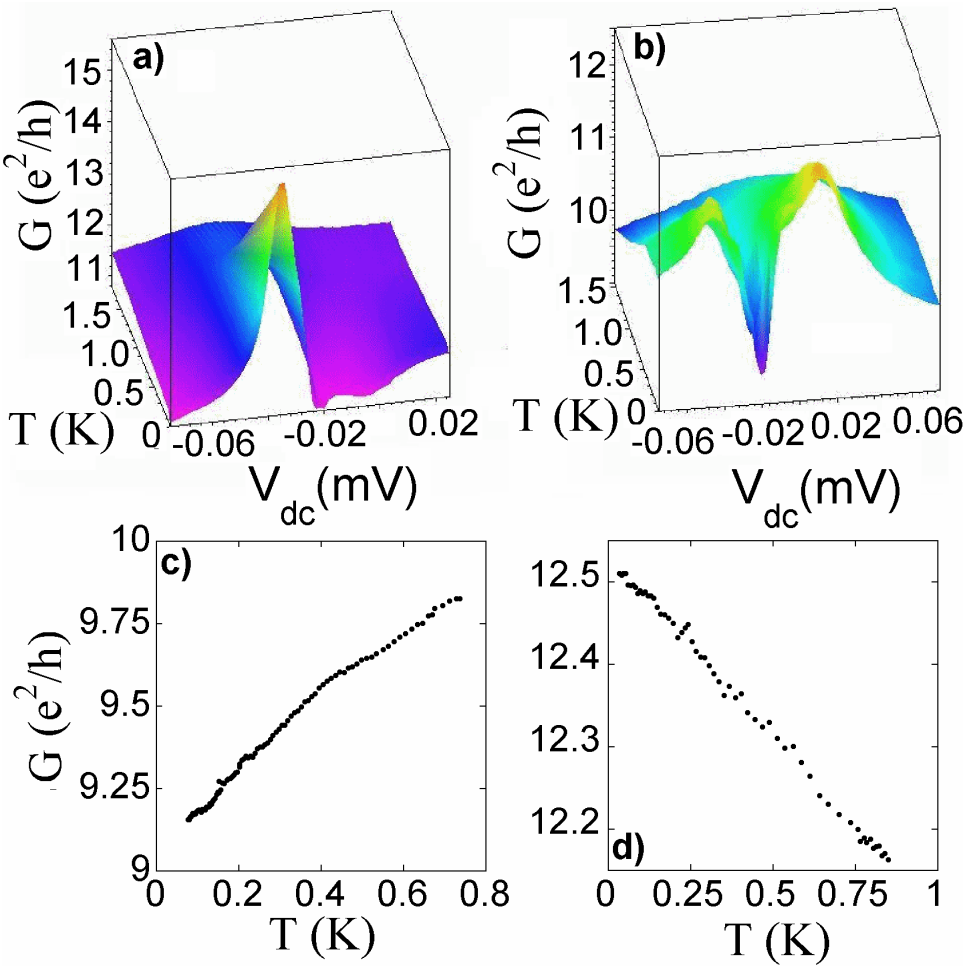

Figure 4.11. (Color) (a)(b) Three-dimensional representations of the differential conductance of Sample C as a function of voltage and temperature. (a) is on the first cooldown, at 20 mK, and (b) is on the second cooldown, at 16 mK, after warming the dilution refrigerator to room temperature. (c) and (d) are the corresponding temperature dependence of the zero-bias conductance. Adapted from Ref. [**107**].

We also found that it is not necessary to warm the sample to room temperature to see such changes. Warming up the sample to merely a few Kelvin can cause changes in the conductance, although generally not as dramatic as in Fig. 4.11(a)(b). This can be understood as arising from thermal annealing of the sample impurities or defects. At low temperature, the positions of the impurities or defects were in a certain configuration. When the temperature increases, the impurities or defects acquire more energy and become mobilized. After the sample is cooled down again, the impurities or defects will be "frozen" into a new configuration. It is evident that the features are associated with impurities or defects in the sample. For the most active impurity or defect, it can change as a function of time on the order of a few hours or a few days. This is also the reason why the CNT resistance in Fig. 4.11(a) and (b) are different. This interpretation also fits well with the random telegraph noise observed in the samples as shown in Fig. 4.12. If the impurities or defects can switch to different states as a function of time, a shift of impurity or defect position over the length scale of λ_F (λ_F is the Fermi wavelength) can result in a shift in the phase of the electron scattered from that impurity. This will cause a change in conductance on the order of e^2/h [**110**]. So the change of the active impurity of defect can be observed as a change in conductance on the order e^2/h just as shown in Fig. 4.12. The time dependent conductance changes are also known as "random telegraph noise" and have been observed in disordered metals [**111**].

For further investigation of quantum interference effects, one needs a "knob" such as a gate or a magnetic field that modulates the relative phase between different paths an electron can take. The random fluctuation may be a manifestation of the modulation of

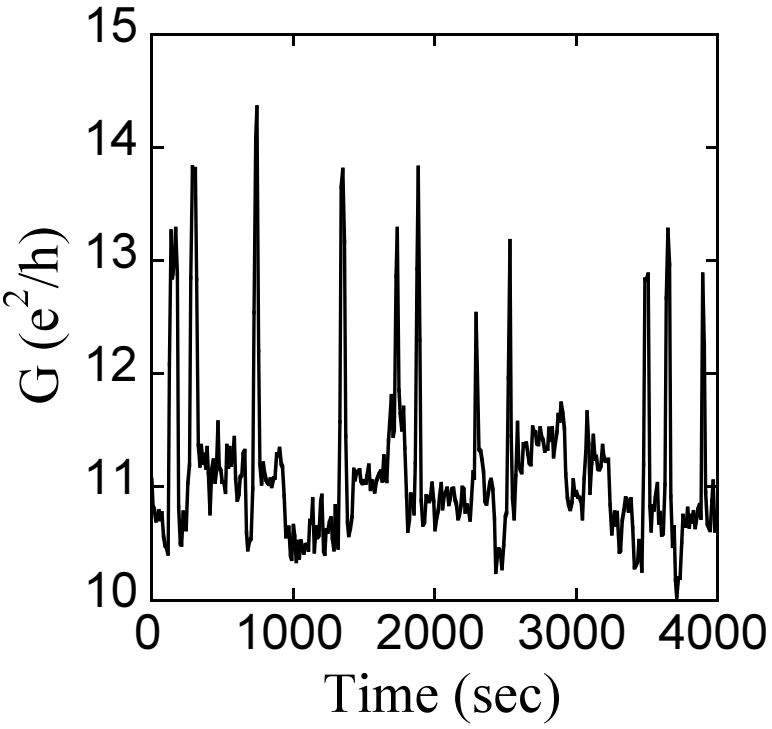

Figure 4.12. Time dependence of the zero-bias conductance of Sample C. Data taken at 35 mK.

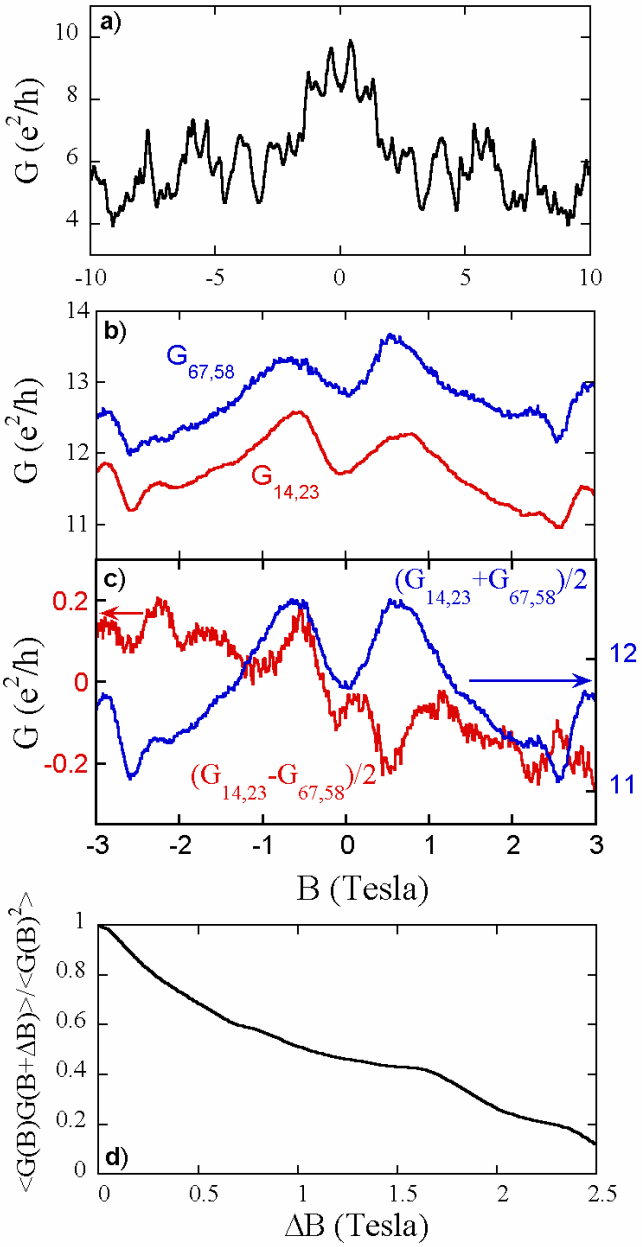

Figure 4.13. (Color) (a) Magnetoconductance of Sample C at 25 mK. (b) Low field magnetoconductance of the same device at low fields with two different measurement configurations as noted. $G_{67,58}$ has been shifted up by 1 e^2/h for clarity. (c) Average of the sum and difference of the two traces shown in (b), demonstrating the symmetric and antisymmetric combinations obtained using the Landauer-Büttiker relations. (d) Autocorrelation function of the magnetoconductance data of (a). The correlation field ΔB_c is 1.05 T. Adapted from Ref. [**107**].

the interference by a gate voltage as described in Sec. 2.2.5. The interference can also be tuned by applying a magnetic field. Figure 4.13(a) shows the magnetoconductance of Sample C at 25 mK. Large variations can be observed. It appears that the conductance is symmetric with $B = 0$. But closer inspection reveals that there are asymmetries in the data. This asymmetry is much more obvious with the data taken over a smaller range. (Data in Figs. 4.13(a),(b) are taken on different cooldowns.) $G_{67,58}(B)$ and $G_{14,23}(B)$ are measured simultaneously while sweeping the magnetic field. As 1 and 5, 2 and 6,3 and 7, and 4 and 8 are connected together (See Fig. 4.1), from the Landauer-Buttiker relation, we have

$$G_{67,58}(B) \approx G_{23,14}(B) = G_{14,23}(-B), \tag{4.4}$$

as given by Eqn. 2.41. Therefore $(G_{14,23}(B)+G_{67,58}(B))/2$ should be nearly symmetric while $(G_{14,23} - G_{67,58})/2$ should nearly antisymmetric with $B = 0$, just as shown in Fig. 4.13(c).

4.4. Discussions: Fano Resonances

From our previous brief discussions of our MWNT devices, it appears that the results can be explained by the physics of quantum transport in a diffusive system. However, a close inspection and in-depth analysis reveals several inconsistencies. First, in looking at the $G(V_{dc})$ curves, Figs. 4.9(c)(e)(g), it can be seen that the amplitude of the conductance fluctuations changes only in certain narrow ranges in dc bias with decreasing temperature, rather than over the whole range of V_{dc}. As an example, for Sample B in Fig. 4.9(c), the change of the conductance outside the voltage range [-2mV, 2mV] is very small, but inside this range, the conductance changes dramatically with changing temperature. Similar

behavior can be observed for Sample C and D in Fig. 4.9(e)(g). As we know, in a diffusive system, the amplitude of conductance fluctuations grows in the whole energy range [**40**]. In addition, in Fig. 4.13(a) the rms amplitude of the conductance fluctuation is 1.3 e^2/h, which is very close to theoretical calculation 1.4 e^2/h when $l_T, l_\varphi \gg L$ (from Eqns. 2.58 and 2.59). This appears to be supportive of quantum interference in the diffusive regime at first look; however, this implies that $l_\varphi \gg L$, where L=450 nm is the length of the CNT section between the two inner electrodes 2 and 3 in Fig. 4.1. From the expression for the correlation field ΔB_c (Eqn. 2.62) and the measured value from our experiment ΔB_c =1.05 T in Fig. 4.13(d), we can calculate that the phase coherence length $l_\varphi \approx 160$ nm for the width $W \approx 25$ nm of the MWNT, a factor of three smaller. Therefore, quantum interference in a diffusive system is unlikely to be the correct explanation for our results.

In summary, we observe large sample to sample variations of the conductance in MWNTs. Even in a single device, the sample characteristics change on thermal cycling and as a function of time. Conductance peaks and dips are seen as a function of bias. These peaks or dips do not necessarily occur at zero bias and are generally asymmetric with respect to the center of the peak or dip. These distinguishing characteristics rule out some more conventional models such as the Kondo effect to explain our data [**89**, **112**] (for example, the Kondo resonances always occur at the zero dc bias).

The model that we believe best explains our data is based on the interference between a path that is directly transmitted an appreciable distance along the MWNT and a path that is transmitted via a resonant state with a well defined energy E_0, the so-called Fano

resonance as described in Sec. 2.2.7. The Fano conductance is decribed by Eqn. 2.93,

$$G_{Fano}(E) = \frac{2e^2}{h} T_d \frac{|2(E - E_0) + q\Gamma|^2}{4(E - E_0)^2 + \Gamma^2}, \tag{4.5}$$

where q is the complex Fano parameter and $\frac{2e^2}{h} T_d \equiv G_d$. The Fano resonance lineshape described by the equation above can explain the structure we see in the differential conductance of our devices: (1) the resonance can occur at finite bias as the energy of the resonant state is not necessarily zero; (2) in the limit $|E - E_0| \gg \Gamma$, the contribution from the resonant state is essentially zero and the conductance goes to $G \sim G_d$, as one would expect off-resonance; and (3) on resonance ($E = E_0$), the conductance can be either a peak or a dip depending on the modulus or phase of the Fano parameter q.

However, in real experiments, phase incoherent transport also takes place, so that one must write [**66**],

$$G_{total} = G_{inc} + G_{Fano}, \tag{4.6}$$

where G_{inc} is the conductance of the incoherent channels that do not interfere with the resonant state. In analyzing the differential conductance of our own devices quantitatively, we have the problem of subtracting the background differential conductance, the part of the differential conductance not associated with the Fano resonance.

To subtract the slowly varying background for Sample C, for example, we use a low pass fast fourier transform (FFT) filter to subtract the background. The technique is as follows. We use a low pass FFT with a cutoff frequency at 30 mV^{-1} for the differential conductance

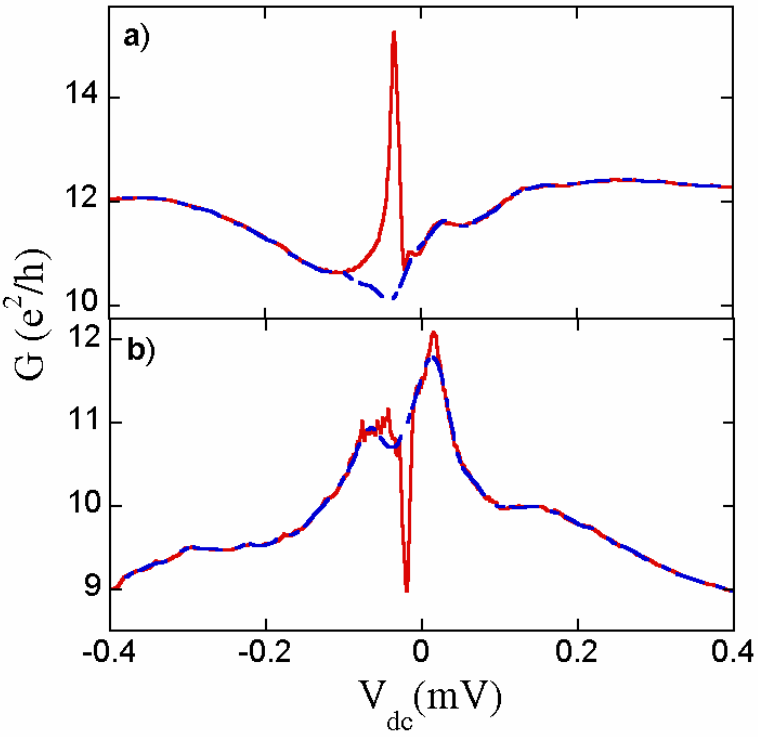

Figure 4.14. (Color) (a) Differential conductance data for Sample C on the first cooldown. Data taken at 20 mK. The dashed line shows the background calculated from the FFT, as described in the text. (b) Similar curves for the conductance dip observed on the second cooldown of Sample C at 16 mK. Adapted from Ref. [**107**].

data outside of the voltage range ([-0.1 mV, -0.02 mV] for conductance peaks and [-0.05 mV, 0.02 mV] for conductance dips) over which the resonance occurs. We then perform a reverse FFT to obtain the background. The result of this process is shown as the dashed lines for the conductance peak and dip, which is represented by the solid lines in Fig. 4.14 for Sample C. The assumption of this numerical process is that the background varies slowly while the feature caused by Fano resonance is very sharp. We believe that the resulting slowly varying background is a better approximation than simply assuming a flat background over the same voltage range.

After this background subtraction, the value of the conductance far off-resonance after the background subtraction process described above would be zero, since we have also subtracted any off-resonance contribution of the direct transmission of the Fano resonance, the contribution corresponding to $G_d = (2e^2/h)T_d$. We do not know for sure the value of T_d as we cannot determine how many channels contribute to transport coherent. However, we believe that the total number of conducting channels is small, and the transport in these channels is highly ballistic. Otherwise, the amplitude of the Fano resonance would be much larger. Since there is only one resonance peak or dip that is prominent, it is a safe to assume that only one resonant state contributes. We assume that two channels interfere coherently with the resonant state, each with a conductance of $2e^2/h$. Consequently, the conductance curve should be offset by $4e^2/h$.

Figure 4.15(a) show the background-subtracted data with an offset of $4e^2/h$ for both the conductance peak and the dip at 20 mK and 16 mK respectively, along with the best fits to the Fano functional form, Eqn. 4.5. For the dip, the modulus of the complex Fano factor

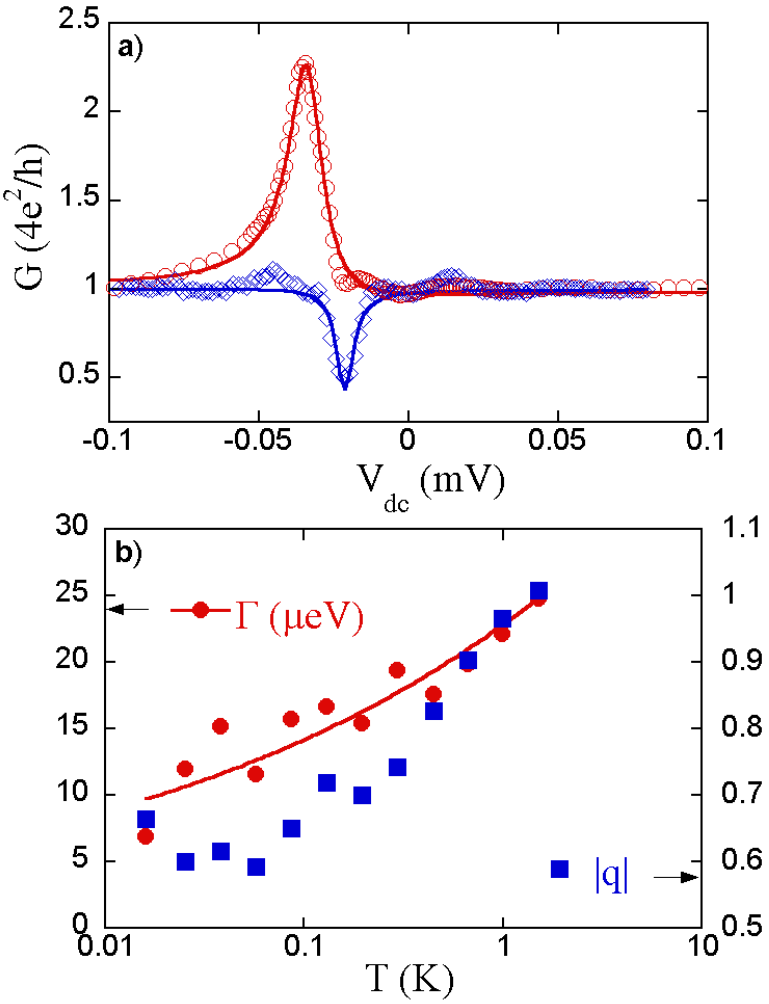

Figure 4.15. (Color) (a) Open symbols; data for the conductance peak and dip of Fig. 4.14 after the subtraction of the backgrounds shown by the dashed curves in Fig. 4.14, with an offset of 4 e^2/h added. Solid lines, fits to the Fano formula, Eqn.(4.14). Fitting parameters for the peak are $|q|$=0.66, θ=1.61 and Γ =6.9 μeV, and $|q|$=1.50, θ=1.69 and Γ =13.6 μeV for the conductance dip. (b) Temperature dependence of the fitting parameters Γ and $|q|$ for the conductance dip of (a). The solid line is a fit to the data, giving $\Gamma = 22.9 \times T^{0.21}$ μeV. Adapted from Ref. [**107**].

is $|q| = 0.65$, while the phase θ of q is nearly $\pi/2$ (1.61). This value for θ corresponds to a phase difference of about $\phi = \pi/2$ (1.507) between the direct and resonant channels.

Figure 4.15(b) shows the fitted values of the modulus of the Fano parameter $|q|$ and the linewidth Γ as a function of temperature for the conductance dip of Fig. 4.15(a). The phase of the Fano parameter θ is essentially a constant at $\pi/2$ (1.58 ± 0.06) over the entire measured temperature range. Γ decreases with decreasing temperature while q first decreases and the saturates at low temperatures. We note that the Fano formula Eqn. 4.5 did not consider the influence of the temperature. One would expect a thermal broadening at finite temperature with the form

$$G(V,T) = \int G_{Fano}(E) \left(-\frac{\partial f(E - eV)}{\partial E} \right) dE, \tag{4.7}$$

where $f(E)$ is the Fermi function. At temperatures $T \gg \Gamma/k_B$, the effective linewidth of the resonance should be approximately 3.5 $k_B T$. At T= 1 K, for example, the effective linewidth should be $\sim$ 300 μeV. However we obtain a much smaller value $\sim$ 22 μeV. Obviously, our attempts to fit our data to the temperature dependent equation, Eqn. 4.7 failed.

We now analyze the origin of the resonant state. The metastable nature of the conductance seen in some of our devices suggests that it might be related to bound states caused by defects or impurities We attempted to locate the locations of the impurities by using different probe configuration and theoretical analysis. However, due to the non-local nature of phase coherent transport, this attempt was not successful.

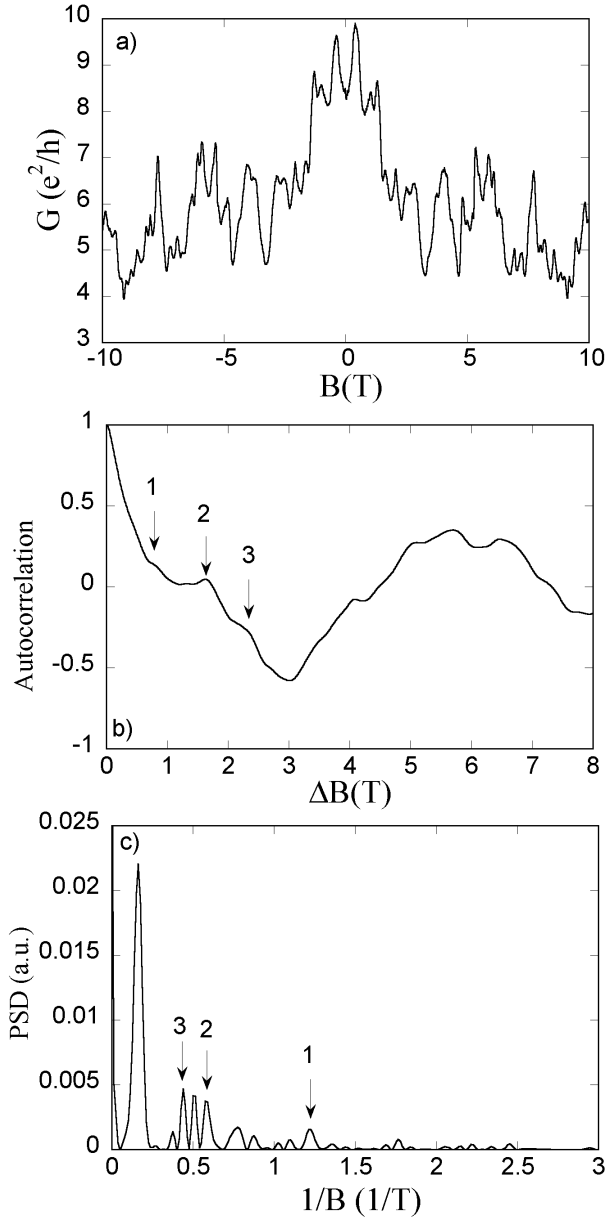

Figure 4.16. (a) Magnetoconductance of Sample C, at 25 mK (reproduction of Fig. 4.13(a)). (b) Autocorrelation function of the data in (a), $< G(B)G(B + \Delta B) > / < G(B)^2 >$, after a sixth-order polynomial background has been subtracted. (c) The PSD of the magnetoconductance data of (a), after a sixth order polynomial background has been subtracted. The arrows in (b) mark the period of magnetoconductance oscillations; the corresponding arrows in (c) mark the frequency. Adapted from Ref. [**107**].

As we noted earlier, quantum interference effects can be modulated by a magnetic field. For Fano resonances, there has been elegant experiment on systems where a quantum dot is embedded in an Aharonov-Bohm interferometer, demonstrating that Fano resonances can be modulated by external magnetic field [**96**]. Although the interference paths in our devices are not as clearly defined as there is no spatial separation between these paths, we tried to understand that the large oscillations in the magnetoconductance observed in our devices by an Aharonov-Bohm modulation of the Fano resonance. As we discussed earlier, the amplitude of the variations in the magnetoconductance is much larger than the amplitude expected from UCF in a diffusive conductor. We also found that superimposed on top of the background fluctuations of the magnetoconductance are periodic oscillations. This can be seen clearly by looking at the autocorrelation functions and the FFTs of the magnetoconductance. Figure 4.16 shows the magnetoconductance, autocorrelation function and power spectral density (PSD) of the magnetoconductance of Sample C whose data have been shown already in Fig. 4.13. A sixth-order polynomial background has been subtracted from the data before performing the autocorrelation and FFTs. Periods corresponds to 0.8 Tesla and its multiples such as 1.6 Tesla and 2.4 Tesla can be clearly seen in the autocorrelation and the PSD. The first three multiples have been marked as "1", "2", and "3" in Figs. 4.16(b)(c). We believe that this period corresponds to a modulation of the phase of the Fano resonance by the magnetic field. For a normal metal wire with the same dimension as our MWNT, the period of 0.8 T corresponds to the penetration of a single normal flux quantum h/e over length scale of approximately 160 nm given an estimated width of 25 nm of the MWNT. This 0.8 T oscillation can be seen in Fig. 4.17. We can see a quasi-oscillation with a field

0.8 T. The shape of $G(V_{dc})$ changes which is to some extent similar to the Fano resonance modulated by magnetic field [**113**].

Fano resonances in CNT devices have been reported by three other groups [**113**–**115**]. Kim *et al.* [**113**] observed a Fano resonance in two of their devices. The authors concluded that the Fano resonances are associated with the presence of a MWNT cross, as they did not observe Fano resonances in the other devices without a MWNT cross. In this paper, however, the mechanism that gave rise to the resonant state was not clear. Yi *et al.* [**114**] measured the conductance of crosses consisting of metal electrodes patterned across MWNT bundles. In two of these devices, they observed a non-monotonic behavior of the conductance near zero bias, which they ascribed to the Fano resonance from interference between a Kondo resonance and non-resonant channels. More recently, Fano resonances have been observed in single-walled nanotubes [**115**]. The authors speculated that the interference might occur between two transport subbands in a single SWCNT, or between transport channels on different SWCNTs in a SWCNT bundle. We note that, in all these experiments, the metastable behavior we observe was not reported. The origin of the resonant states are obscure.

By now, we have established that the sharp features we observed are an interference effect from transmission through a resonant state and direct transmission with the theoretically predicted value expected for a metallic CNT shell of $4e^2/h$. The resonant state is associated with defects or impurities which can change due to thermal annealing or as a function of time. This picture assumes ballistic transport with a conductance of $4e^2/h$. As the ballistic transport in MWNTs seems still controversial as described in Sec. 2.3.2 and 2.3.3, and the setup of our devices seems to resemble more the devices which showed diffusive

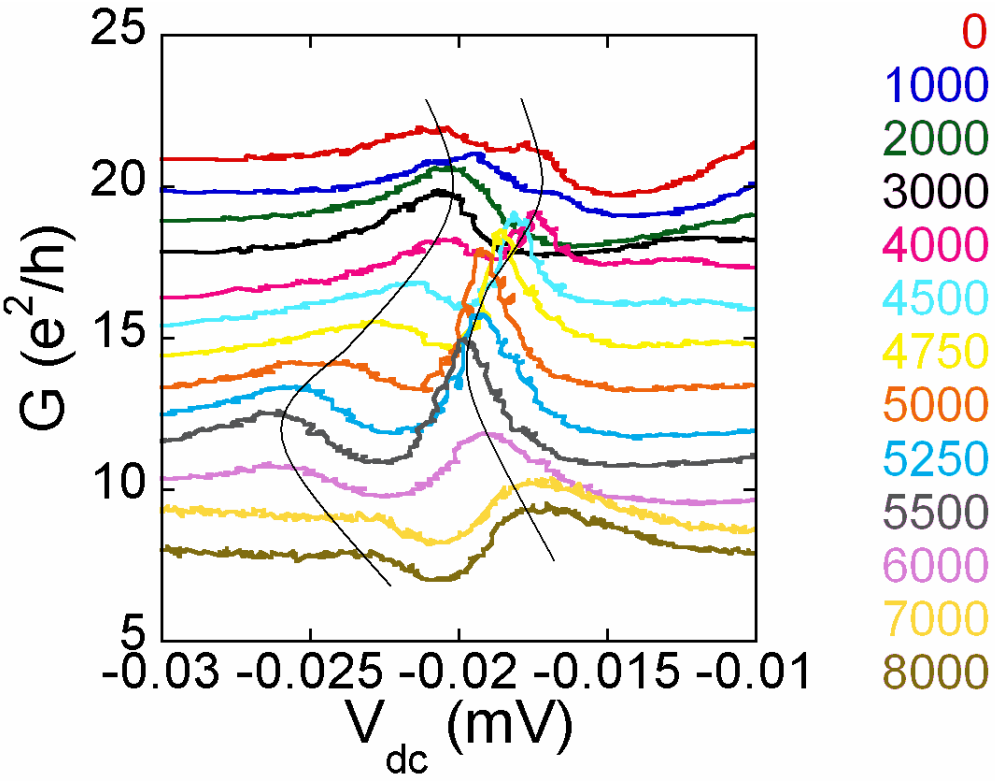

Figure 4.17. (Color) The differential conductance curve of Sample C at 0 (top), 0.1, 0.2, 0.3, 0.4, 0.45, 0.475, 0.5, 0.525, 0.55, 0.6, 0.7, 0.8(bottom) Tesla. The units of the magnetic field in the figure are Gauss. The data (0-0.7 Tesla) are offsetted e^2/h from adjacent data for clarity. The black lines are the guide lines for Aharonov-Bohm oscillations.

transport [**62**, **79**], it is fair to ask that whether this assumption is valid or not and how can we explain this "apparent" discrepancy.

As we know, SWCNT can be metallic or semiconducting depending on chirality as discussed in Sec. 2.1, and MWNT consists multi-shells which individually can be metallic or semiconducting [**76**]. We propose a similar model as in Ref. [**92**]. Our MWNT samples with low contact resistance actually have contacts with more than one shell. The outermost shell is very disordered and the transport is incoherent, which is the background resistance we subtracted in Fig. 4.14. The inside shells are clean and the transport is ballistic. The resonant states can be caused by the probes, from which the electrons can either go to the inside shell directly or go to the outermost shell first, then to the inside shell and and be resonantly transmitted. Alternatively, the electrons in the clean shell can either go to the higher subbands in the same shell and come back, or go to the next shell then come back. This can also result in Fano resonance lineshape as in Ref. [**68**].

This model can also be one of the possible explanations to reconcile that both ballistic and diffusive transport are observed in MWNTs: for the experiments in Refs. [**62**, **79**], the electrodes are patterned on the outside shell of the MWNTs, which has lots of disorders. Therefore diffusive transport was observed. We note that this is similar to our high contact resistance Sample A. For the experiments with different configurations as in Ref. [**47**], the MWNT stuck out from a bundle. Electrical contact could be at the end of the CNT, which could be open and allow connection to an inside shell. The other end is dipped into liquid mercury, which might be able to diffuse into the inner shell. Obviously, further research is needed to support this speculation.

CHAPTER V

Summary and Outlook

5.1. Summary

We have studied the electronic transport behavior of MWNTs. Our multielectrode devices allowed us to make four-terminal measurement of the MWNT and the contact resistances of the device. Because of the multitermianl configuration, we were able to do measurements in a way that is much more informative than the majority of the experiments done by other groups. We developed methods to achieve low contact resistances by using a short time O_2 plasma etch. Some of our MWNTs were cooled down in a dilution refrigerator down to 16 mK, which has been done only by a few other groups [**78**].

The differential conductance of the MWNTs was measured at low temperatures, as a function of the dc bias voltage, temperature and the magnetic field. We found that although the CNT devices we fabricated were nominally the same, their transport properties were quite different. The transport properties showed a distinct evolution as a function of the contact resistance. In our studies, we focused on phenomena not previously observed by other researchers. Sharp features such as a prominent peak or dip were observed in low contact resistance samples at the base temperature of the dilution refrigerator. The key characteristics of these features were the following: (1) the features appeared at non-zero

bias; (2) they had asymmetric lineshapes; (3) the conductance was metastable. These characteristics ruled out other more familiar models such as the Kondo effect. The features are best described as arising from Fano resonances that result from interferences between direct transmission paths and resonant transmission paths. The resonant state was due to impurities. However the locations of these impurities were not known due to non-local effects. We further proposed a model which can account for the origin of the ballistic transport in MWNT as well as a possible explanation for the controversial results obtained by different groups. However, this model needs further testing. Regarding the controversy about whether MWNTs are ballistic conductor or diffusive conductor requires further study. In our experiments, we conclude that the impurities play an important role in the transport properties of the MWNTs. It would be very interesting to actually "see" and locate those impurities. A low temperature STM can be used for this purpose as this technique has been used image the electronic wavefunctions in CNTs [**116**] and charge states in CNT quantum dots [**117**].

There are also many other open questions which have not been studied. For example, what is the mechanism of conduction between shells of the MWNTs? Although there have been some preliminary studies on this subject [**118**], this problem remains largely unexplored. There are also suggestions that transport in MWNTs depends on whether different shells are commensurate or incommensurate [**37**, **38**], leading to MWNTs that are either ballistic or diffusive. Experiments which can relate the atomic structure and electrical properties of MWNTs have yet to be performed.

In this thesis, electron transport in MWNTs was the focus of our research. Interesting quantum effects were shown in our experiments. These quantum effects give some insight into the transport properties of MWNTs. Nevertheless, there is a lot of work that remains to be done. For example, in this thesis, SWCNTs were not systematically studied, and part of the reason is due to our limited access to high quality SWCNTs. As the technology of synthesizing SWCNTs by chemical vapor deposition becomes more accessible, it would be interesting to study electron transport in SWCNTs.

5.2. Outlook of Future Work

The improvement of current experiments discussed in the previous section is a natural evolution of this current research. There are many other interesting topics involving new CNT physics that will be discussed here.

Because of the expected low spin-orbit coupling in CNTs, they are viewed as a potential candidate for spin electronic devices. There have been a number of experimental studies of spin transport in CNTs. Tsukagoshi *et al.* [**119**] fabricated the first spin transport device on a MWNT. Other experiments [**120**, **121**] followed their work in MWNTs. Spin transport in SWCNTs has also been studied very recently [**122**]. In these experiments, however, the data were not clean. This is because it is very difficult to make good contact to CNTs. As we have developed methods to fabricate good contact to MWNTs, we are interested in doing research in spin transport in CNTs. A preliminary device with MWNT connected to ferromagnetic materials Ni is shown in Fig. 5.1(a). The two Ni bars have different switching fields, so the device is a CNT spin valve device. The gold electrodes at the two ends of the

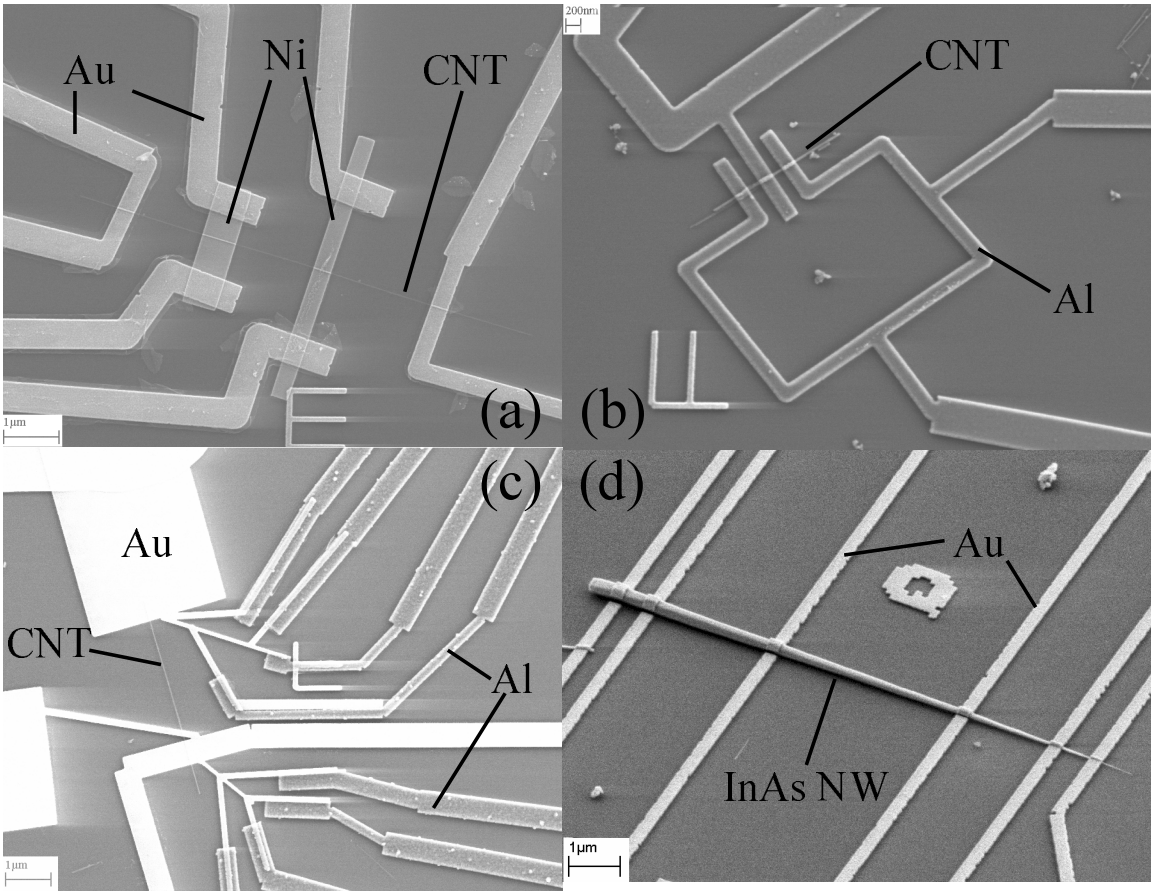

Figure 5.1. (a) A MWNT spin valve device with a long and thin Ni bar and a short and wide Ni bar. (b) A MWNT device with Al electrodes to form SQUID shape device. (c) Device to measure MWNT thermopower. (d) A multiprobe InAs NW device.

CNT enable us to measure the contact resistances. Unfortunately, the data did not show the expected spin valve effects. A possible cause of this failure might due to the fact that our contacts were not perfect.

Connecting superconducting leads to CNTs brings interesting physics. The superconducting proximity effect [**123**] was observed by connecting SWCNTs to superconducting electrodes [**124**]. A supercurrent was also observed by a different group [**125**, **126**] in SWCNT ropes connected to a superconductor. However, no other research groups observed the supercurrent in similar devices until very recently, when Jarillo-Herrero *et al.* [**127**] used a multiple-stage filtering system to suppress electronic noise and observed gate modulated supercurrent in CNT devices. The superconducting proximity effect was also observed in MWNT devices [**128**], although suppercurrent was not observed. The most controversial experiments are intrinsic superconductivity found in SWCNT ropes [**126**, **129**], which was only reproduced by a different group on entirely end-bonded MWNTs very recently [**130**]. We fabricated MWNT devices connecting to an Al loop as shown in Fig. 5.1(b). For phase coherent transport, we expected to see resistance oscillations as a function of magnetic flux inside the loop. However, this oscillation was not observed. We instead observed some hysterical behavior with oscillations [**131**]. This effect is not understood and further study is needed.

The thermopower of CNTs is another interesting subject which is often overlooked by the research community. There are only a few experiments concerning thermopower in CNTs [**132**–**135**]. The author has fabricated devices to measure CNT thermopower as shown in Fig. 5.1(c). Our measured value was comparable to that measured earlier [**132**].

We observed interesting oscillations as a function of a magnetic field along the tube axis. The technique of the thermopower measurement can be found in Ref. [**99**].

Beside CNTs, there are other interesting nanomaterials such as inorganic nanotubes (NTs) and semiconductor nanowires (NWs). The most well characterized inorganic NT is boron nitride NT. It is a close analog to CNTs, but unlike CNTs which can be either metallic or semiconducting, boron nitride NTs are wide gap semiconductors (E_g=5.5 eV), independent of the diameter. They are more like insulators. Boron nitride NTs were proposed to be put inside or outside carbon nanotubes for insulation.

Semiconductor NWs can be synthesized as a single crystal. The chemical composition, diameter and length can be well controlled. In fact, they are one of the best controlled class of nanoscale building blocks. Semiconductor NWs have been assembled as nanoscale FETs [**136**, **137**], p-n diodes [**136**, **138**], light emitting diodes [**136**], bipolar junction transistors [**138**], complementary inverters [**138**], complex logic gates, or other basic computation circuits [**139**]. However, the synthesis of NWs and the integration with other current elements remains a challenge for nanoelectronics. The author has fabricated and done preliminary measurements on InAs NWs. The InAs NWs were synthesized in Prof. Lauhon's group [**140**]. Figure 5.1(d) shows an InAs device fabricated by the author.

In conclusion, the discovery of CNTs marked a milestone in nanoscience and technology. CNTs are important and interesting both due to their great potential for nanoscale applications and because they offered a testing stage to study fundamental physics in low dimensions. Other nanomaterials such as NWs also have begun to show their potential and have become a hot research area in recent years. With so many novel materials and rich

physics, this field has attracted a lot of scientific interests. We believe this fast developing trend will continue for the next a few years or even next decade.

References

[1] Intel. Intel EUV lithography program enters development phase. http://www.intel.com/technology/silicon/si08041.htm, 2006.

[2] P. Rai-Choudhury. *Handbook of microlithography, micromaching and microfabrication.* SPIE Optical Engineering Press, Bellingham, Wa., 1997.

[3] S. Y. Chou, P. R. Krauss, and P. J. Renstrom. Imprint lithography with 25-nanometer resolution. *Science*, 272(5258):85–87, 1996.

[4] R.P. Feynman. There's plenty of room at the bottom, 1959.

[5] H. Park, J. Park, A. K. L. Lim, E. H. Anderson, A. P. Alivisatos, and P. L. McEuen. Nanomechanical oscillations in a single-C-60 transistor. *Nature*, 407(6800):57–60, 2000.

[6] J. Park, A. N. Pasupathy, J. I. Goldsmith, C. Chang, Y. Yaish, J. R. Petta, M. Rinkoski, J. P. Sethna, H. D. Abruna, P. L. McEuen, and D. C. Ralph. Coulomb blockade and the Kondo effect in single-atom transistors. *Nature*, 417(6890):722–725, 2002.

[7] W. J. Liang, M. P. Shores, M. Bockrath, J. R. Long, and H. Park. Kondo resonance in a single-molecule transistor. *Nature*, 417(6890):725–729, 2002.

[8] S. W. Chung, D. S. Ginger, M. W. Morales, Z. F. Zhang, V. Chandrasekhar, M. A. Ratner, and C. A. Mirkin. Top-down meets bottom-up: Dip-pen nanolithography and DNA-directed assembly of nanoscale electrical circuits. *Small*, 1(1):64–69, 2005.

[9] R. H. Baughman, A. A. Zakhidov, and W. A. de Heer. Carbon nanotubes - the route toward applications. *Science*, 297(5582):787–792, 2002.

[10] B. Q. Wei, R. Vajtai, and P. M. Ajayan. Reliability and current carrying capacity of carbon nanotubes. *Appl. Phys. Lett.*, 79(8):1172–1174, 2001.

[11] C. T. White and T. N. Todorov. Carbon nanotubes as long ballistic conductors. *Nature*, 393(6682):240–242, 1998.

[12] T. Durkop, S. A. Getty, E. Cobas, and M. S. Fuhrer. Extraordinary mobility in semiconducting carbon nanotubes. *Nano Lett.*, 4(1):35–39, 2004.

[13] M. M. J. Treacy, T. W. Ebbesen, and J. M. Gibson. Exceptionally high Young's modulus observed for individual carbon nanotubes. *Nature*, 381(6584):678–680, 1996.

[14] S. Berber, Y. K. Kwon, and D. Tomanek. Unusually high thermal conductivity of carbon nanotubes. *Phys. Rev. Lett.*, 84(20):4613–4616, 2000.

[15] R. Martel, T. Schmidt, H. R. Shea, T. Hertel, and P. Avouris. Single- and multi-wall carbon nanotube field-effect transistors. *Appl. Phys. Lett.*, 73(17):2447–2449, 1998.

[16] J. Appenzeller, J. Knoch, V. Derycke, R. Martel, S. Wind, and P. Avouris. Field-modulated carrier transport in carbon nanotube transistors. *Phys. Rev. Lett.*, 89(12):126801, 2002.

[17] S. Heinze, J. Tersoff, R. Martel, V. Derycke, J. Appenzeller, and P. Avouris. Carbon nanotubes as Schottky barrier transistors. *Phys. Rev. Lett.*, 89(10):106801, 2002.

[18] A. Javey, J. Guo, Q. Wang, M. Lundstrom, and H. J. Dai. Ballistic carbon nanotube field-effect transistors. *Nature*, 424(6949):654–657, 2003.

[19] J. U. Lee, P. P. Gipp, and C. M. Heller. Carbon nanotube p-n junction diodes. *Appl. Phys. Lett.*, 85(1):145–147, 2004.

[20] A. Bachtold, P. Hadley, T. Nakanishi, and C. Dekker. Logic circuits with carbon nanotube transistors. *Science*, 294(5545):1317–1320, 2001.

[21] V. Derycke, R. Martel, J. Appenzeller, and P. Avouris. Carbon nanotube inter- and intramolecular logic gates. *Nano Lett.*, 1(9):453–456, 2001.

[22] J. B. Cui, R. Sordan, M. Burghard, and K. Kern. Carbon nanotube memory devices of high charge storage stability. *Appl. Phys. Lett.*, 81(17):3260–3262, 2002.

[23] Z. H. Chen, J. Appenzeller, Y. M. Lin, J. Sippel-Oakley, A. G. Rinzler, J. Y. Tang, S. J. Wind, P. M. Solomon, and P. Avouris. An integrated logic circuit assembled on a single carbon nanotube. *Science*, 311(5768):1735–1735, 2006.

[24] Neil W. Ashcroft and N. David Mermin. *Solid state physics*. Holt Rinehart and Winston, New York,, 1976.

[25] C. Kane, L. Balents, and M. P. A. Fisher. Coulomb interactions and mesoscopic effects in carbon nanotubes. *Phys. Rev. Lett.*, 79(25):5086–5089, 1997.

[26] R. Saito, G. Dresselhaus, and M. S. Dresselhaus. *Physical properties of carbon nanotubes*. Imperial College Press, London, 1998.

[27] S. Reich, C. Thomsen, and J. Maultzsch. *Carbon nanotubes : basic concepts and physical properties*. Wiley-VCH, Weinheim ; Cambridge, 2004.

[28] M. Ouyang, J. L. Huang, and C. M. Lieber. Scanning tunneling microscopy studies of the one-dimensional electronic properties of single-walled carbon nanotubes. *Annu. Rev. Phys. Chem.*, 53:201–220, 2002.

[29] J. W. Mintmire and C. T. White. Universal density of states for carbon nanotubes. *Phys. Rev. Lett.*, 81(12):2506–2509, 1998.

[30] R. A. Jishi, D. Inomata, K. Nakao, M. S. Dresselhaus, and G. Dresselhaus. Electronic and lattice properties of carbon nanotubes. *J. Phys. Soc. Jpn.*, 63(6):2252–2260, 1994.

[31] N. Hamada, S. Sawada, and A. Oshiyama. New one-dimensional conductors - graphitic microtubules. *Phys. Rev. Lett.*, 68(10):1579–1581, 1992.

[32] C. L. Kane and E. J. Mele. Size, shape, and low energy electronic structure of carbon nanotubes. *Phys. Rev. Lett.*, 78(10):1932–1935, 1997.

[33] A. Kleiner and S. Eggert. Curvature, hybridization, and STM images of carbon nanotubes. *Phys. Rev. B*, 6411(11):113402, 2001.

[34] P. Delaney, H. J. Choi, J. Ihm, S. G. Louie, and M. L. Cohen. Broken symmetry and pseudogaps in ropes of carbon nanotubes. *Nature*, 391(6666):466–468, 1998.

[35] P. Delaney, H. J. Choi, J. Ihm, S. G. Louie, and M. L. Cohen. Broken symmetry and pseudogaps in ropes of carbon nanotubes. *Phys. Rev. B*, 60(11):7899–7904, 1999.

[36] R. Saito, G. Dresselhaus, and M. S. Dresselhaus. Electronic-structure of double-layer graphene tubules. *J. Appl. Phys.*, 73(2):494–500, 1993.

[37] K. H. Ahn, Y. H. Kim, J. Wiersig, and K. J. Chang. Spectral correlation in incommensurate multiwalled carbon nanotubes. *Phys. Rev. Lett.*, 90(2):026601, 2003.

[38] S. Roche, F. Triozon, A. Rubio, and D. Mayou. Conduction mechanisms and magnetotransport in multiwalled carbon nanotubes. *Phys. Rev. B*, 6412(12):121401, 2001.

[39] P. A. Lee and A. D. Stone. Universal conductance fluctuations in metals. *Phys. Rev. Lett.*, 55(15):1622–1625, 1985.

[40] S. Washburn and R. A. Webb. Aharonov-Bohm effect in normal metal quantum coherence and transport. *Adv. Phys.*, 35(4):375–422, 1986.

[41] E. Abrahams, P. W. Anderson, D. C. Licciardello, and T. V. Ramakrishnan. Scaling theory of localization - absence of quantum diffusion in 2 dimensions. *Phys. Rev. Lett.*, 42(10):673–676, 1979.

[42] B. J. Vanwees, H. Vanhouten, C. W. J. Beenakker, J. G. Williamson, L. P. Kouwenhoven, D. Vandermarel, and C. T. Foxon. Quantized conductance of point contacts in a two-dimensional electron-gas. *Phys. Rev. Lett.*, 60(9):848–850, 1988.

[43] C. L. Kane and M. P. A. Fisher. Transport in a one-channel Luttinger liquid. *Phys. Rev. Lett.*, 68(8):1220–1223, 1992.

[44] A. M. Chang, L. N. Pfeiffer, and K. W. West. Observation of chiral Luttinger behavior in electron tunneling into fractional quantum hall edges. *Phys. Rev. Lett.*, 77(12):2538–2541, 1996.

[45] M. A. Kastner. Artificial atoms. *Phys. Today*, 46(1):24–31, 1993.

[46] Supriyo Datta. *Electronic transport in mesoscopic systems*. Cambridge studies in semiconductor physics and microelectronic engineering ; 3. Cambridge University Press, Cambridge ; New York, 1995.

[47] S. Frank, P. Poncharal, Z. L. Wang, and W. A. de Heer. Carbon nanotube quantum resistors. *Science*, 280(5370):1744–1746, 1998.

[48] Yoseph Imry and ebrary Inc. *Introduction to mesoscopic physics*. Mesoscopic physics and nanotechnology. Oxford University Press, New York, 1997.

[49] David K. Ferry and Stephen M. Goodnick. *Transport in nanostructures*. Cambridge studies in semiconductor physics and microelectronic engineering ; 6. Cambridge University Press, Cambridge, U.K. ; New York, 1997.

[50] M. Buttiker. 4-terminal phase-coherent conductance. *Phys. Rev. Lett.*, 57(14):1761–1764, 1986.

[51] A. D. Benoit, S. Washburn, C. P. Umbach, R. B. Laibowitz, and R. A. Webb. Asymmetry in the magnetoconductance of metal wires and loops. *Phys. Rev. Lett.*, 57(14):1765–1768, 1986.

[52] Yuri Galperin. Quantum transport: Lecture notes, 1998.

[53] Johannes Voit. A brief introduction to Luttinger liquids, 2000.

[54] Tsuneya Ando. *Mesoscopic physics and electronics*. Nanoscience and technology. Springer, Berlin ; New York, 1998.

[55] D. L. Maslov and M. Stone. Landauer conductance of Luttinger liquids with leads. *Phys. Rev. B*, 52(8):R5539–R5542, 1995.

[56] Rolf Haug and Herbert Schoeller. Interacting electrons in nanostructures, 2001.

[57] M. Bockrath, D. H. Cobden, J. Lu, A. G. Rinzler, R. E. Smalley, T. Balents, and P. L. McEuen. Luttinger-liquid behaviour in carbon nanotubes. *Nature*, 397(6720):598–601, 1999.

[58] Z. Yao, H. W. C. Postma, L. Balents, and C. Dekker. Carbon nanotube intramolecular junctions. *Nature*, 402(6759):273–276, 1999.

[59] C. W. J. Beenakker and H. Vanhouten. Quantum transport in semiconductor nanostructures. *Solid State Phys.-Adv. Res. Appl.*, 44:1–228, 1991.

[60] B. L. Altshuler and A. G. Aronov. Magnetoresistance of thin-films and of wires in a longitudinal magnetic-field. *Jetp Lett.*, 33(10):499–501, 1981.

[61] R. A. Webb and S. Washburn. Quantum interference fluctuations in disordered metals. *Phys. Today*, 41(12):46–53, 1988.

[62] C. Schonenberger, A. Bachtold, C. Strunk, J. P. Salvetat, and L. Forro. Interference and interaction in multi-wall carbon nanotubes. *Appl. Phys. A-Mater. Sci. Process.*, 69(3):283–295, 1999.

[63] Hermann Grabert, Michel H. Devoret, and North Atlantic Treaty Organization. Scientific Affairs Division. *Single charge tunneling : Coulomb blockade phenomena in nanostructures*. NATO ASI series. Series B, Physics ; v. 294. Plenum Press, New York, 1992.

[64] R. Egger and A. O. Gogolin. Bulk and boundary zero-bias anomaly in multiwall carbon nanotubes. *Phys. Rev. Lett.*, 8706(6):066401, 2001.

[65] U. Fano. Effects of configuration interaction on intensities and phase shifts. *Phys. Rev.*, 1(6):1866–1878, 1961.

[66] J. Gores, D. Goldhaber-Gordon, S. Heemeyer, M. A. Kastner, H. Shtrikman, D. Mahalu, and U. Meirav. Fano resonances in electronic transport through a single-electron transistor. *Phys. Rev. B*, 62(3):2188–2194, 2000.

[67] L. D. Landau and E. M. Lifshits. *Quantum mechanics : non-relativistic theory*. Course of theoretical physics ; v. 3. Pergamon Press, Oxford ; New York, 3d , rev. and enl. / edition, 1977.

[68] J. U. Nockel and A. D. Stone. Resonance line-shapes in quasi-one-dimensional scattering. *Phys. Rev. B*, 50(23):17415–17432, 1994.

[69] A. A. Clerk, X. Waintal, and P. W. Brouwer. Fano resonances as a probe of phase coherence in quantum dots. *Phys. Rev. Lett.*, 86(20):4636–4639, 2001.

[70] J. W. G. Wildoer, L. C. Venema, A. G. Rinzler, R. E. Smalley, and C. Dekker. Electronic structure of atomically resolved carbon nanotubes. *Nature*, 391(6662):59–62, 1998.

[71] T. W. Odom, J. L. Huang, P. Kim, and C. M. Lieber. Atomic structure and electronic properties of single-walled carbon nanotubes. *Nature*, 391(6662):62–64, 1998.

[72] M. Ouyang, J. L. Huang, C. L. Cheung, and C. M. Lieber. Energy gaps in "metallic" single-walled carbon nanotubes. *Science*, 292(5517):702–705, 2001.

[73] S. J. Tans, M. H. Devoret, H. J. Dai, A. Thess, R. E. Smalley, L. J. Geerligs, and C. Dekker. Individual single-wall carbon nanotubes as quantum wires. *Nature*, 386(6624):474–477, 1997.

[74] S. J. Tans, A. R. M. Verschueren, and C. Dekker. Room-temperature transistor based on a single carbon nanotube. *Nature*, 393(6680):49–52, 1998.

[75] C. W. Zhou, J. Kong, and H. J. Dai. Intrinsic electrical properties of individual single-walled carbon nanotubes with small band gaps. *Phys. Rev. Lett.*, 84(24):5604–5607, 2000.

[76] P. C. Collins, M. S. Arnold, and P. Avouris. Engineering carbon nanotubes and nanotube circuits using electrical breakdown. *Science*, 292(5517):706–709, 2001.

[77] M. Bockrath, D. H. Cobden, P. L. McEuen, N. G. Chopra, A. Zettl, A. Thess, and R. E. Smalley. Single-electron transport in ropes of carbon nanotubes. *Science*, 275(5308):1922–1925, 1997.

[78] L. Langer, V. Bayot, E. Grivei, J. P. Issi, J. P. Heremans, C. H. Olk, L. Stockman, C. VanHaesendonck, and Y. Bruynseraede. Quantum transport in a multiwalled carbon nanotube. *Phys. Rev. Lett.*, 76(3):479–482, 1996.

[79] A. Bachtold, C. Strunk, J. P. Salvetat, J. M. Bonard, L. Forro, T. Nussbaumer, and C. Schonenberger. Aharonov-Bohm oscillations in carbon nanotubes. *Nature*, 397(6721):673–675, 1999.

[80] A. Urbina, I. Echeverria, A. Perez-Garrido, A. Diaz-Sanchez, and J. Abellan. Quantum conductance steps in solutions of multiwalled carbon nanotubes. *Phys. Rev. Lett.*, 90(10):106603, 2003.

[81] A. Bachtold, M. S. Fuhrer, S. Plyasunov, M. Forero, E. H. Anderson, A. Zettl, and P. L. McEuen. Scanned probe microscopy of electronic transport in carbon nanotubes. *Phys. Rev. Lett.*, 84(26):6082–6085, 2000.

[82] J. Kong, E. Yenilmez, T. W. Tombler, W. Kim, H. J. Dai, R. B. Laughlin, L. Liu, C. S. Jayanthi, and S. Y. Wu. Quantum interference and ballistic transmission in nanotube electron waveguides. *Phys. Rev. Lett.*, 8710(10):art. no.–106801, 2001.

[83] P. L. McEuen, M. Bockrath, D. H. Cobden, Y. G. Yoon, and S. G. Louie. Disorder, pseudospins, and backscattering in carbon nanotubes. *Phys. Rev. Lett.*, 83(24):5098–5101, 1999.

[84] H. J. Li, W. G. Lu, J. J. Li, X. D. Bai, and C. Z. Gu. Multichannel ballistic transport in multiwall carbon nanotubes. *Phys. Rev. Lett.*, 95(8):086601, 2005.

[85] Y. Aharonov and D. Bohm. Significance of electromagnetic potentials in the quantum theory. 115(3):485–491, 1959.

[86] B. L. Altshuler, A. G. Aronov, and B. Z. Spivak. The Aaronov-Bohm effect in disordered conductors. *Jetp Lett.*, 33(2):94–97, 1981.

[87] B. Stojetz, C. Hagen, C. Hendlmeier, E. Ljubovic, L. Forro, and C. Strunk. Ensemble averaging of conductance fluctuations in multiwall carbon nanotubes. *New J. Phys.*, 6:27, 2004.

[88] B. Stojetz, C. Miko, L. Forro, and C. Strunk. Effect of band structure on quantum interference in multiwall carbon nanotubes. *Phys. Rev. Lett.*, 94(18):186802, 2005.

[89] J. Nygard, D. H. Cobden, and P. E. Lindelof. Kondo physics in carbon nanotubes. *Nature*, 408(6810):342–346, 2000.

[90] W. J. Liang, M. Bockrath, and H. Park. Shell filling and exchange coupling in metallic single-walled carbon nanotubes. *Phys. Rev. Lett.*, 88(12):126801, 2002.

[91] W. J. Liang, M. Bockrath, D. Bozovic, J. H. Hafner, M. Tinkham, and H. Park. Fabry-Perot interference in a nanotube electron waveguide. *Nature*, 411(6838):665–669, 2001.

[92] M. R. Buitelaar, A. Bachtold, T. Nussbaumer, M. Iqbal, and C. Schonenberger. Multiwall carbon nanotubes as quantum dots. *Phys. Rev. Lett.*, 88(15):156801, 2002.

[93] A. Bachtold, M. de Jonge, K. Grove-Rasmussen, P. L. McEuen, M. Buitelaar, and C. Schonenberger. Suppression of tunneling into multiwall carbon nanotubes. *Phys. Rev. Lett.*, 8716(16):166801, 2001.

[94] R. Tarkiainen, M. Ahlskog, J. Penttila, L. Roschier, P. Hakonen, M. Paalanen, and E. Sonin. Multiwalled carbon nanotube: Luttinger versus Fermi liquid. *Phys. Rev. B*, 64(19):art. no.–195412, 2001.

[95] I. G. Zacharia, D. Goldhaber-Gordon, G. Granger, M. A. Kastner, Y. B. Khavin, H. Shtrikman, D. Mahalu, and U. Meirav. Temperature dependence of Fano line shapes in a weakly coupled single-electron transistor. *Phys. Rev. B*, 6415(15):155311, 2001.

[96] K. Kobayashi, H. Aikawa, S. Katsumoto, and Y. Iye. Tuning of the Fano effect through a quantum dot in an Aharonov-Bohm interferometer. *Phys. Rev. Lett.*, 88(25):256806, 2002.

[97] K. Kobayashi, H. Aikawa, S. Katsumoto, and Y. Iye. Mesoscopic Fano effect in a quantum dot embedded in an Aharonov-Bohm ring. *Phys. Rev. B*, 68(23):235304, 2003.

[98] K. Kobayashi, H. Aikawa, A. Sano, S. Katsumoto, and Y. Iye. Fano resonance in a quantum wire with a side-coupled quantum dot. *Phys. Rev. B*, 70(3):035319, 2004.

[99] Zhigang Jiang. *Thermal transport near the normal-metal/superconductor interface in mesoscopic devices*. PhD thesis, Northwestern University, 2005.

[100] Chen-Jung Chien. *Transport phenomena near the normal-metal/superconducting interface in mesoscopic devices*. PhD thesis, Northwestern University, 1998.

[101] Josè Aumentado. *Nonequilibrium and quantum transport phenomena in mesoscopic ferromagnet/superconductor heterostructures*. PhD thesis, Northwestern University, 2000.

[102] S. P. Doherty and R. P. H. Chang. Synthesis of multiwalled carbon nanotubes from carbon black. *Appl. Phys. Lett.*, 81(13):2466–2468, 2002.

[103] R. Tarkiainen, M. Ahlskog, A. Zyuzin, P. Hakonen, and M. Paalanen. Transport in strongly disordered multiwalled carbon nanotubes. *Phys. Rev. B*, 69(3):033402, 2004.

[104] Jonghwa Eom. *Electrical properties of mesoscopic spin glasses*. PhD thesis, Northwestern University, 1998.

[105] Michael P. Marder. *Condensed matter physics*. John Wiley, New York, 2000.

[106] Z. Zhang, D. A. Dikin, R. S. Ruoff, and V. Chandrasekhar. Conduction in carbon nanotubes through metastable resonant states. *Europhys. Lett.*, 68(5):713–719, 2004.

[107] Z. F. Zhang and V. Chandrasekhar. Signatures of phase coherence in the low-temperature transport properties of multiwall carbon nanotubes. *Phys. Rev. B*, 73(7):075421, 2006.

[108] Hiroshi Kamimura and Hideo Aoki. *The physics of interacting electrons in disordered systems*. The International series of monographs on physics ; no. 76. Clarendon Press ; Oxford University Press, Oxford New York, 1989.

[109] M. S. Fuhrer, J. Nygard, L. Shih, M. Forero, Y. G. Yoon, M. S. C. Mazzoni, H. J. Choi, J. Ihm, S. G. Louie, A. Zettl, and P. L. McEuen. Crossed nanotube junctions. *Science*, 288(5465):494–497, 2000.

[110] S. C. Feng, P. A. Lee, and A. D. Stone. Sensitivity of the conductance of a disordered metal to the motion of a single atom - implications for 1/f noise. *Phys. Rev. Lett.*, 56(18):1960–1963, 1986.

[111] N. O. Birge, B. Golding, and W. H. Haemmerle. Conductance fluctuations and 1/f noise in Bi. *Phys. Rev. B*, 42(5):2735–2743, 1990.

[112] J. Kondo. Resistance minimum in dilute magnetic alloys. *Prog. Theor. Phys.*, 32(1):37–49, 1964.

[113] J. Kim, J. R. Kim, J. O. Lee, J. W. Park, H. M. So, N. Kim, K. Kang, K. H. Yoo, and J. J. Kim. Fano resonance in crossed carbon nanotubes. *Phys. Rev. Lett.*, 90(16):166403, 2003.

[114] W. Yi, L. Lu, H. Hu, Z. W. Pan, and S. S. Xie. Tunneling into multiwalled carbon nanotubes: Coulomb blockade and the Fano resonance. *Phys. Rev. Lett.*, 91(7):076801, 2003.

[115] B. Babic and C. Schonenberger. Observation of Fano resonances in single-wall carbon nanotubes. *Phys. Rev. B*, 70(19):195408, 2004.

[116] S. G. Lemay, J. W. Janssen, M. van den Hout, M. Mooij, M. J. Bronikowski, P. A. Willis, R. E. Smalley, L. P. Kouwenhoven, and C. Dekker. Two-dimensional imaging of electronic wavefunctions in carbon nanotubes. *Nature*, 412(6847):617–620, 2001.

[117] M. T. Woodside and P. L. McEuen. Scanned probe imaging of single-electron charge states in nanotube quantum dots. *Science*, 296(5570):1098–1101, 2002.

[118] B. Bourlon, C. Miko, L. Forro, D. C. Glattli, and A. Bachtold. Determination of the intershell conductance in multiwalled carbon nanotubes. *Phys. Rev. Lett.*, 93(17):176806, 2004.

[119] K. Tsukagoshi, B. W. Alphenaar, and H. Ago. Coherent transport of electron spin in a ferromagnetically contacted carbon nanotube. *Nature*, 401(6753):572–574, 1999.

[120] S. Chakraborty, K. M. Walsh, B. W. Alphenaar, L. Liu, and K. Tsukagoshi. Temperature-mediated switching of magnetoresistance in Co-contacted multiwall carbon nanotubes. *Appl. Phys. Lett.*, 83(5):1008–1010, 2003.

[121] S. Sahoo, T. Kontos, C. Schonenberger, and C. Surgers. Electrical spin injection in multiwall carbon nanotubes with transparent ferromagnetic contacts. *Appl. Phys. Lett.*, 86(11):112109, 2005.

[122] B. Nagabhirava, T. Bansal, G. U. Sumanasekera, B. W. Alphenaar, and L. Liu. Gated spin transport through an individual single wall carbon nanotube. *Appl. Phys. Lett.*, 88(2):023503, 2006.

[123] Michael Tinkham. *Introduction to superconductivity*. International series in pure and applied physics. McGraw Hill, New York, 2nd edition, 1996.

[124] A. F. Morpurgo, J. Kong, C. M. Marcus, and H. Dai. Gate-controlled superconducting proximity effect in carbon nanotubes. *Science*, 286(5438):263–265, 1999.

[125] A. Y. Kasumov, R. Deblock, M. Kociak, B. Reulet, H. Bouchiat, II Khodos, Y. B. Gorbatov, V. T. Volkov, C. Journet, and M. Burghard. Supercurrents through single-walled carbon nanotubes. *Science*, 284(5419):1508–1511, 1999.

[126] A. Kasumov, M. Kociak, M. Ferrier, R. Deblock, S. Gueron, B. Reulet, I. Khodos, O. Stephan, and H. Bouchiat. Quantum transport through carbon nanotubes: Proximity-induced and intrinsic superconductivity. *Phys. Rev. B*, 68(21):214521, 2003.

[127] P. Jarillo-Herrero, J. A. van Dam, and L. P. Kouwenhoven. Quantum supercurrent transistors in carbon nanotubes. *Nature*, 439(7079):953–956, 2006.

[128] M. R. Buitelaar, T. Nussbaumer, and C. Schonenberger. Quantum dot in the Kondo regime coupled to superconductors. *Phys. Rev. Lett.*, 89(25):256801, 2002.

[129] M. Kociak, A. Y. Kasumov, S. Gueron, B. Reulet, II Khodos, Y. B. Gorbatov, V. T. Volkov, L. Vaccarini, and H. Bouchiat. Superconductivity in ropes of single-walled carbon nanotubes. *Phys. Rev. Lett.*, 86(11):2416–2419, 2001.

[130] I. Takesue, J. Haruyama, N. Kobayashi, S. Chiashi, S. Maruyama, T. Sugai, and H. Shinohara. Superconductivity in entirely end-bonded multiwalled carbon nanotubes. *Phys. Rev. Lett.*, 96(5):057001, 2006.

[131] Z. Zhang and V. Chandrasekhar. unpublished.

[132] P. Kim, L. Shi, A. Majumdar, and P. L. McEuen. Thermal transport measurements of individual multiwalled nanotubes. *Phys. Rev. Lett.*, 8721(21):215502, 2001.

[133] J. P. Small, K. M. Perez, and P. Kim. Modulation of thermoelectric power of individual carbon nanotubes. *Phys. Rev. Lett.*, 91(25):256801, 2003.

[134] M. C. Llaguno, J. E. Fischer, A. T. Johnson, and J. Hone. Observation of thermopower oscillations in the Coulomb blockade regime in a semiconducting carbon nanotube. *Nano Lett.*, 4(1):45–49, 2004.

[135] C. H. Yu, L. Shi, Z. Yao, D. Y. Li, and A. Majumdar. Thermal conductance and thermopower of an individual single-wall carbon nanotube. *Nano Lett.*, 5(9):1842–1846, 2005.

[136] X. F. Duan, Y. Huang, Y. Cui, J. F. Wang, and C. M. Lieber. Indium phosphide nanowires as building blocks for nanoscale electronic and optoelectronic devices. *Nature*, 409(6816):66–69, 2001.

[137] Y. Cui, Z. H. Zhong, D. L. Wang, W. U. Wang, and C. M. Lieber. High performance silicon nanowire field effect transistors. *Nano Lett.*, 3(2):149–152, 2003.

[138] Y. Cui and C. M. Lieber. Functional nanoscale electronic devices assembled using silicon nanowire building blocks. *Science*, 291(5505):851–853, 2001.

[139] Y. Huang, X. F. Duan, Y. Cui, L. J. Lauhon, K. H. Kim, and C. M. Lieber. Logic gates and computation from assembled nanowire building blocks. *Science*, 294(5545):1313–1317, 2001.

[140] S. J. May, J. G. Zheng, B. W. Wessels, and L. J. Lauhon. Dendritic nanowire growth mediated by a self-assembled catalyst. *Adv. Mater.*, 17(5):598–602, 2005.

[141] S. M. Huang, X. Y. Cai, and J. Liu. Growth of millimeter-long and horizontally aligned single-walled carbon nanotubes on flat substrates. *J. Am. Chem. Soc.*, 125(19):5636–5637, 2003.

[142] T. Brintlinger, Y. F. Chen, T. Durkop, E. Cobas, M. S. Fuhrer, J. D. Barry, and J. Melngailis. Rapid imaging of nanotubes on insulating substrates. *Appl. Phys. Lett.*, 81(13):2454–2456, 2002.

APPENDIX A

Measurement of Single-Walled Carbon Nanotubes

In this chapter, our fabrication and measurment techniques and preliminary results of SWCNT devices will be shown here.

We have had access to a limited number of SWCNT samples from Duke University[1]. The synthesis method can be found in Ref. [**141**]. The samples were long SWCNTs on highly doped (p^{++}) Si substrate with 1 μm thick oxide layer, as schematically shown in Fig. A.1(a). Because the SWCNTs are randomly distributed on the substrate, maximum flexibility is needed for patterning. Therefore e-beam lithography is used in all the lithography steps. Coarse and fine alignment marks are patterned by e-beam lithography as in Fig. A.1(b). The fine alignment marks are numbered. The diameter of SWCNTs is only one or a few nanometers, which is beyond the resolution of most SEM. But due to charging effects, at low acceleration voltages, it is possible to image SWCNTs on an insulating substrate [**142**]. By SEM inspection, we can locate the SWCNTs and map out their coordinates as in Fig. A.1(c). The connecting electrodes and wirebonding pads are then patterned according to the alignment marks defined in the previous step. The completed device is shown schematically in Fig. A.1(d) with a real device shown in Fig. A.2.

The SWCNT devices we fabricated have a resistance on the order of MΩ as they are exceptionally long. For these high resistance samples, it is difficult or impossible to use the

[1]Obtained from research group of Prof. Jie Liu. Dr. Shaoming Huang synthesized the SWCNTs.

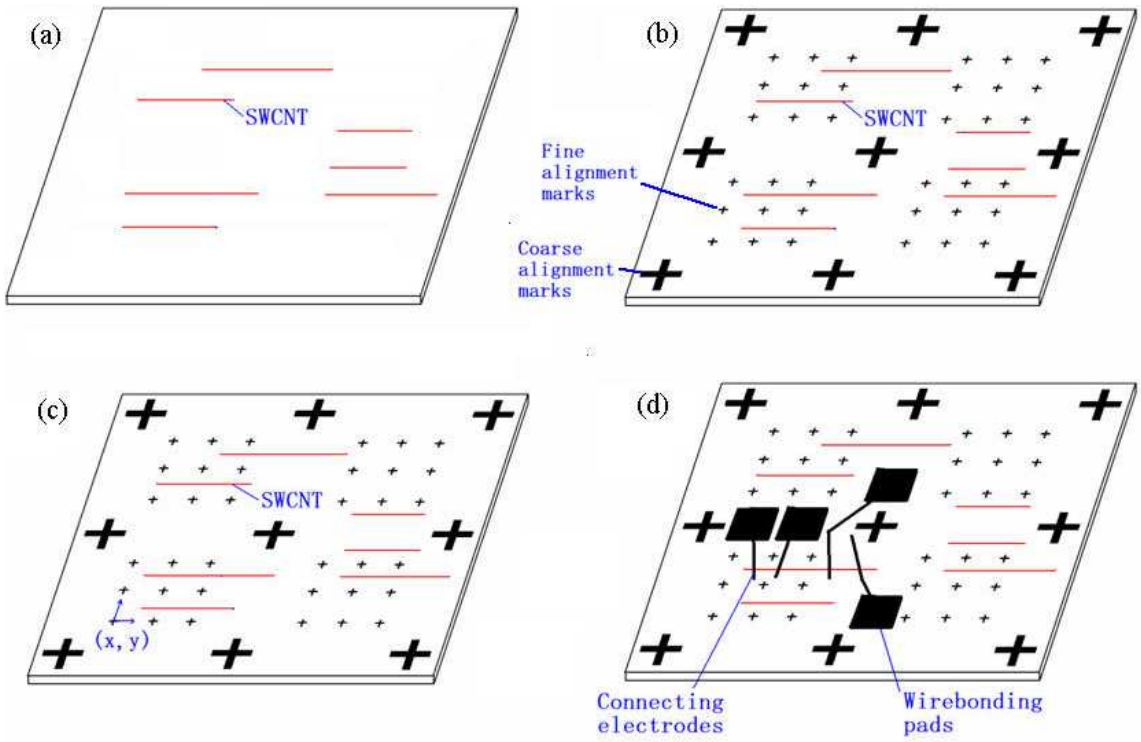

Figure A.1. (Color) Process flow of SWCNT device fabrication. (a) The wafter received with aligned SWCNTs, (b) Coarse and fine alignment marks are patterned, (c) The coordinates of the SWCNTs are obtained by SEM imaging with regard to the alignment marks, (d) E-beam lithography patterning of the connecting electrodes and wire bonding pads.

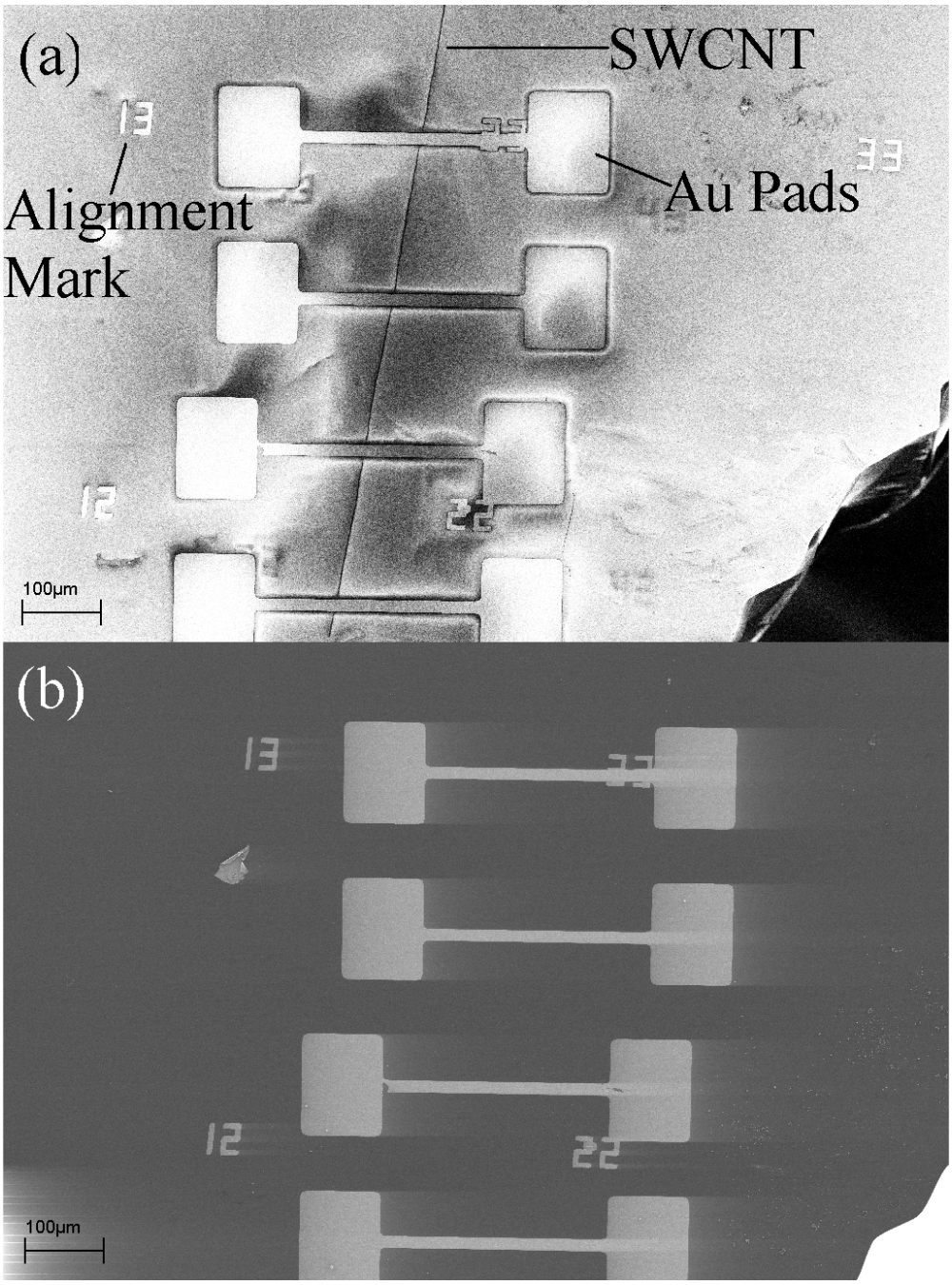

Figure A.2. SEM images of a SWCNT device. (a) Image taken with 3 kV acceleration voltage with in-lens detector. (b) Image taken with 3 kV acceleration voltage with secondary electron detector. The SWCNT is clearly visible only in (a) due to charging effect.

circuits shown in Fig. 3.11. This is because these circuits are current biased by a current source and for high resistance samples, the current source can easily be overloaded as the current I times the sample resistance R_S exceeds 12 V, which is the maximum voltage output of the current source. A voltage bias circuit as shown in Fig. A.3 is used. Although this method is less sensitive than the measurement technique discussed in Chapter 3 and cannot be implemented for four terminal measurement, it is preferable for SWCNT devices as it can measure high resistance samples. In Fig. A.3, the voltage divider is 1022:22≈46.5:1, but any number can be used depending on the voltage range needed. The SWCNT device shown in Fig. A.2 was measured using this technique.

As we only have limited number of SWCNT devices, a systematic study like the MWNT devices presented in this thesis is not possible. Here we will only show our measurement of differential conductance G for a single SWCNT sample as a function of V_{dc} at V_g from 10 V to -10 V as in Fig. A.4. We can see that at 4 K, if the gate voltage $V_g < -4$ V, there is no conduction, while when the gate voltage increases, the conductance increases. This is similar to an n-type semiconductor. At positive voltages, structure appears. Although this looks very similar to the data on tunneling DOS measured by STM [**70**,**71**], further analysis found that the voltage scale we observed is too small for SWCNT DOS[2]. If the structure was the DOS of SWCNT, the voltage scale should be on the order of volts. However, as can be seen in our data, the voltage scale is only about 25 mV. We still do not understand this behavior and further study is certainly needed.

[2]The SWCNTs we obtained are most likely having a diameter of 3∼4 nm.

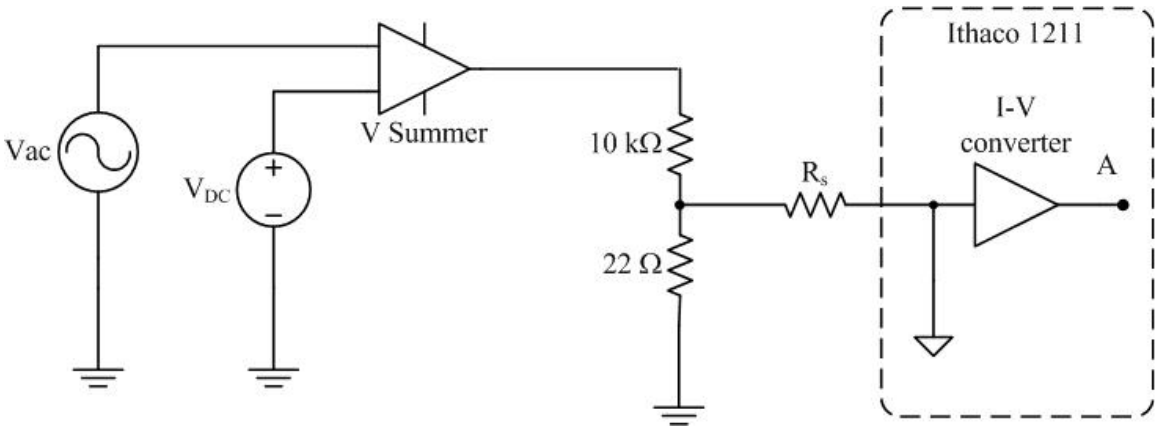

Figure A.3. Circuit diagram of differential conductance measurement by Ithaco 1211. The sample resistance R_S is on the order of MΩ. Port **A** is connected to the lock in amplifier input.

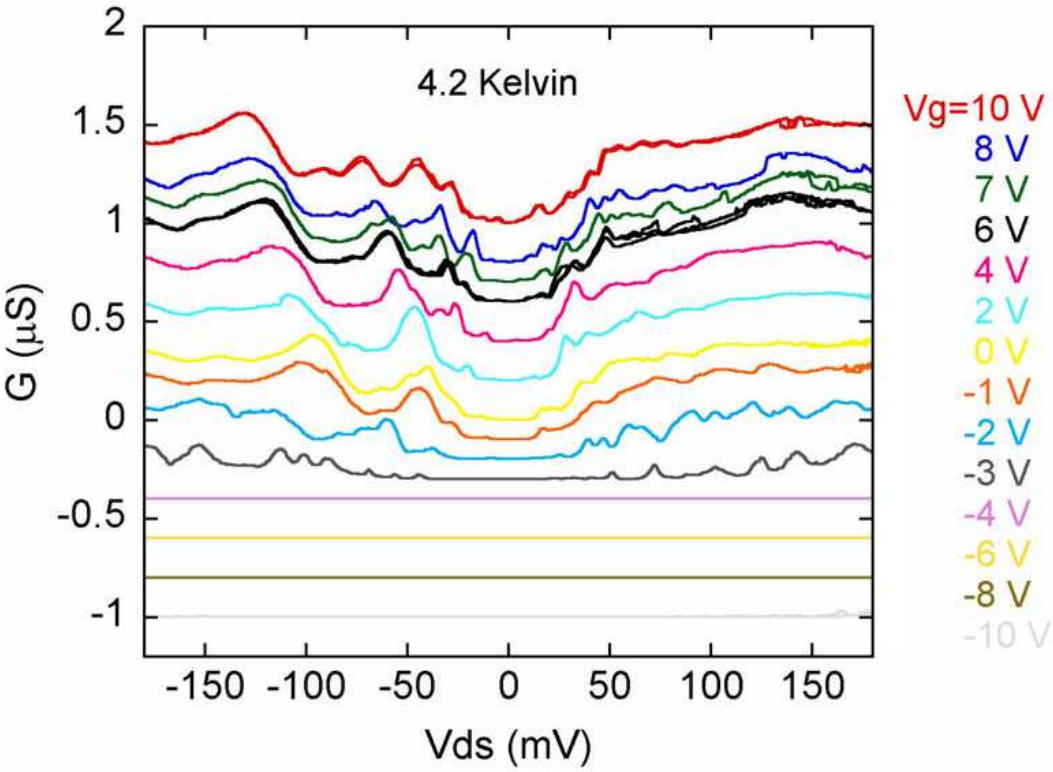

Figure A.4. (Color) Differential conductance vs bias voltage of a SWCNT device at gate voltages from 10 V to -10 V. Data are shifted for clarity.